**University of Natural Resources and Life Sciences, Vienna**
Department of Civil Engineering and Natural Hazards
Institute of Geotechnical Engineering

# Experimental study on the triggering of landslides in partially saturated slopes

MASTER THESIS

For the award of the degree 'Diplom-Ingenieur'
No. 364

Submitted by

DI Grims Michael

born on 16th of February, 1986 in Ried.i.I., Austria

Supervisors:
Univ.Prof. Dr.-Ing. **Wu** Wei
Dipl.-Ing. **Idinger** Gregor

November 2014

# Abstract

The understanding of natural disasters such as landslides, avalanches or earthquakes is of great significance, since they have the potential to cause heavy damage to life and infrastructure. The growing world population implies the need for optimized prediction and protection systems. The experimental investigation in this thesis contributes to better understanding of the triggering conditions of landslides in a partially saturated, non-cohesive soil.

Centrifuge model tests were performed as they provide the possibility to simulate the real stress state of slopes with models of reduced size. This modeling technique allows a large number of experiments within reasonable amount of time under laboratory conditions. The soil in the model slope was compacted in layers. The model slopes were prepared with pre-defined density and water content. 14 slopes were tested under increasing self-weight loading conditions. Poorly graded, medium-fine sand was compacted to four different initial dry densities. Additionally, the influence of the initial water content and slope angle on the stability of a slope was investigated.

During the tests, photos of the soil were taken every five seconds. The processing of the pictures with a Particle Image Velocimetry (PIV)-code and self-written Matlab scripts allowed a comprehensive interpretation and visualization of the soil deformation. The main focus was laid on the explanation of the failure mechanisms and on the impact of varied soil parameters on the slope stability.

It was found, that the density and the water content have great influence. A higher dry density and lower water content increase the stability of the slope. The failure mechanisms reveal a translational nature.

# Kurzfassung

Naturkatastrophen wie Rutschungen, Lawinen oder Erdbeben haben das Potential, großen Schaden an Menschen und Infrastruktur anzurichten. Die wachsende Weltbevölkerung führt zu einem erhöhten Bedarf an optimierten Vorwarn- und Schutzsystemen. Deshalb ist es von Bedeutung, die grundlegenden Prozesse beschreiben zu können. Die experimentelle Untersuchung im Rahmen dieser Arbeit dient einem besseren Verständnis der Auslösebedingungen von Rutschungen in teilgesättigtem, nicht-kohäsivem Boden.

Zentrifugen-Modellversuche wurden durchgeführt, da diese die Möglichkeit bieten, echte Spannungszustände anhand kleiner Modelle zu simulieren. Diese klein-maßstäblichen Modelle wurden erst schichtweise verdichtet, und dann die Böschungen geschnitten. Die Homogenität der Modelle in Bezug auf Dichte und Wassergehalt wurde kontrolliert. 14 Böschungen wurden unter ansteigendem Eigengewicht getestet, bis es zum Versagen kam. Als Modelboden diente ein enggestufter mittel-fein-Sand. Der Einfluss von Trockendichte, Anfangswassergehalt und Böschungsneigung auf die Hangstabilität wurde untersucht.

Während der Tests wurde alle fünf Sekunden ein Foto gemacht. Das Verarbeiten dieser Bilder mit einem "Particle Image Velocimetry" (PIV) Code und selbst erstellten Matlab-Skripten ermöglichte eine umfangreiche Visualisierung und Interpretation der Bodenverformungen. Der Schwerpunkt der Untersuchung lag auf der Erklärung der Bedingungen der Versagensinitialisierung und den dahinter stehenden Mechanismen und Bruchbildern.

Es wurde festgestellt, dass Dichte und Wassergehalt einen großen Einfluss auf die Hangstabilität haben. Eine höhere Trockendichte und ein niedrigerer Wassergehalt haben positiven Einfluss auf die Stabilität. Der Versagensmechanismus kann als Translationsrutschung beschrieben werden, dessen Gleitfuge vom Böschungsfuß ausgehend fortschreitet.

# Acknowledgement

I would like to express my gratitude to my supervisors Prof. Wu and DI Gregor Idinger from the Institute of Geotechnical Engineering at the University of Natural Resources and Life Sciences, Vienna.

Prof. Wu gave me the possibility to work with the only geotechnical centrifuge available in Austria at the moment. The permanent cooperation with DI Gregor Idinger was an essential part of my thesis, as it is embedded in his dissertation. Working together was a rewarding process. I am grateful to his patience and help.

From the geotechnical laboratory, I would like to thank Martin Grogger and Dr. Markus Rauchecker for helping us with the technical problems.

Special thanks deserve my parents as they supported me financially and as parents. It would not have been possible for me to finish my second master thesis without their permanent help.

Finally I thank my girlfriend Laura as she is a person who influenced my life in a very positive way and helped me with her support to finish my study.

# Table of Contents

# 1 Introduction

The negative impacts of natural disasters have always and will always be of high importance for society. Natural hazards exist in different forms such as earthquakes, avalanches and landslides. However, the term ‘natural disasters’ should be used with precaution, as the process itself is natural, but the negative, catastrophic effects can just emerge due to human vulnerability (WISNER et al. 2004). This vulnerability increases with the rising world population as more damage is expected at heavily populated areas. On the other hand the capability of humanity to deal with such events increases with the scientific and technical achievements. Some active and passive measures have been applied and improved. For instance some protection structures such as embankments against floods or earthquake resisting buildings have become increasingly sophisticated. Hazard mapping and land management can avoid or decrease the negative impact of natural disasters. Disaster response exercises conducted with the population can be another mitigation measure. But independently from the type of countermeasure, the positive effect rises significantly with the capability to predict natural disasters. For example, the planning of residence areas should be based on the knowledge of magnitude and probability of possible events. Research which aims to explain the causes of dangerous natural processes can contribute to improved prediction.

## 1.1 Examples of landslides

Hong Kong is especially susceptible to landslides due to steep hills, poor compaction and the high probability of heavy rainfall (TAKE et al. 2004). In 1972 for instance, a landslide killed several people (Fig. 1; GOVERNMENT INFORMATION CENTRE HONG KONG). TAKE et al. (2004) conducted research to examine possible triggering mechanisms which lead to such landslides. An Austrian example of a recent landslide with significant consequences is the event at the Felbertauern (Fig. 2; TOURENFAHRER). It destroyed a traffic route of high importance for the region.

## 1.2 Aims of the research

This master thesis is embedded in a research project on the stability of partially saturated soil slopes (IDINGER 2015). The complete research was conducted in cooperation and the objectives were coordinated.

Landslides normally occur in areas of partially saturated soils as this soil state is the most common in nature. A significant number of research has already been conducted on the subject of partially saturated soils by considering the capillary forces (e.g., DELAGE 2002) but still many processes are not fully explained and understood.

- This research aims at better understanding of landslides occurring in partially saturated, non-cohesive soil.
- The centrifuge modeling technique was applied to model slopes at a small-scale. Therefore the model box and its corresponding components had to be designed and optimized.
- The main focus lies on the description and explanation of the pre-failure conditions and the failure mechanisms as well as on the identification of the factors which have notable influence on the slope stability.

**Fig. 1: Landslide in Hong Kong -1972**
**(GOVERNMENT INFORMATION CENTRE HONG KONG)**

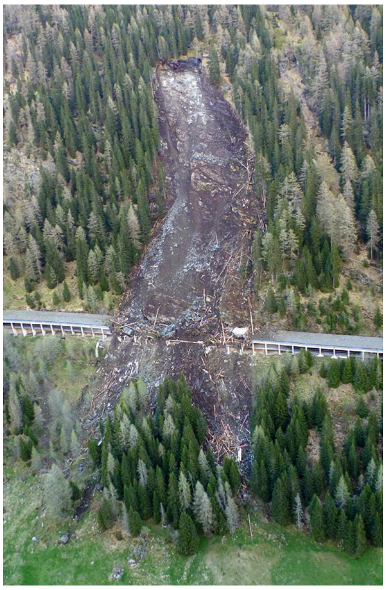

**Fig. 2: Landslide at Felbertauern - 2013**
**(TOURENFAHRER)**

# 2 Background and related work

## 2.1 Unsaturated soil mechanics

An overview of effective stress definitions for partially saturated soils can be found in NUTH & LALOUI (2008). The effective stress principle of TERZAGHI (1936) is one of the earliest theories in saturated soil mechanics. Ever since, several concepts for unsaturated soils were proposed as the understanding is of high importance for many geotechnical problems.
Terzaghi defined the effective stress in fully saturated soils as follows:

$$\sigma' = \sigma - u_w$$

where $u_w$ is the pore water pressure and $\sigma$ is the total stress. This equation is just valid when the fluid and the solid material are incompressible and the soil is fully saturated.

The effective stress $\sigma'$ in dry soils with $u_w = 0$ becomes:

$$\sigma' = \sigma$$

For unsaturated soils, BISHOP (1959) proposed the following equation:

$$\sigma' = (\sigma - u_a) + \chi(u_a - u_w)$$

Where $\chi$ is called the Bishop's parameter and $u_a$ is the pressure in gas and vapor phase. The term $\sigma - u_a$ defines the net stress, and $u_a - u_w$ the matric suction. $\chi$ ranges from 0 for dry soils to 1 for completely saturated soils. SCHREFLER (1984) defined a simple relationship as follows:

$$\chi = S_r$$

Fig. 3 contains measured values for $\chi$ of various soils.

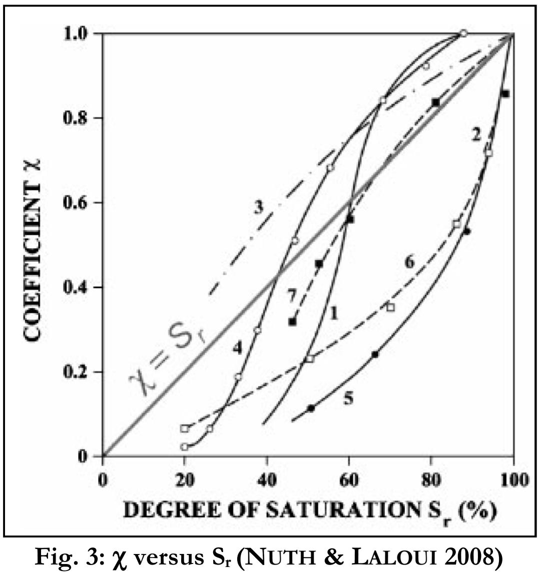


**Fig. 3: $\chi$ versus $S_r$ (NUTH & LALOUI 2008)**

A trend in Fig. 3 is obvious, but the relationship is more complex than defined by SCHREFLER (1984). Many different definitions exist, such as those introduced by AITCHISON (1961) or KHALILI & KHABBAZ (1998).

In this thesis, the soil water content is a factor of high importance, as it notably influences the stability of the slope. VANAPALLI et al. (1996) described a concept which explains the various stages of saturation and its influence on the suction (Fig. 4). Stage 1 is termed the 'boundary effect zone', stage 2a the 'primary transition zone', stage 2b the 'secondary transition zone' and stage 3 the 'residual zone of unsaturation'.

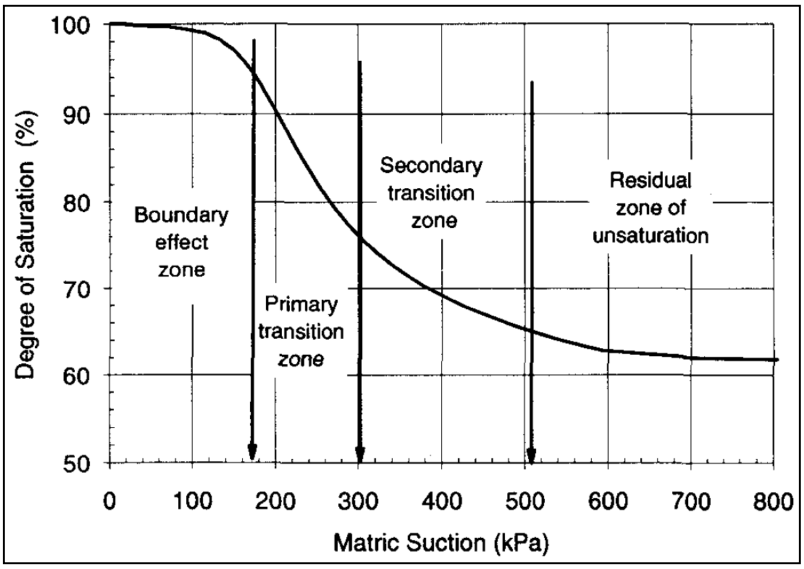


**Fig. 4: Saturation and matric suction (hypothetical porous medium) (VANAPALLI et al. 1996)**

At stage 1, the pores are filled with water and the single stress state can be described with:

$$\sigma' = \sigma - u_w$$

Stage 2 starts at the air-entry value, where air enters the biggest pores. During stage 2 and 3, the saturation decreases significantly and the suction increases. In the last stage, small changes in saturation lead to a high change in suction.

Fig. 5 illustrates the different stages (VANAPALLI et al. 1996). An additional amount of air as well as less water can be observed from stage to stage.

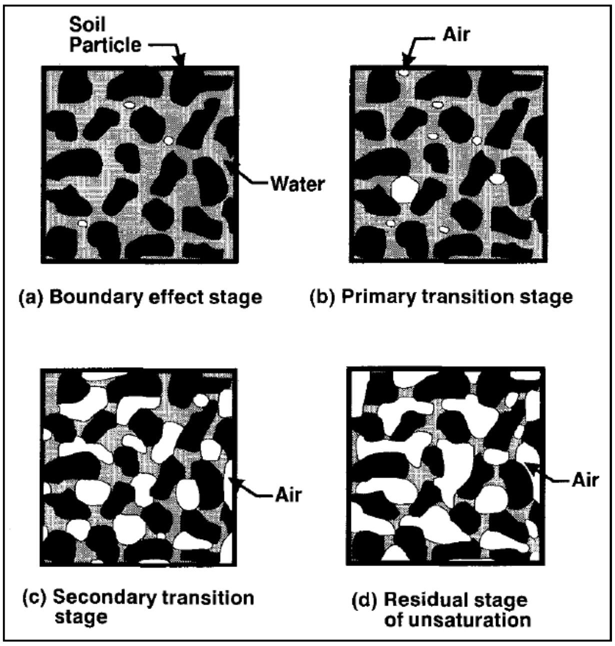


**Fig. 5: Different stages, soil – water – air (VANAPALLI et al. 1996)**

Soil-water characteristic curves (SWCC) such as the hypothetical one of Fig. 4 are derived from laboratory tests and described by mathematic functions. On the y-axis they show the water content or the degree of saturation and on the log-x-axis the suction, which ranges from zero to the zone of high suction. The determination of suction in laboratory can be rather difficult, especially in the zone of higher suction. Several mathematical equations for SWCCs were proposed by different authors. VAN GENUCHTEN (1980), MUALEM (1976) and BURDINE (1953) suggested functions which are asymptotic to a horizontal line in the range of high suction. Hence the curve never goes through 0 water content in this zone. FREDLUND & XING (1994) introduced a correction factor which forces the curve through 1,000,000 kPa at a water content of 0. Furthermore there exist functions which derive the whole SWCC from parameters such as the GSD-curve and the water content at fully saturated conditions.

Real SWCCs are actually much more complex (NG & MENZIES 2007) than the curve presented in Fig. 4. Depending on whether the soil is in a drying or in a wetting process, the curves can differ significantly. Hence more SWCCs exist for the same soil, resulting in a main drying and wetting curve. This behavior is called 'hysteresis'. Fig. 6 shows measured points and mathematically fitted curves for the same sand. Notable differences can be observed between the initial drying curve and the main wetting and subsequent drying curve. This effect can be explained by the 'ink bottle' effect, for instance NG & MENZIES (2007) (Fig. 7). On the left side, the drying effect is illustrated. The larger part of the pore is filled with water. On the right side, this part of the pore is empty, as the soil water is not strong enough to overcome the capillary forces at the boundary of the large pore.

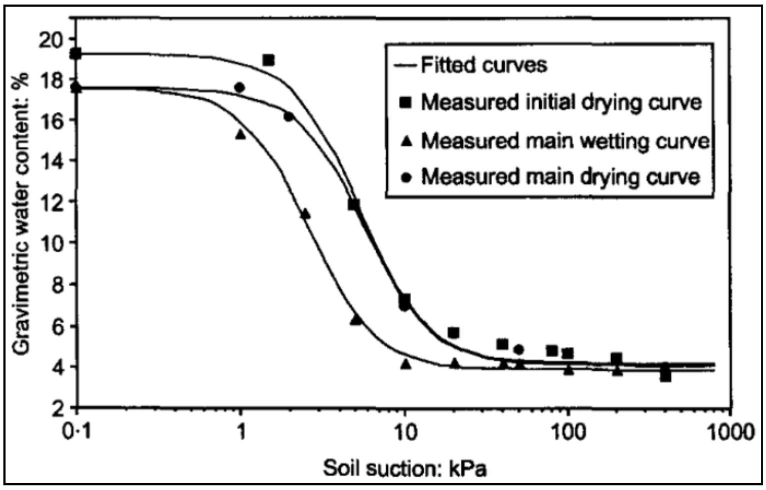


**Fig. 6: Different SWCCs for the same sand (PHAM et al. 2003)**

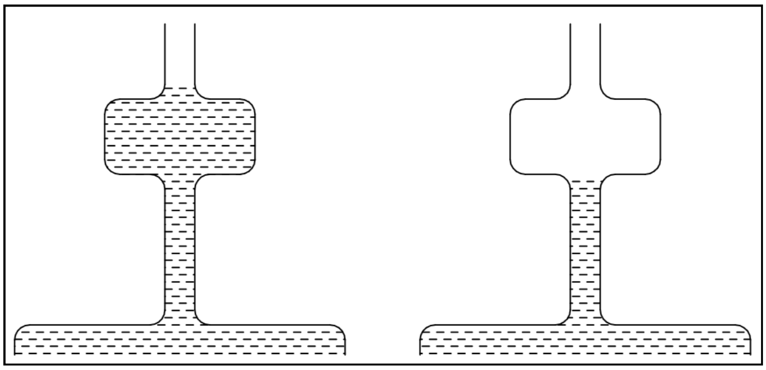

**Fig. 7: Ink bottle effect**

## 2.2 Slope stability and landslides

Landslides occurs due to the loss of stability of the soil material and is a gravitation driven process. Failure happens, when the driving forces are larger than the retaining ones. A broad range of events is subsumed with the term 'landslide'. A review of classifications of landslides was given by HUNGR et al. (2001). Their classification is based on the factors velocity, material involved or water content, among others.

### 2.2.1 Shear strength

For describing the shear strength of unsaturated soil, the following equation with two independent stress state variables can be used (FREDLUND et al. 1978):

$$\tau = c' + (\sigma - u_a)tan\phi' + (u_a - u_w)tan\phi^b$$

This formulation of the failure envelope can be illustrated as a three-dimensional graphic (Fig. 8), where the x-axis shows the net normal stress, the y-axis the shear stress and the z-axis the matric suction (FREDLUND & RAHARDJO 1993).

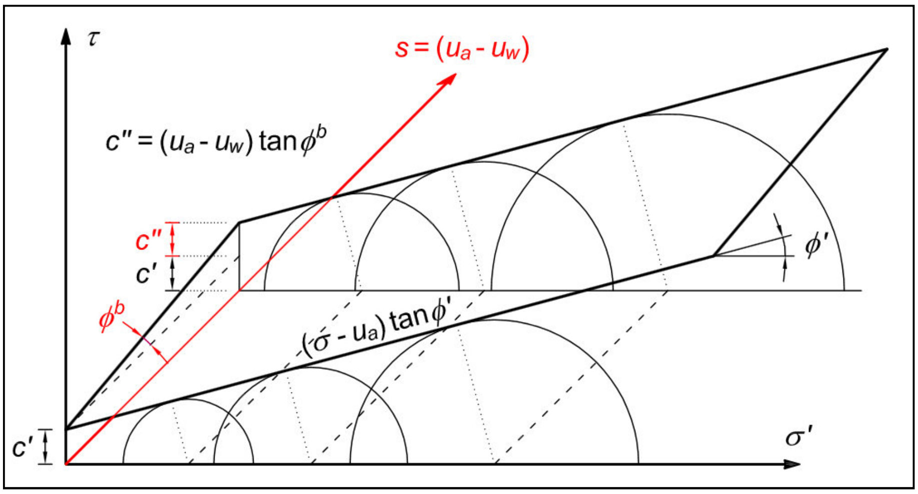


**Fig. 8: Extended Mohr-Coulomb failure envelope for unsaturated soils (After FREDLUND & RAHARDJO 1993)**

Where in the above equation, c' is the intercept of the (extended) Mohr-Coulomb failure envelope on the axis of the shear strain when the net normal stress and the matric suction are zero (RAHARDJO et al. 2002). The term ($\sigma$ - $u_a$) stands for the net normal stress and the term ($u_a$ - $u_w$) for the matric suction. $\phi$' is the effective internal friction angle as known from Mohr's two-dimensional failure envelope. This definition is extended with $\phi^b$, describing the increase in shear strength, as a factor of the matric suction (NG & MENZIES 2007).

BISHOP (1959) proposed another equation, where the $\chi$-parameter is used.

$$\tau_f = c' + \left[(\sigma - u_a)_f + \chi(u_a - u_w)_f\right] tan\phi'$$

As already described earlier, $\chi$ is related to the degree of saturation of the soil. Contrary to the extended Mohr-Coulomb failure envelope, this formulation contains a single $\phi$-angle.

### 2.2.2 Calculated slope stability

The stability of a slope is influenced by various factors:

- Geometry of slope surface
- Ground conditions
- Mechanical properties such as shear parameters, density or permeability
- Groundwater in the slope
- External loads
- In situ stress
- etc.

Different models for calculating and describing slope stability exist. The following part of the chapter gives a short overview according to PREGL (1999).

The model applicable for examining slope stability strongly depends on the shape of the moving part of the slope. If it is parallel to the surface of the slope, the stability can be calculated relatively easily. This is the case, when the soil is homogenous or all different layers are parallel to the surface.

In practice, limit equilibrium models are popular, such as the method of Bishop and Janbu. Thereby the slope is divided in vertical stripes. The number of stripes should be at least 10. Subsequently, the applied forces vs. the resisting ones are calculated and compared. Various potential failure planes are investigated, and the weakest one finally determines the significant factor of safety.

Several other methods exist for slope stability. Nowadays the calculations are normally computer-assisted, using finite elements for instance.

## 2.3 Geotechnical modeling of slopes

Many methods exist for modeling geotechnical problems. Computer simulations are a possibility as already described earlier (e.g., PIETRUSZCZAK & HAGHIGHAT 2013). They get increasingly important nowadays, but they always depend on the validation of laboratory and in-situ tests. Field tests are another possibility (RAHARDJO et al. 2002). They can provide good results due to the genuine conditions but often are difficult to perform. WANG & SASSA (2003) reported laboratory tests on small-scale models at 1 g conditions. Such experiments are easier to perform than centrifuge modeling, but the stress state differs from that of the real case. Centrifuge tests provide a reasonable compromise between quality and work.

First geotechnical experiments with a centrifuge were reported by BUCKY (1931). Decades later, SCHOFIELD (1980) achieved a broad approval in the geotechnical community. Ever since, a remarkable amount of scientific work has been accomplished in this field (e.g. TAKE et al. 2004, LING et al. 2009, TAMATE et al. 2012).

### 2.3.1 Types of centrifuges

There are two different types of geotechnical centrifuges. The beam-type centrifuge (Fig. 9) and the drum centrifuge. Beam-type centrifuges consist of a beam which rotates around a vertical axis. On the ends of the beam, the model is mounted on one side and the counterweight on the other. The model is located on a swinging platform, which allows an upswing of nearly 90° during flight. On the opposite side of the beam, the counterweight keeps the system in balance. It is of high importance, that the counterweight is distributed over the swinging platform in a similar way as the weight of the model. The maximal payload vs. the maximal acceleration is always a compromise. With a higher model-weight, a lower max. acceleration is possible. The second type of centrifuges is the drum-type centrifuge. It provides the possibility to model a soil without endings and it basically consists of a cylinder which rotates around a vertical axis. The soil is located at the inner side of the walls of the cylinder. Differences in model height and rpm exist between those two types of centrifuges (MUIR WOOD 2004). The model height in beam-type centrifuges is normally higher but the rpm are lower. More details to the centrifuge used in this investigation will be given in Chapter 3.4.

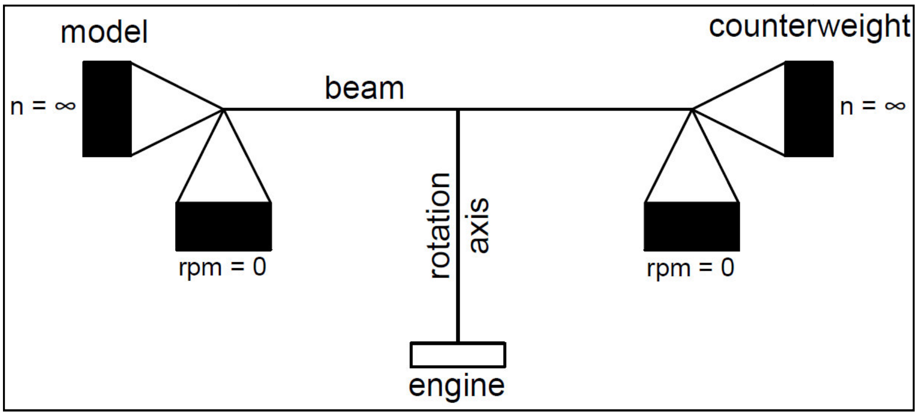


**Fig. 9: Schematic layout of beam-centrifuge**

### 2.3.2 Acceleration in the centrifuge: The n-factor

The scaling-factor n is explained in Fig. 10. The left illustration represents the prototype with a height of 1 and a max. stress of 1 (example without units). The illustration in the middle shows the soil model on a reduced size where h = 0.2 and the stress is 0.2, having a scaling factor of 5. The stress distribution on the right shows the small scale model under centrifuge acceleration of 5 g. There, the height is still 0.2, but the max. stress is 1, like in the prototype. This kind of modeling has the advantage of being able to simulate gravitational processes of a large slope with a small model. The model slope of the experiments of the actual research has a height of 20 cm, resulting in a slope of 20 m when 100 g (n = 100) are applied.

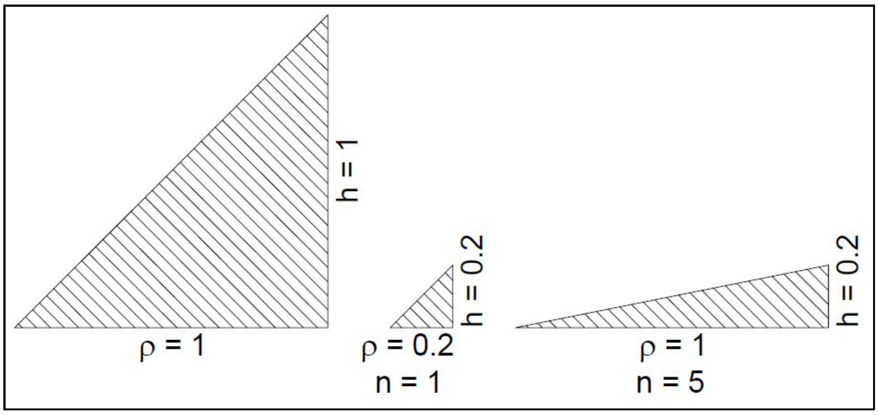


**Fig. 10: n-factor**

### 2.3.3 Theoretical upswing angle

Due to the centrifugal forces, the swinging basket of beam-type centrifuges approaches the horizontal position with an increasing scaling factor n. Fig. 11 illustrates the theoretical upswing angle of the swinging platform, assuming no friction and an equally distributed weight of the model box. Already at 6 g, an angle of more than 80 degrees is reached. 29 g result in an angle of more than 88 degrees and at 58 g the angle exceeds 89 degrees. In real tests, additional factors such as the friction of the pivot exist. More on this issue will be discussed in the Chapter 3.4.

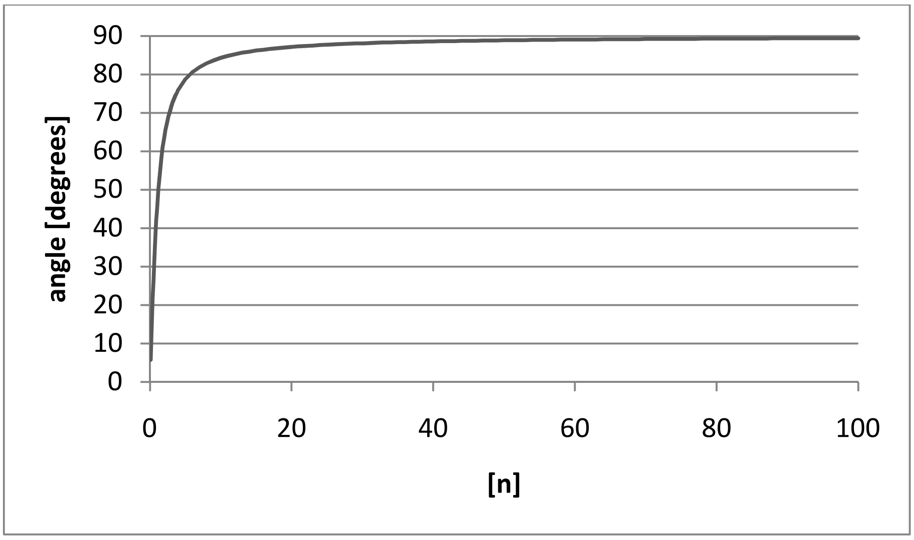


**Fig. 11: Theoretical upswing angle**

### 2.3.4 Modeling inaccuracies

For civil engineering purposes, the earth can be idealized as a flat surface since the radius of it is relatively high in comparison to the area of a typically investigated geotechnical problem. But the acceleration field which occurs in a centrifuge is radial (MUIR WOOD 2004). This leads to certain inaccuracies in the stress field, which can be accepted when the ratio of the width of the model to the radius of the centrifuge is sufficiently small.

Another inaccuracy occurs due to the fact, that the stress is a function of the radius. Hence it changes with the height of the model as explained in detail in Chapter 3.4.

Boundary conditions also have to be taken into account. At the conducted research they were optimized by using silicone oil at the walls of the model box.

During dynamic processes such as simulated rainfall, the moving parts additionally experience Coriolis acceleration (MUIR WOOD 2004).

### 2.3.5 Scaling laws

In centrifuge tests, scaling laws have to be applied as most parameters change with the n-factor. Table 1 gives an overview (KONKOL 2014, GARNIER et. al 2007). As an example, a length of 1 in the prototype results in 1/n in the model.

**Table 1: Scaling laws for tests with centrifuges**

| Parameter | Unit | Scaling Law (model/prototype) |
|---|---|---|
| **BASIC SIMILARITIES** | | |
| length | m | 1/n |
| area | $m^2$ | $1/n^2$ |
| volume | $m^3$ | $1/n^3$ |
| density | $kg/m^3$ | 1 |
| mass | kg | $1/n^3$ |
| gravitational acceleration | $m/s^2$ | n |
| unit weight | $N/m^3$ | n |
| stress | $N/m^2$ | 1 |
| strain | - | 1 |
| force (static) | N | $1/n^2$ |
| displacement | m | 1/n |
| **FLUID FLOW IN SATURATED CENTRIFUGE SAMPLES** | | |
| Darcy permeability k | m/s | n |
| Darcy flow rate v | m/s | n |
| Hydraulic gradient i | - | 1 |
| time | s | $1/n^2$ |
| **UNSATURATED CONDITIONS** | | |
| capillary rise | m | 1/n |
| time | s | $1/n^2$ |

# 3 Material and Methods

## 3.1 Soil description

The material used for the experiments was taken from the landfill Fischamend Ing. Rottner GesmbH, located near the Vienna airport/Schwechat. Altogether, some 73 kg have been sampled in soil buckets. As for one experiment less than half of the total amount was necessary, the soil for one experiment could be prepared while running another one at the same time. Several classification tests were conducted in order to define the soil properties.

### 3.1.1 Grain size distribution curve (GSD-curve)

The GSD-curve (Fig. 12) was determined by DIWALD (2011) and illustrated by IDINGER (2015).

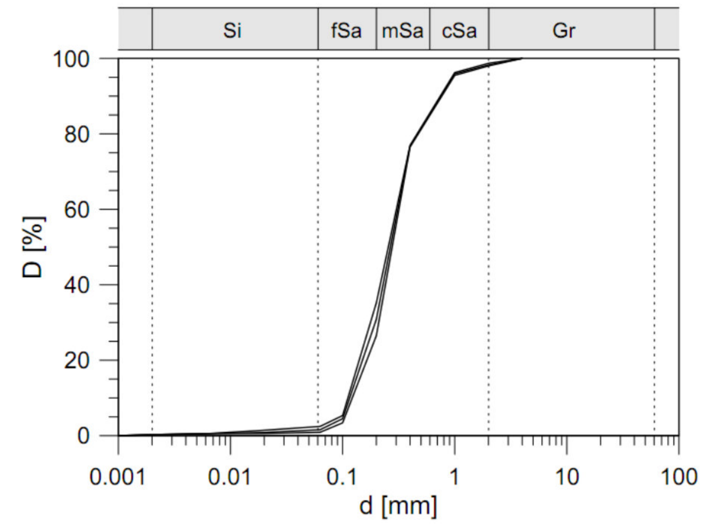


| | | |
|---|---|---|
| Cl | 0.2 ± 0.1 | % |
| Si | 1.4 ± .07 | % |
| Sa | 97.0 ± 0.6 | % |
| Gr | 1.4 ± 0.2 | % |
| fSa | 29.0 | % |
| mSa | 54.6 | % |
| cSa | 13.4 | % |
| $d_{max}$ | 4.0 | mm |
| $d_{50}$ | 0.27 ± 0.011 | mm |
| $d_{10}$ | 0.12 ± 0.006 | mm |
| $C_c$ | 1.0 ± 0.1 | - |
| $C_u$ | 2.7 ± 0.1 | - |

**Fig. 12: Grain size distribution of used soil**

The soil can be classified as poorly graded, medium-fine quartz sand.

### 3.1.2 Analysis of SEM images

The images taken with a scanning electron microscope (SEM) (NOTTINGHAM CENTRE FOR GEOMECHANICS 2014) were visually analyzed (Fig. 13). The main component of sand as well as the small percentage of fine particles are in accordance with the GSD.

In the lowest zoom level, mainly the sand particles are visible. In the medium zoom level, the particles smaller than sand can be seen and in the highest zoom-level the microstructure of those can be observed.

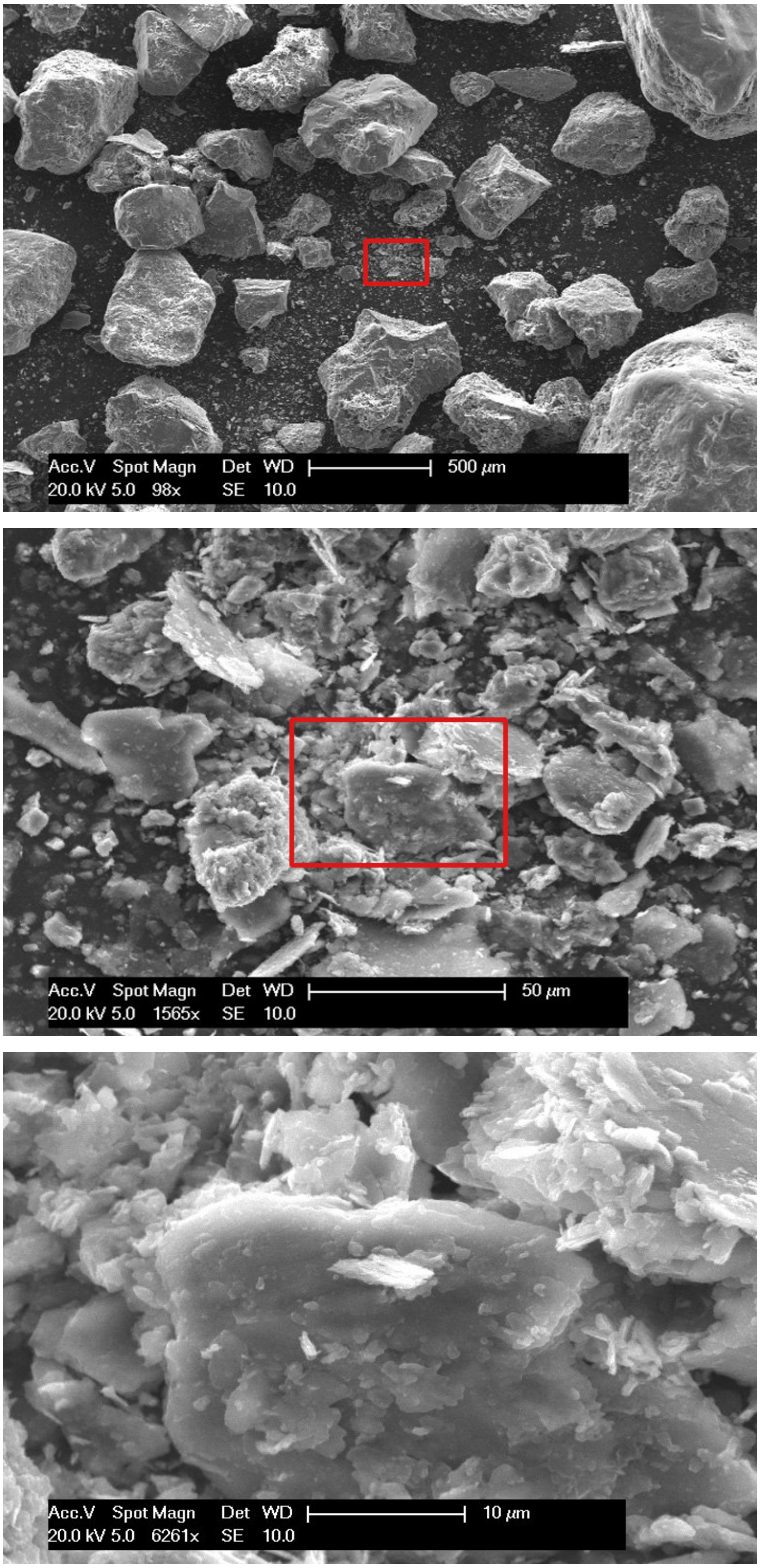


**Fig. 13: SEM images**

### 3.1.3 Densities

Fig. 14 and Table 2 give an overview of relevant densities of the soil. The hatched area of Fig. 14 represents the range of densities examined in the centrifuge experiments. Four different densities were chosen (E1 to E4). 'Min' and 'Max' stands for the minimum and the maximum density. 'Pr' is the Proctor density.

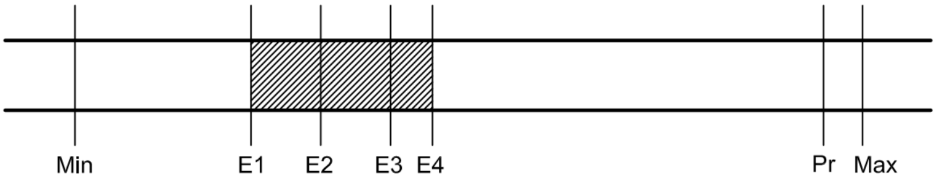


**Fig. 14: Overview of various densities**

**Table 2: Various densities and their corresponding parameters**

| | Min | E1 | E2 | E3 | E4 | Pr | Max |
|---|---|---|---|---|---|---|---|
| $\rho_d$ | 1.27 | 1.40 | 1.45 | 1.50 | 1.53 | 1.81 | 1.84 |
| $e$ | 1.09 | 0.91 | 0.84 | 0.78 | 0.74 | 0.48 | 0.45 |
| $n$ | 0.52 | 0.48 | 0.46 | 0.44 | 0.43 | 0.32 | 0.31 |
| $D_r$ | 0.00 | 0.29 | 0.40 | 0.49 | 0.55 | 0.96 | 1.00 |
| $D_{Pr}$ | 0.71 | 0.78 | 0.80 | 0.83 | 0.85 | 1.00 | 1.02 |
| *Class.* (Table 3) | | loose | medium dense | medium dense | medium dense | very dense | |

Where:

$$\rho_d = dry\ density$$

$$e\ (void\ ratio) = \frac{\rho_s}{\rho_d} - 1$$

$$n\ (porosity) = 1 - \frac{\rho_d}{\rho_s}$$

$$D_r(relative\ density) = \frac{e_{max} - e}{e_{max} - e_{min}}$$

$$D_{Pr}(relative\ Proctor\ density) = \frac{\rho_d}{\rho_{Pr}}$$

**Table 3: Class. (DIN EN ISO 14 688-1)**

| $D_r$ [%] | Class. |
|---|---|
| 0 – 15 | very loose |
| 15 – 35 | loose |
| 35 – 65 | medium dense |
| 65 – 85 | dense |
| 85 – 100 | very dense |

The experiments in the centrifuge were conducted with loose and medium dense soils, following the classification of Table 3. For the densest soil, the relative Proctor density at 85 % ($D_{Pr85}$) was selected.

## Particle density

The particle density of 2.669 ± 0.004 g/cm³ was found with a series of seven pycnometer tests (ÖNORM B4413) by DIWALD (2011).

## Proctor density

In order to determine the compressibility of the soil at various water contents, a proctor test was run by DIWALD (2011) (Fig. 15).

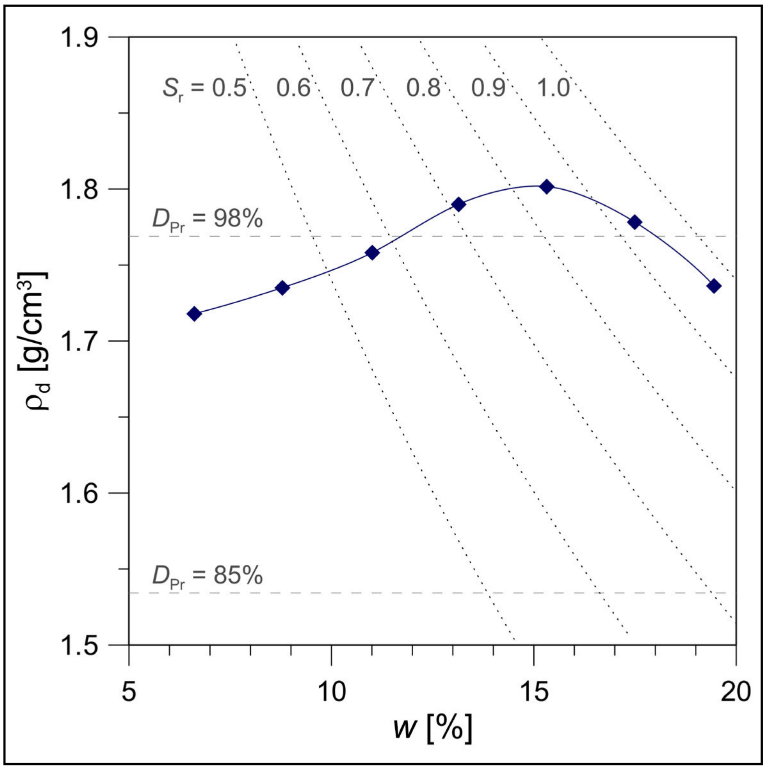


**Fig. 15: Proctor compaction curve (IDINGER 2015)**

The peak of the curve was found at a water content of 15.1 % with a dry density of 1.81 g/cm³. The $D_{Pr98}$ can be determined with 1.77 g/cm³ and the $D_{Pr85}$ with 1.53 g/cm³. The $D_{Pr98}$ can be reached at water contents between 11.6 % and 18.2 %. Those two water contents served for selecting the water contents for the experimental investigation, were the lower value is on the dry side of optimum and the higher one on the wet side of optimum.

## Minimum density

In order to determine the minimum density, a test was performed with a cylinder of defined volume, following the standards of ASTM D4254 (Fig. 16).

**Fig. 16: Cylinder with soil**

A funnel served for filling the cylinder with soil. The exact dimensions of the cylinder were measured with a vernier caliper at multiple points, resulting in a mean value of 17.49 cm of height and 14.93 cm of diameter, and hence the volume is 3061.96 $cm^3$.

Soil preparation was done by drying the soil and then sieving it to eliminated conglomerates. Then soil material was poured carefully into the cylinder, using the funnel. Thereby, the funnel was held in a proper position to achieve a permanent drop height of about 13 mm. For filling the cylinder evenly with material, a spiral movement was conducted with the funnel. A plane surface was created finally for achieving exactly the calculated volume.

The mass of the soil was found by measuring together the cylinder and the soil, and afterwards subtracting the mass of the empty cylinder. For checking the result of the process, the bucket which contained the soil was measured previously and after filling the cylinder. By calculating the difference, the mass of the used soil could be determined a second time and was compared to the first result. The two methods always led to corresponding results.

The complete process was conducted three times. Table 4 shows the results of the tests. By definition of ASTM D4254 the values of the density are allowed to differ maximally 1 %. A difference of 0.08 % could be achieved, thus the results were found to be accurate enough and the mean of the three values could be calculated.

Table 4: Results of the tests for determining the minimum density

| Nr. | Mass of cylinder + soil [g] | Mass of cylinder [g] | Mass of soil [g] | Density [g/cm³] |
|---|---|---|---|---|
| 1 | 18 392 | 14 492 | 3900 | 1.274 |
| 2 | 18 394 | 14 492 | 3902 | 1.274 |
| 3 | 18 396 | 14 492 | 3904 | 1.275 |
| | | | **Mean density** | **1.274** |

## Maximum density

To determine the maximum density of the soil, a series of tests with a cylinder and surcharge weights was conducted (Fig. 17).

**Fig. 17: Cylinder with weights**

For filling the cylinder with soil, a funnel was used. With a vibrating plate, the demanded compression could be achieved.

The cylinder was filled with soil to a height of about 12 cm in a similar way as it was filled for the tests of the minimum density. Subsequently, weights of 23.243 kg in total were placed above it. After mounting the cylinder with the soil and the weights on the vibrating plate, the latter was turned on for 8 min.

The height of the compressed soil was determined by measuring and subtracting the distance of the top of the cylinder to the top of the soil from the total height of the cylinder. All measurements were conducted with a vernier caliper and repeated three times. The diameter of

the cylinder was measured with 14.93 cm and respectively the volume of the compressed soil could be calculated.
By subtracting the mass of the empty cylinder plus the weights from the total mass, the mass of the compressed soil was determined. For checking, the weight of the bucket with the soil was measured before and after filling the cylinder. The differences of the two values corresponded with the results of the first method used for obtaining the mass of the soil.
The experiment was conducted three times. Table 5 shows the results of the tests. By definition of ASTM D4253 the values of the density are allowed to differ maximally 2 %. A difference of 0.16 % was achieved, thus the results were found to be accurate enough and the mean of the three values could be calculated.

**Table 5: Results of the tests for determining the maximum density**

| Nr. | Volume [cm³] | Mass [g] | Density [g/cm³] |
|---|---|---|---|
| 1 | 1435.57 | 2639 | 1.838 |
| 2 | 1506.47 | 2764 | 1.835 |
| 3 | 1543.93 | 2836 | 1.837 |
| | | **Mean Density** | **1.837** |

### 3.1.4 Shear strength

With triaxial compression tests, the shear strength of the model soil with a dry density of 1.53 g/cm³ was determined as described in SCHÖFER (2012) and IDINGER (2015). This is the densest compaction of the soil which was used for the experiments in the centrifuge.
Tests were performed under saturated (s = 0 kPa) and partially saturated (s = 10 kPa) conditions. Fig. 18 and Table 6 show the results.

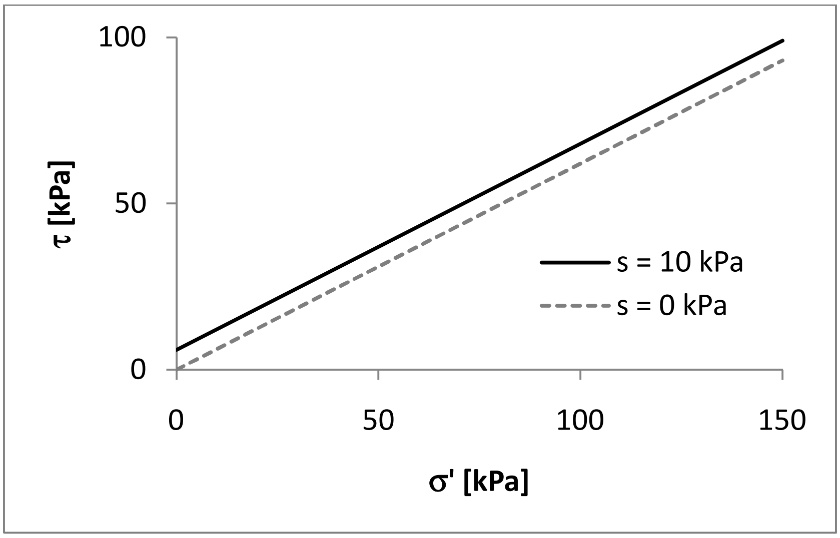


**Fig. 18: Lines of shear resistance according to Mohr-Coulomb**

**Table 6: Results of triaxial compression tests**

| | $\phi'_f$ [deg] | $c_f$ [kPa] |
|---|---|---|
| s = 0 kPa | 31.8 | 0.0 |
| s = 10 kPa | 31.8 | 6.0 |

### 3.1.5 Water content and saturation

Fig. 19 illustrates the water content and the degree of saturation for the four densities which were applied at the experiments in the centrifuge. To make the results comparable, the same soil moisture content had to be used for various densities. Depending whether same saturation or same water content are chosen, the amount of water differs. For the experiments of this research, the water content was used for defining the amount of water which was added to the soil.

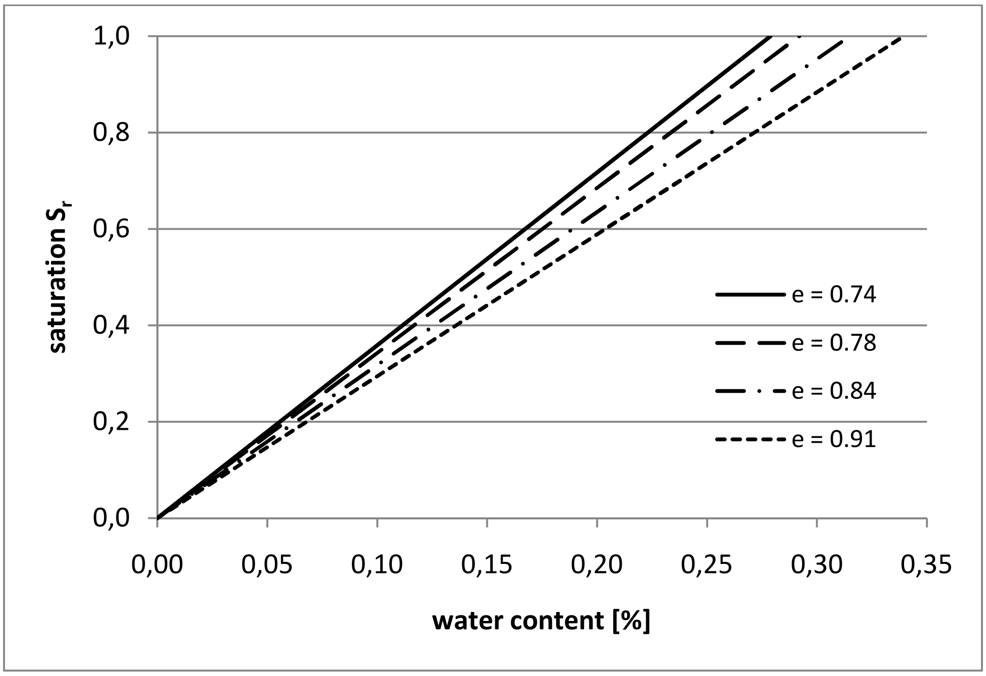


**Fig. 19: Saturation and water content**

### 3.1.6 Interaction of soil, atmosphere and water

The water within the soil matrix and the water of the air in the gaseous phase are in a process of permanent exchange. One $m^3$ of fully saturated air at a temperature of 20° C contains 17.3 g of water. This process was not considered to be a problem for the soil in the model box, as the air volume is much less than one $m^3$ and the few grams of water which can evaporate from the soil are negligible.

On the contrary, the evaporation had to be taken into account during the process of taking samples for determining the water content. As these samples have a high ratio of surface to volume, they had to be weighted as soon as possible after taking them, in order to avoid wrong results due to evaporation. Quantitative and qualitative tests were run to determine the named effect.

Fig. 20 shows soil of dark brown color with a water content of about 10 % and dry soil of light brown color. The soil was placed in an air-tight bucket were no exchange with the surrounding air was possible. In the left bottom corners of the pictures, direct contact of dry and wet soil was established. The dry soil in the glass bowl had no direct contact to the wet soil, but only over the air phase. The right picture was taken 25 hours after the left one.

**Fig. 20: Interaction of soil, atmosphere and water**

The qualitative, visual analysis of the two pictures led to the result, that due to capillarity a strong interaction of soil with direct contact exists. The soil where the interaction was just possible over the air shows nearly the same color and led to the conclusion, that the exchange is comparatively weak.

Two quantitative tests were conducted for determining the interaction between the water of the soil and the water of the air in the gaseous phase (Fig. 21). A soil sample with $\rho_d$ = 30.32 g and a water content of 9.4 % was allowed to dry at room temperature. This turned out to be a relatively slow process. After 30 hours a stable water content of 0.56 % was reached.
Afterwards the soil was completely dried in the drying oven and then left at the air at room temperature. A stable water content of 0.46 % was already reached after 4.5 hours, resulting in a difference of 0.1 % water content between drying and wetting process.

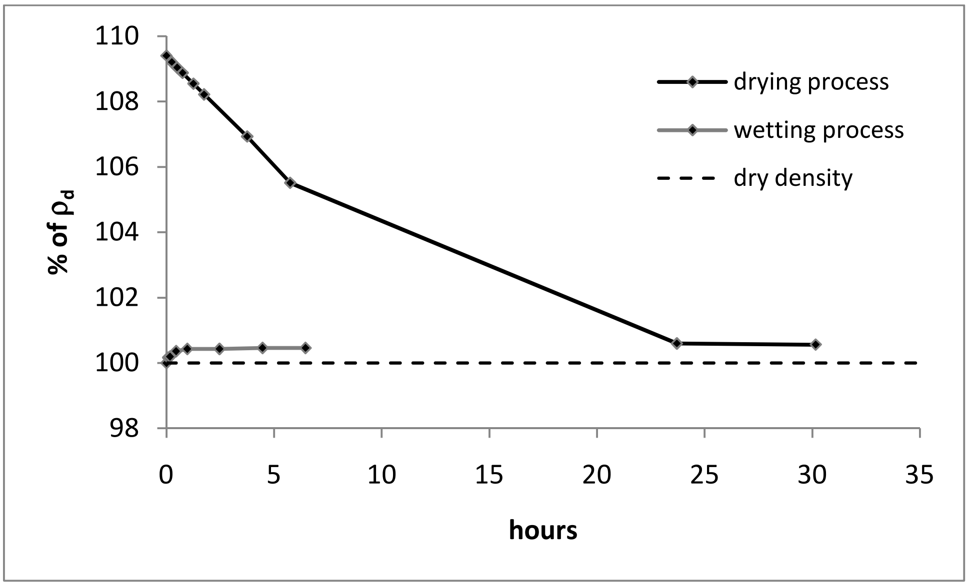


**Fig. 21: Drying and wetting process of the soil at room temperature**

### 3.1.7 Soil water characteristic curve (SWCC)

Fig. 22 shows the SWCC for e = 0.74. It is based on the work of SCHÖFER (2012) using a modified Kovács model (AUBERTIN et al. 2003). Two laboratory-measured points were added to adjust the SWCC IDINGER (2015).

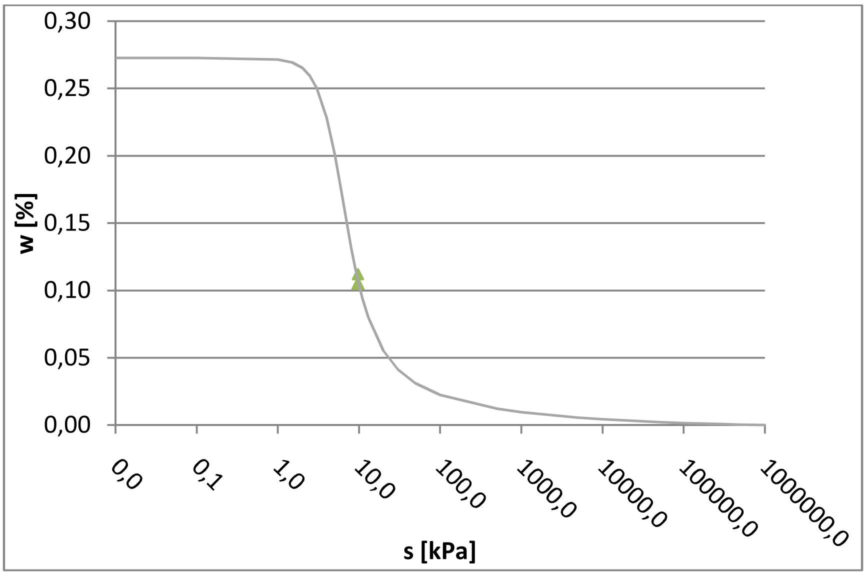


**Fig. 22: SWCC for e = 0.74**

### 3.1.8 Hydraulic conductivity

In order to determine the hydraulic conductivity (k) of the soil at various densities, several tests were run. In addition, the influence of the initial water content at soil preparation - resulting in a different soil structure - on the hydraulic conductivity was investigated. The experiments were performed with falling water head, where the time at certain water heads was measured. The hydraulic conductivity (k) was calculated with the incremental velocities and hydraulic gradients (Table 7).

First, the soil was mixed at particular water content (11.55 % or 18.00 %). Soils with 98 % and 85 % relative Proctor density were tested. A calculated mass of soil was compacted in a cylinder of known volume to a height of 40 mm. Subsequently, the cylinder with the soil specimen was placed on a draining base plate with an additional metal grid. On top of the soil specimen, a filter stone and a metal surcharge were located, and all parts were moved into a plastic cylinder (Fig. 23). The plastic cylinder and the metal cylinder were first filled with water and subsequently the system was closed with a head plate which is connected to the standpipe. Then the specimen was saturated. After the minimum water volume of four times the pore space passed through the specimen, a test was started.

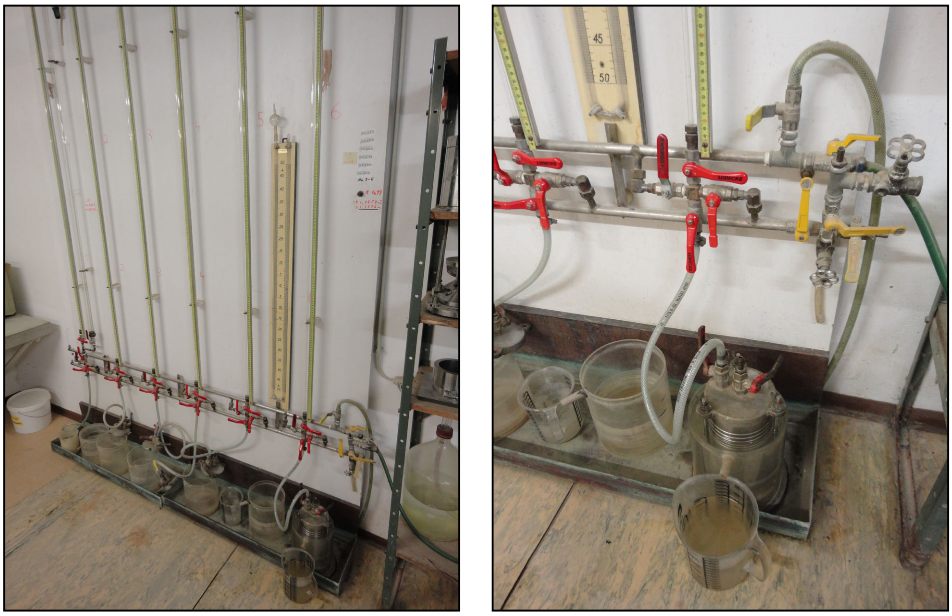

**Fig. 23: Permeability test**

**Table 7: Hydraulic conductivity k**

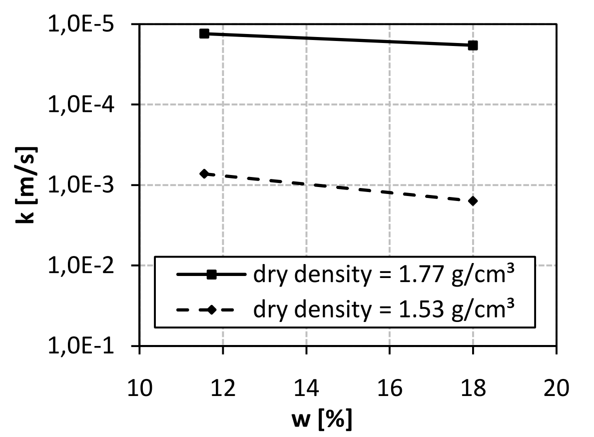


| dry density [g/cm³] | initial water content [%] | k-value [m/s] |
|---|---|---|
| 1.53 | 11.55 | $7.25 \cdot 10^{-4}$ |
| | 18.00 | $1.58 \cdot 10^{-3}$ |
| 1.77 | 11.55 | $1.32 \cdot 10^{-5}$ |
| | 18.00 | $1.84 \cdot 10^{-5}$ |

## 3.2 Soil preparation

To make the test results comparable, a homogenous soil of predefined water content and density was necessary. Natural soil does not provide these properties. Hence the same soil material was used for all experiments and prepared each time with the required properties. In this chapter, the three steps necessary for preparing the slope are described, which are the mixing of the soil with water, the soil compaction and the shaping of the slope.

### 3.2.1 Mixing of model soil

First, the soil was dried in a drying oven and stored in air-tight buckets. Then the required amount of water and soil for obtaining the desired water content was calculated and the water was filled into a watering can. For the process of mixing water and soil, following components were used (Fig. 24): Container (1), Shovel (2), Drilling machine + attachment for mixing the soil (3), Balance (4) and watering can. Some 30 kg of soil were mixed in total, where about 2 kg more soil than required for the model slope was prepared in order to guarantee a sufficient amount of mixed soil.

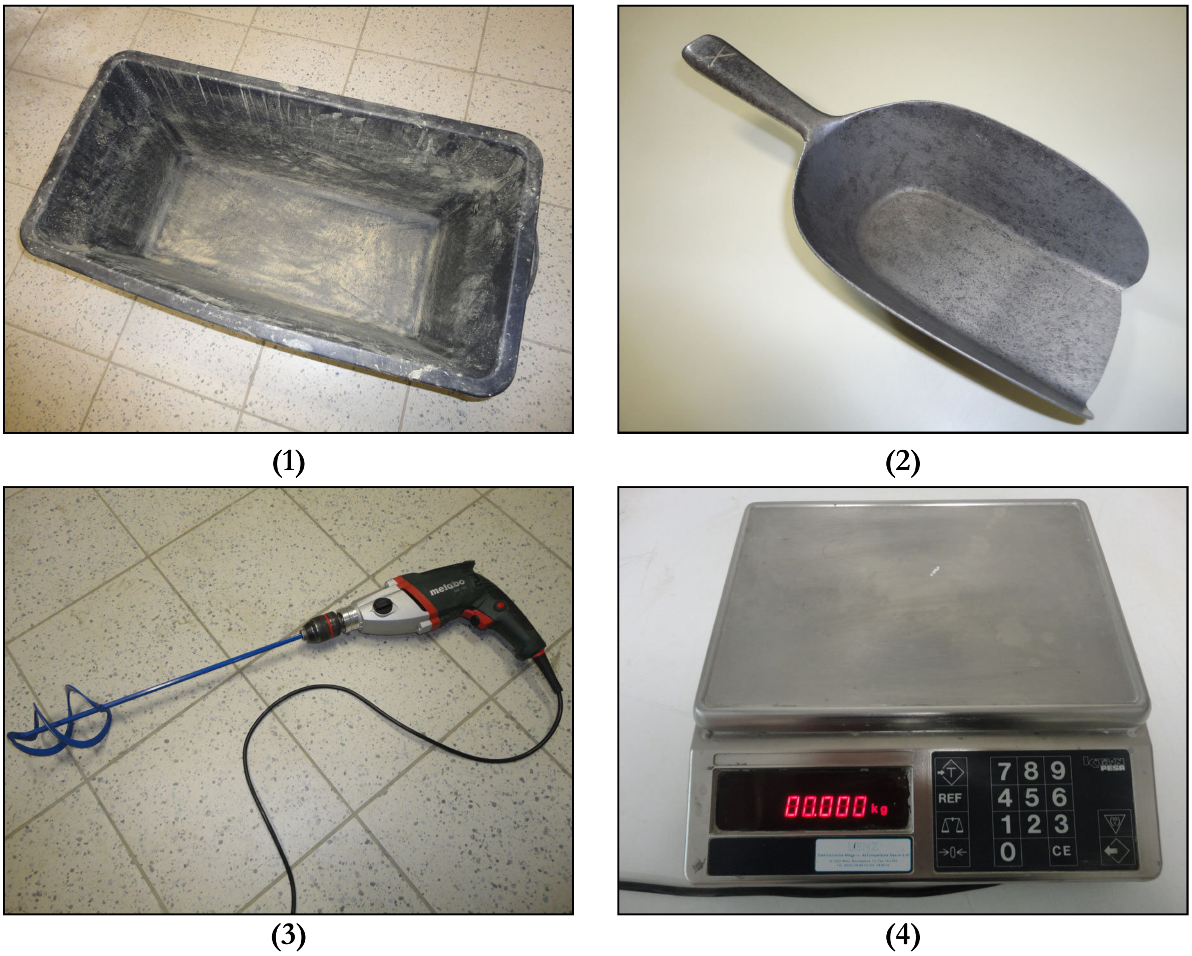


**Fig. 24: Instruments for soil mixing**

The dry soil from the buckets was placed in the container. After each bucket, some water was added from the watering can and mixed with the shovel. In the end, the remaining water was used and the whole soil was mixed with the shovel as well as with the drilling machine.
Subsequently, the soil was filled into five buckets, where each bucket contained exactly the amount of soil necessary for one layer of the soil-model.
Finally, the weight of the remaining wet soil was determined and a calculation was performed in order to control the total process. In doing so, the calculated and the measured total weight were compared. This led to the conclusion that about 50 g of water evaporates during the process of soil-mixing, depending on the air temperature. As a solution, this amount of water was added additionally at the beginning of the process.

### 3.2.2 Soil compaction (moist tamping)

Various methods exist to reconstitute a model soil to the required density. The dry and wet pluviation, the slurry deposition and moist tamping will be discussed in this chapter.
DELLA et al. (2011) describes the dry pluviation, where a funnel of constant height to the surface was used for obtaining loose specimens. Wet pluviation is similar, but the soil is dropped into water. The slurry deposition method was used by BRADSHAW & BAXTER (2007). A slurry with a water content of about 45 % was compacted in a triaxial cell. Moist tamping is a method where the specimen is compacted by layers with defined compaction energy or a defined number of strokes per layer. This method was applied by MULILIS et al. (1977), BRADSHAW & BAXTER (2007) or LADD (1978) for example. LADD (1978) described a variation of this method, the approach of 'undercompation'. It is based on the fact, that layers located at a lower position will be additionally compacted during the compaction of the layers located at higher positions. As a possible solution, LADD (1978) suggests a slightly increasing compaction during the whole process in order to achieve a consistent density.
For the experiments of this research, an approach was chosen, where compaction in layers of 50 mm led to the required density. The density could be established by adding a pre-calculated, exact amount of soil per layer and compacting it to a known volume. This method has the advantage of an exactly defined geometry of layers, enabling a more detailed analysis of the results of the experiments. Moreover, it is relatively time-efficient. One point of consideration is that no soil can be lost during the process of layer preparation, as it would result in a lower density than required. A shortcoming of this method is the possible inhomogeneity of the soil layers. Undercompaction, chosen thickness of the layers and soil structure dependent on the water content during soil preparation are further points, which had to be considered.

In the following, the model soil preparation is described step-by-step, and the advantages and disadvantages are analyzed in detail. A compaction plate with two mounted bubble levels, a plastic fork, a whisk and a proctor hammer were used for this process.

1. Preparing the soil per buckets as described in the previous chapter
2. Filling the model box with the content of one bucket
3. Distributing the material evenly over the whole layer, using the plastic fork and the whisk. Horizontal lines on the inside of the model box and the bubble levels of the compaction plate were used to adjust the soil distribution before compaction
4. Compacting the material to the demanded volume, using a proctor hammer if required. The horizontal lines of the model box indicated the layer boundaries
5. Roughening the surface and additionally scarifying the top section of the layer with the plastic fork in order to achieve a better compound to the next layer
6. Starting again at point 2 and repeating the whole process five times

Additionally to the main steps, an intermediate pre-compaction was performed in the middle of each layer.

Fig. 25 shows the material used for the process of soil compaction.

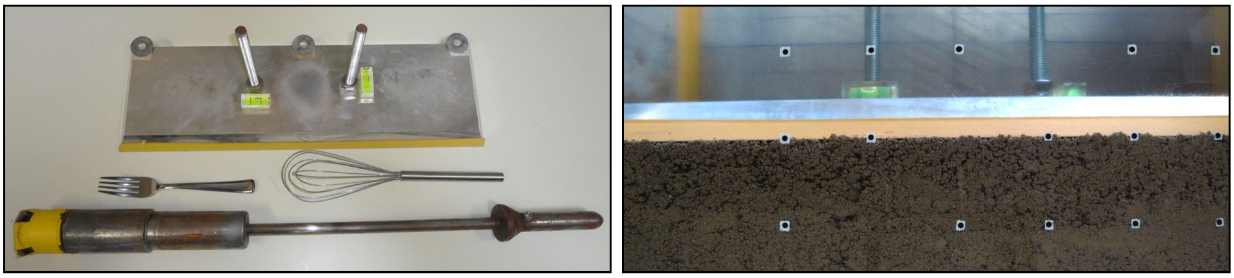

**Fig. 25: Instruments for compaction**

The process of soil preparation and soil compaction is relatively time-efficient. The achieved compound between the layers seems to be sufficient, as no influence on the shape of the slides during failure could be observe, when the process of compaction was conducted correctly. Experiment 9 is an example of a problematic soil model, where the shear band leaves the slope between layer 3 and 4, as layer 4 was compacted stronger.

One of the critical points of this method is the different soil structure which is formed, when compacting soil to the same density at different water content. Both soils of Fig. 26 have a density of 1.53 g/cm$^3$, but the left one has a water content of about 11.55 % and the right one of about 18 %. Hence the different soil structure is a result of the distinct water content. This leads to the conclusion that soils of different water content cannot be considered to be the same, using this method of compaction.

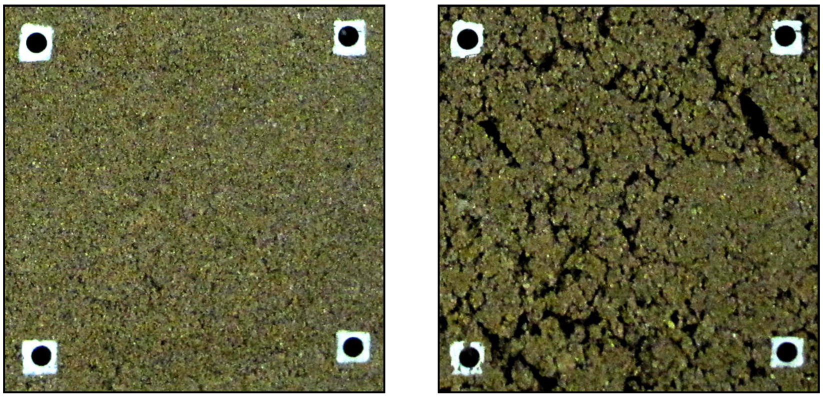

**Fig. 26: Soil structure**

Fig. 27 illustrates the results of a PIV-analysis of pictures taken during the compaction of a soil model with a density of 1.53 g/cm$^3$ and a water content of 18 %. The green, purple and blue lines describe the settlements of the already existing layers during the compaction of the new layer. The red line shows the compaction of the soil in the zone between 100 mm and 200 mm during the process of compacting the last three layers. The top layer was compacted significantly less, as the layer below was compacted more than required. This fact shows the importance of an exact working procedure in order to obtain a consistent soil density. Such effects are automatically corrected in the centrifuge to a certain amount, as the less compacted parts of the soil are the ones with more settlements which finally leads to a more consistent soil density. Avoiding inconsistencies in the first place is obviously recommended.

Undercompaction is a topic already discussed above. The layer in the zone between 150 mm and 200 mm shows a total, cumulated compaction of 1 mm during the preparation of the three layers above it. This shortcoming can be solved by using the approach of undercompaction as described above.

The ideal thickness of one layer is another topic of interest. Soil models with thicker layers are faster to establish. Thinner layers lead to a more consistent density. LADD (1978) suggests not exceeding 25 mm per layer for his specimens of diameters less than 102 mm. For this research, layers of 50 mm were chosen, and most of the time a first pre-compaction was conducted at about half of the height of each layer. Fig. 27 shows that the compaction decreases with the depth and reaches a minimum after about 20 to 30 mm. For further research with this soil, decreasing the thickness of the layers could lead to an improvement of the compaction process.

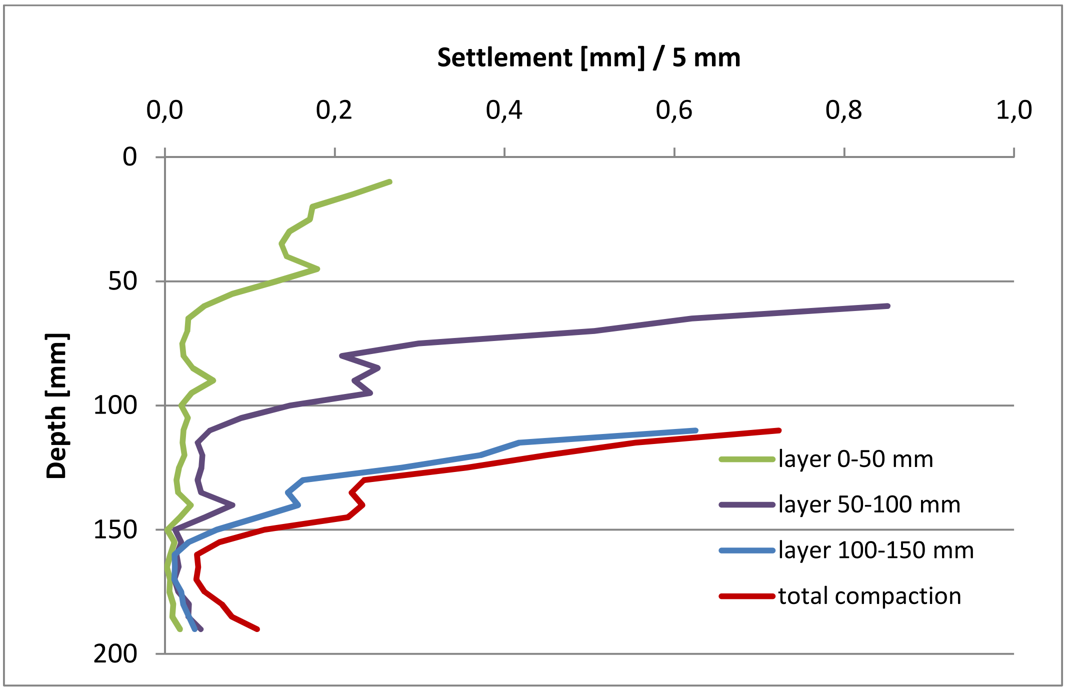


**Fig. 27: Compaction by layer**

### 3.2.3 Shaping the model

After soil compaction, the final shape of the slope had to be established. For this purpose, templates of impregnated wood and a knife were used. The front and the back wall of the model box had to be removed and were replaced by the templates, which were fixed with clamps (Fig. 28). At first, the surplus soil was removed. Then the exact surface of the final shape was cut by using both templates. In doing so, zig-zag movements were made with the knife in order to avoid smearing the surface. The upper four layers formed the slope whereas the lowest layer formed the basement. Finally, the templates were removed and the back und front walls of the model box were mounted again.

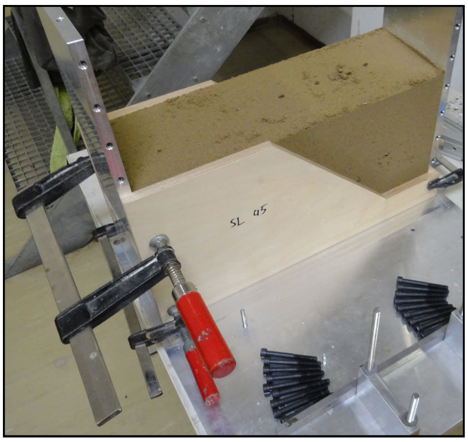

**Fig. 28: Slope cutting**

## 3.3 Test configuration

### 3.3.1 Model box

The chosen dimensions of the model box (Fig. 29) provide plane-strain conditions for the slope. For minimizing wall friction, the front and the back wall were coated with silicone oil each time a new slope was built. The inner dimensions of the model box are 480 mm x 155 mm in length and width and 450 mm of height. The aluminum ground plate, designed for fitting the swinging basket of the centrifuge, is 538 mm wide and long and has a thickness of 12 mm. The two smaller side walls, the back wall, the frame and the covering plate are made of aluminum with a thickness of 15 mm. The transparent front wall is constructed of 30 mm thick acrylic glass. Black points with white background are painted in a grid of 50 mm x 50 mm on the inside of the acrylic glass for the PIV-analysis. The components are connected with screws. Summing up all parts of the box, it weights 40.353 kg (Table 8). The arrangement of the parts results in an asymmetric distribution of the weight.

**Table 8: Weight of model box**

| | | |
|---|---|---|
| ground plate + screws for lights + construction for camera | 11.122 | kg |
| back wall | 9.099 | kg |
| side wall left | 2.683 | kg |
| side wall right | 2.683 | kg |
| frame | 2.094 | kg |
| front wall (acrylic glass) | 8.034 | kg |
| covering plate | 4.638 | kg |
| **total** | **40.353** | **kg** |

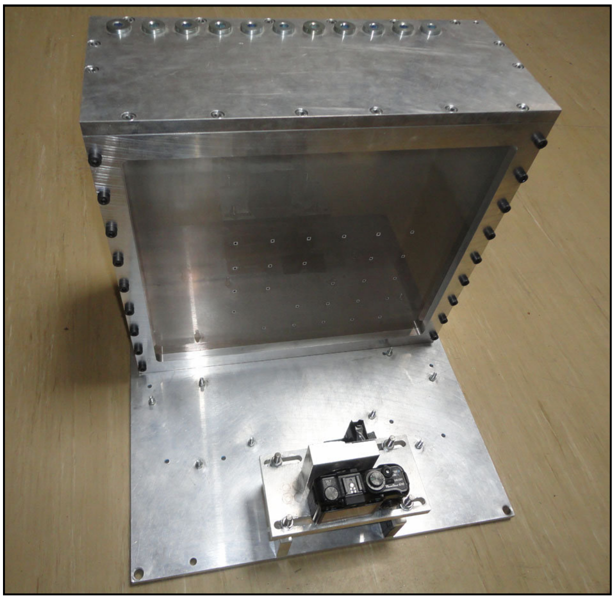

**Fig. 29: Model box with mounted camera**

The box had to be waterproof, or, failing that, water could leave the box during the experiments as a result of the high centrifugal forces.

Generally, it was assumed that the components of the box could be pressed together with the screws and the box would be waterproof. The test on soil with the initial water content of about 11.55 % showed that little water was lost. However, for tests with about w = 18 % significant water loss was observed. During experiment 8 (max. of scaling-factor n = 100.9), the water content at the toe of the slope reduced from the initial value of 11.25 % to around 11.00 % which could be accepted. For experiment 9 (max. of scaling-factor n = 99.4), however, the water content reduced from 18 % to 13 %. This loss was found too high.

As a first attempt, adhesive tape was used inside the box were the parts join together. This turned out to reduce the loss of water slightly but not sufficiently. The reason might be that during the process of slope cutting, the front and back walls have to be removed and afterwards mounted again. Probably the cohesive tape cannot stick to the walls strong enough after this process.

The second try was the construction of a waterproof basin, which reached up until the end of the lowest layer. This approach reduced the loss of water significantly, however, with two ensuing problems. First, the basin was demolished by coarse soil particles. This can be resolved by strengthening the basin. Secondly, the parts of the box above the basin kept leaking. Hence a solution had to be found, where all joints of the box could be sealed.

Teflon stripes with a thickness of about 0.1 mm were placed between the parts in order to seal the joints. This approach was the most successful and could reduce the reduction of water content to around 2 % at the toe of the slope for an initial water content of about 18 %.

Independent of the soil used and the method of sealing, the water loss was larger at the front side. This is ascribed to the fact that the back wall was mounted to the bottom plate with extra-screws, which was not the case for the front wall.

Fig. 30 shows the three approaches of sealing, chronologically from left to right as described above.

**Fig. 30: Sealing methods**

### 3.3.2 Camera

The main camera used is a Canon PowerShot G10. It was mounted on the ground plate with an aluminum construction (Fig. 31). This structure had to fulfill the following requirements:

- High stiffness
- Fixation of the lens, in order to obtain the same image section for each picture, as due to the high centrifugal forces, a deformation of the lens was caused
- Elevated position of the camera, for the purpose of obtaining pictures, which show the part of the model required for further processing with the PIV-analysis
- Horizontal and vertical adjustment of the camera possible
- Orthogonal alignment of the camera to the object plane

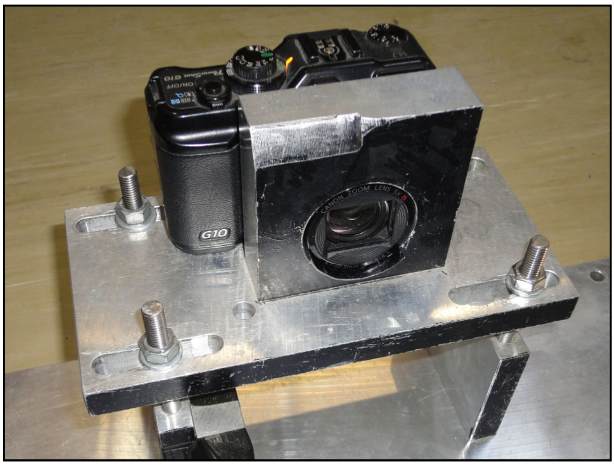


**Fig. 31: Camera**

All points named above could be fulfilled by the construction. The camera was fixed with a screw and the thread normally used for a tripod. For fastening the lens, a rounded metal piece was inserted between the lens and the aluminum frame. In spite of this, however, significant shift of the field of view during acceleration could still be observed. Since an exterior deformation was unlikely, an inner deformation of the lens had to be the cause. This shortcoming could be compensated by selecting more images for the PIV-analysis in order to consider these deformations, as described later.

During the experiments, pictures were taken every five seconds. The camera settings are listed in Table 9.

**Table 9: Camera settings**

| | |
|---|---|
| Exposure time | 1/160 s |
| Aperture | 2.8 |
| ISO | 400 |
| Size/Quality | Medium1/fine |
| White balance | Tungsten |
| Auto-focus distance | Close-up |
| Focus points | Auto |
| Flash | Off |

The camera was remote controlled. This was possible as the camera was connected to a laptop in the centrifuge which itself was connected to an external computer via the slip rings of the centrifuge.

For experiment 5, a high speed camera of the model Casio Exilim was used, enabling to document the failure mechanism with a frame rate of 120 pictures per second. The high frame rate implied a lower photo quality, which obstructed the proper pre-processing of these pictures. Nevertheless, they were valuable for visualizing the failure process.

### 3.3.3 Lights

A lighting system was necessary to obtain pictures with good quality, enabling the processing with the PIV-analysis (Fig. 32).

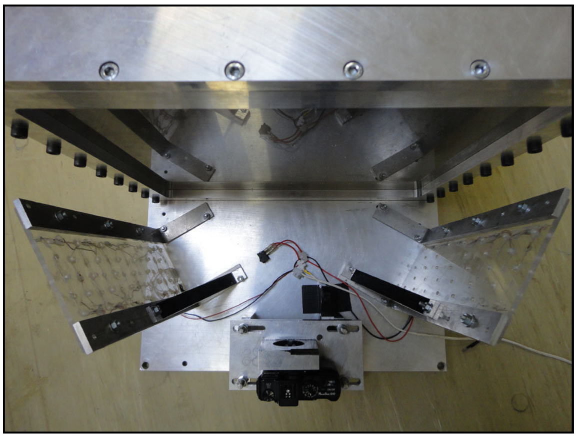

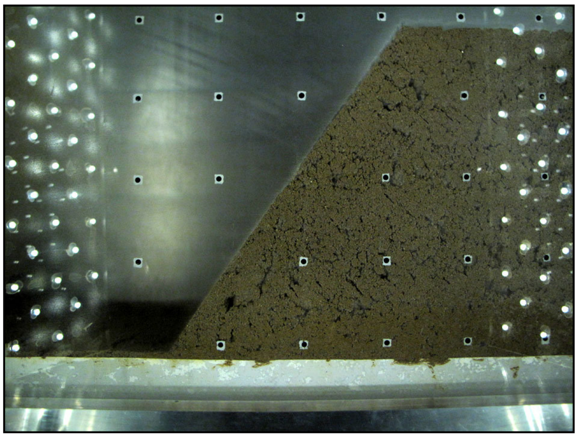

**Fig. 32: Lighting system and caused reflections**

Developing a proper lighting system is a challenging task, as sometimes conflicting objectives had to be fulfilled:

- Strong lights
- Little demand for energy
- Big surface of the system in order to produce an evenly distributed light

- Little reflections
- Rigid system, which resists the enhanced g-forces and vibrations during the experiments caused by the centrifuge

Single LED-lights were mounted and connected on acrylic glass, reinforced by an aluminum construction, which furthermore enables to connect the panels with the ground plate of the model box. Two of those panels were constructed. Various problems occurred during the process of developing this system.

At the beginning of the experiments, reaching higher g-levels always caused the breakdown of the lighting system and its fuse was blown. As a first attempt, the energy supply was changed from battery to external supply via the slip rings, since it was assumed, that the batteries could not resist the high g-forces. This was not successful and as a next try, the cable system was fixed more carefully with tape to the model box, to avoid a power interruption due to the high vibrations at increased g-levels. Finally, more stable panels of smaller height were chosen. This solved the problem, as they were less prone to vibrations but still provided a sufficient amount of light. In parallel, the source of vibrations was eliminated, as the counterweights were distributed in an improved way.

Another problem was the reflection caused by the lights itself as one can see on the right picture of Fig. 32. Two different positions of the panels were tried in order to find a compromise between brightness of the pictures and reflections which had to be accepted. Positioning the panels parallel to the model box would cause heavy reflections, while turning them 90 would avoid nearly all reflections but leads to a low lighting quality. The positions shown in Fig. 32 were finally chosen.

Additionally, reflections were caused by the aluminum parts of the panels and the camera system. This problem could easily be solved by painting them with black color.

## 3.4 Centrifuge at BOKU

The centrifuge used for the experiments (Fig. 33) is located in the laboratory of the Institute of Geotechnical Engineering (IGT) at the University of Natural Resources and Life Sciences (BOKU), Vienna. It is a beam-type centrifuge, installed in the late eighties and consists of a beam with two swinging platforms on its ends. The beam is mounted on an engine-driven axis and the construction is covered in a metal shell. The centrifuge can be remote controlled from a separate room, using slip rings for establishing the connection between the rotating parts of the centrifuge and the non-moving cables at the outside of it. It is of high importance that nobody is in the centrifuge room during flight as the model box speeds up to 125.5 km/h at 100 g or even 177.4 km/h at 200 g.


**Fig. 33: Centrifuge of the IGT**

Several experiments in various fields of geotechnical experimentation have already been conducted with this centrifuge. For instance silo modeling by MATHEWS (2013), geosynthetic reinforced slopes by AKLIK (2012), shallow tunneling by IDINGER (2010), or testing of bio-engineering methods by STAUBMANN (2008). The centrifuge offers an effective radius of 1.3 m, measured from the rotation axis to the swinging platform during flight. Depending on the weight of the model, various maximum g-levels are possible. The absolute maximum is 200 g. The max. payload is 90 kg and the max. load capacity are 10,000 g-kg, where the load capacity is defined as the result of a multiplication of the payload and the g-level. Table 10 gives an overview of important parameters of the centrifuge.

Table 10: Specifications of centrifuge

| | | |
|---|---|---|
| Diameter | 3.0 | [m] |
| Radius (axis to end of swinging basket) | 1.3 | [m] |
| Max. acceleration | 200 | [g] |
| Max. angular velocity | 400 | [rpm] |
| Max load capacity | 10,000 | [g-kg] |
| Max. payload | 90 | [kg] |
| Max. model dimensions (w/d/h) | 540/560/560 | [mm] |
| Full bridge connections | 5 | [pcs] |
| Half bridge connections | 5 | [pcs] |
| Power supply, max. 24 V, 5 A | 6 | [pcs] |

A comparison with other centrifuges shows, that the one of the IGT is relatively small (data from MUIR WOOD 2004):

- Radius 9.14 m (Owner: U Calif, Davis; USA)
- Max. 600 g acceleration (Owner: ISMES; Italy)
- 2.769 tons max. payload (Owner: Min of Trans, PARI; Japan)

The advantage of smaller dimensions is that the model can be handled easier. One disadvantage is that less equipment can be placed on and around the swinging basket. Another disadvantage is that the derivations from the prototype stresses as illustrated in Fig. 37 are stronger when the radius is smaller.

### 3.4.1 Rotation-speed of centrifuge and scaling factor n

Fig. 34 shows n as a function of the rpm. The knowledge of this function is crucial, as the experiments are conducted with a certain scaling factor n, but the speed of the centrifuge is adjusted by the rpm-value.

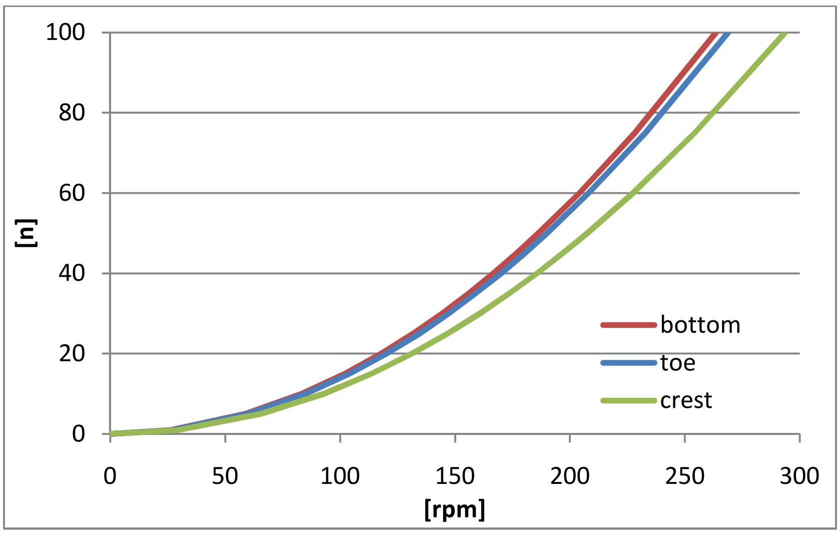


Fig. 34: n as a function of the rpm

The underlying formulas of Fig. 34 are the following:

$$n * g = \omega^2 * r$$

where:

$$\omega = 2\pi * U/60$$

$$g = 9.81\ m/s^2$$

resulting in:

$$n = 1.118 * 10^3 * U^2 * r$$

where:

$$U = rpm\ (revolutions\ per\ minute)$$

$$r\ (crest) = 1.038\ m$$

$$r\ (toe) = 1.238\ m$$

$$r\ (bottom) = 1.288\ m$$

In the conducted research, n was defined for r (toe) = 1.238 m.

Slopes in the presented test series were forced to fail by an increase of the self-weight. Failure was triggered by a step-wise rising of the g-level.

Fig. 35 shows n over the elapsed time of experiment 12. At 10, 20 and 30 n, a break of a few minutes was made. The factor n does not increase in a linear way, since the rpm are rising constantly, but n is not, as explained by Fig. 34.

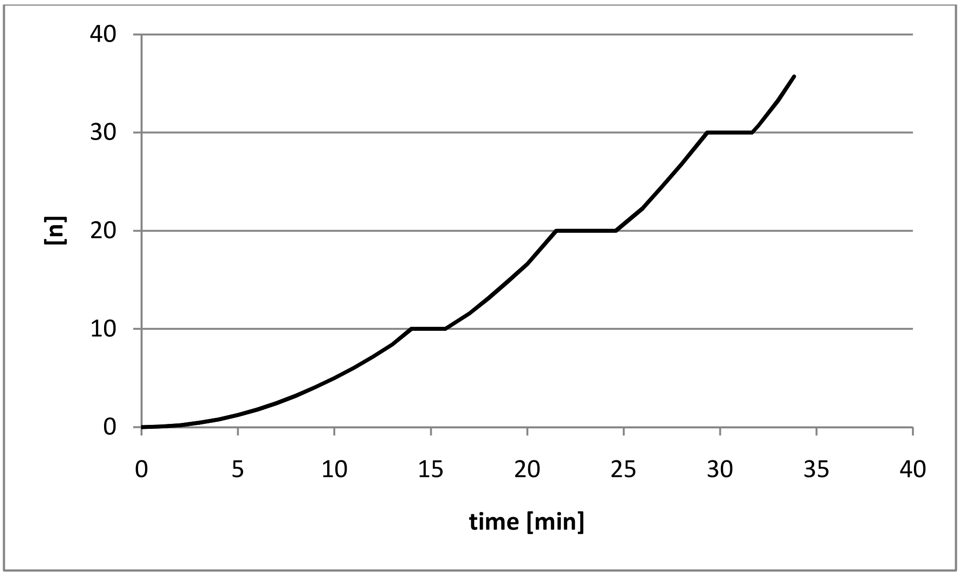


**Fig. 35: n over time at experiment 12**

### 3.4.2 Control of the centrifuge

In the control room the speed of the centrifuge can be navigated manually with the control panel (Fig. 36) or with a computer program. For the experiments, a constantly increasing rate of 0.1 rpm/s was chosen, controlled by using the computer. In the event of a crash of the computer system manual adjustment of the rpm could be performed.


**Fig. 36: Control panel**

Next to the control panel as well as on the centrifuge, instructions for the proper use are placed. In the following, a step-by-step description of how to operate the centrifuge is given:

1. Mounting the model box in the centrifuge and checking the inside for any loose material. If necessary, removing or securing it
2. Adjusting the counterweight of the model, using big iron weights as well as small metal pieces for finer modifications. A control of balance is performed by measuring the height from the bottom of the metal shell to the edge of the beam at both sides
3. Closing the upper and the front door of the centrifuge
4. Activating the engine of the centrifuge (probably it is necessary to switch it on and off several times, until the sound of the engine can be heard)
5. Locking the door to the centrifuge room after checking that nobody is inside
6. Switching from remote to manual on the panel in the control room
7. Turning the starting key clockwise
8. Switching from stop to run
9. Switching from manual to remote and using the computer program for increasing the speed of the centrifuge

After the experiment

1. Switching from manual to remote on the control panel
2. Turning down the speed to nearly 0 rpm
3. Shutting down the system (switching to stop, turning back the starting key)

4. Entering the centrifuge room, turning off the engine and opening the doors of the centrifuge

### 3.4.3 Problems and solutions

During the first experiments, the centrifuge switched into unbalanced-mode when a value of 230 rpm (about 75 g) was reached, causing an automatic shut down. The source of the unbalanced error was found to result from poorly adjusted counterweights. In order to avoid this problem, the metal weights were distributed as similar as possible to the asymmetric design of the model box on the opposite side of the beam. Afterwards, the unbalanced-mode occurred at around 100 g which was not a problem anymore, as all experiments were ended at this speed or earlier.

A general problem occurring at centrifugal experiments is the fact that the radius of rotation changes within the model height. Hence, the stress does not increase in a linear way (Fig. 37). It is only correct at the crest as well as at a defined point. For these experiments, this point was located at the toe of the slope as the failure initiation starts there. The zone above it shows lower stress levels due to a lower radius, and the zone underneath shows higher stresses due to a higher radius. This is an error, which can and must be accepted, as it is relatively low. Depending on n and the density of the soil, the absolute values of the stress vary, but for the experiments of this research the distribution will always be as shown in Fig. 37.

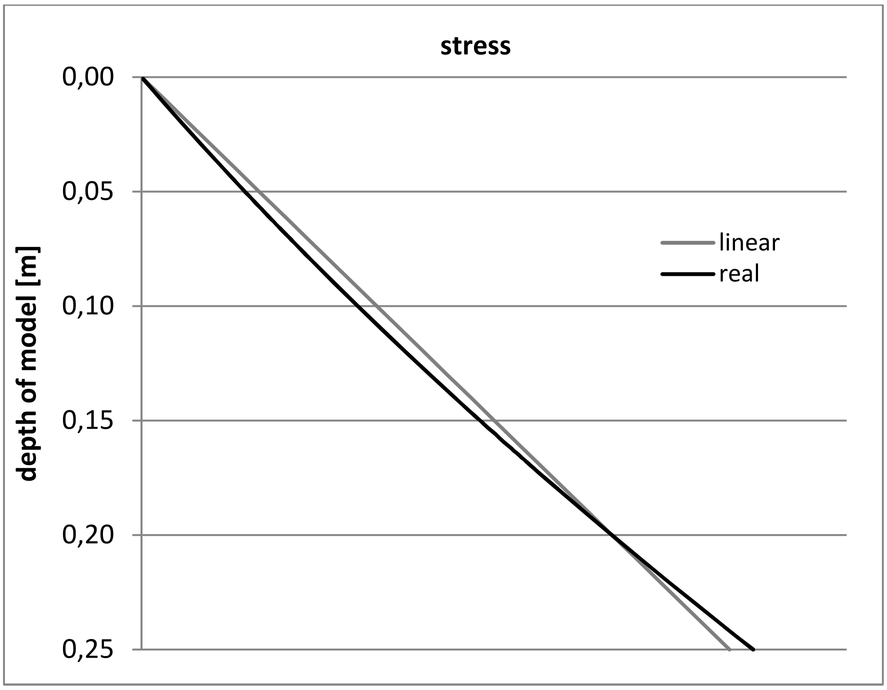


**Fig. 37: Error of stress due to changing radius**

Additionally to the model box and its components, a laptop was placed nearby the axis and connected by USB-cable to the camera in order to be able to remote-control the camera. Furthermore, a surveying webcam was installed, pointing away from the axis into the direction of the swinging basket. It was also connected to the laptop, and the laptop was connected by Ethernet-cable over the slip rings to the computer in the control room. The surveying of the whole experiment was crucial due to the possibility of a cable getting stuck during the movement of the swinging basket. Furthermore, the upswing angle of the model had to be checked constantly. Establishing a proper upswing angle was essential for two reasons. First, an upswing angle of more than 90 degrees would involve the risk of a fracture of the stopper, installed in order to avoid an over twist of the basket. Second, an upswing angle of significantly less than 90 degrees would lead to a wrong state of stress within the slope model. Two measures for checking this angle were applied (Fig. 38). Left hand side, the stopper with a pencil lead taped on it can be seen. A broken pencil lead would have signaled an upswing angle of 90 degrees or more. This was never the case during the experiments. Right hand side, a paper with lines, signaling the respective upswing angle is illustrated. Using the video from the surveying camera, the current angle during the experiment could be determined while being in the control room.

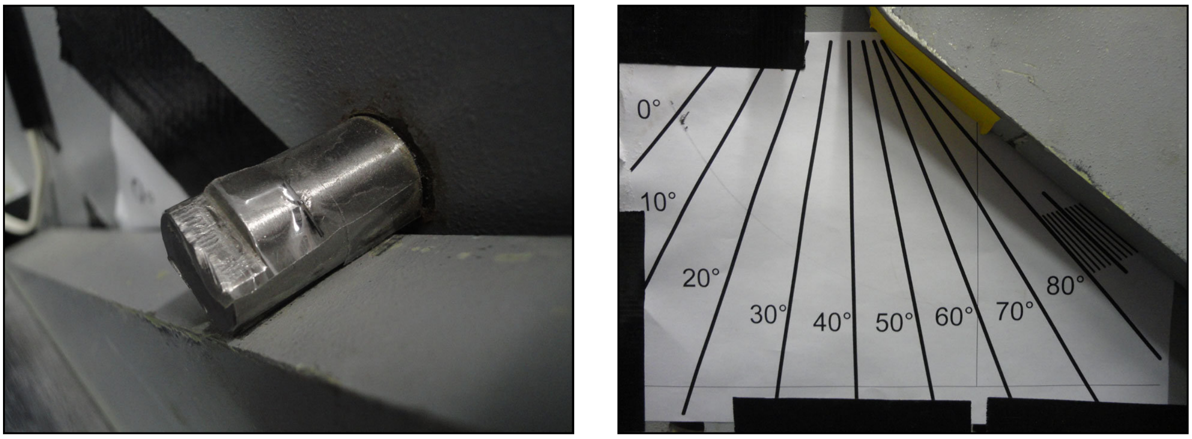


**Fig. 38: Measures for checking the upswing angle**

The theoretical upswing angel is discussed in Chapter 2.3.3. However, friction and an unequally distributed weight of the model during real experiments have to be taken into account. The measurement of the actual angle led to the conclusion, that at the time of failure of the slope, the angle always exceeded 89 degrees. This can be reasoned by the fact, that the weight of the model box was distributed in a way, which supported the upswing of it. This was achieved by positioning the higher part of the slope on the inside of the swinging basket.

Generally, it has to be taken into account that the vertical force of $1 \cdot g$ occurs additionally to the horizontal force $n \cdot g$ during the flight of the centrifuge.

## 3.5 Methods for model validation

Before and after each experiment, penetrometer tests and the determination of the water content per layer were conducted. This was necessary to verify the quality of the soil model preparation and to provide data for the subsequent interpretation of the experimental results.

### 3.5.1 Penetrometer tests

The consistency in density within and between the layers of the model was tested at various points, before and after the experiment in the centrifuge, respectively. Fig. 39 shows the penetrometer during a test at the left hand side and the tip of the penetrometer on the right hand side with markers at every 10 mm.

**Fig. 39: Penetrometer**

The tip has a larger diameter than the upper part in order to minimize the wall friction of the instrument during the test. Every centimeter was marked with a black ring as the strikes per cm were counted. The compaction energy was adjusted each time. For a denser soil, more weight was used and for a looser one, less weight was necessary. An overestimation of the required weight led to a coarse resolution and an underestimation to a high rate of strikes, which caused a time consuming testing procedure. At a certain height, a stopper was placed on the instrument in order to be able to drop the weight each time at the same distance.

For the purpose of illustrating the test results, a normalized diagram was created, were the maximal number of strikes equals the value one. The mean of several tests was calculated. On the left photo of Fig. 39 one can see a hole of an already finished test. Fig. 40 shows the result of the penetrometer test of experiment 10. First, a higher number of strikes can be observed after the experiment, resulting from the compaction process caused by the centrifugal forces during the experiment. Second, the layer between 100 mm and 150 mm shows inconsistencies.

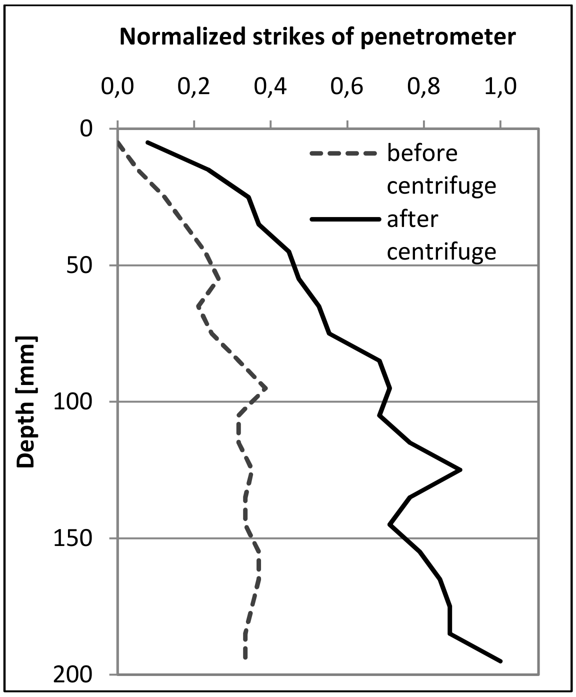


**Fig. 40: Result of penetrometer test**

### 3.5.2 Water content

Before cutting the slope, soil samples were taken from the part of the soil which was about to be removed. This part consisted of four layers. From each layer, four samples were taken from the front side and four from the back side, distributed over the whole layer. Additionally, four samples were taken from the top. Each group of four samples was analyzed together by putting the material into a bowl, weighting it, drying it in the drying oven and weighting it again afterwards. This procedure led to nine values of water content for the soil before the experiment. After the experiment, the same procedure was repeated, this time leading to eleven values, as from the bottom layer samples could be taken as well.

The instrument used for taking the samples was an apple corer (Fig. 41). One layer has a height of 50 mm. As the external diameter of the apple corer is 20 mm, it was suitable for receiving samples of one specific layer. Fig. 42 shows a model before slope cutting and after the samples were taken. In Fig. 43 the results of experiment 7 are presented. The loss of water during the experiment which was caused by leakage of the model box is visible. Furthermore, the differences of the front and the back side can be observed.

Additionally to the tests with the apple corer, at some experiments the complete soil material of the slope was dried in the drying oven after the experiment. The water contents measured this way are in accordance with the values measured with the apple corer.

Fig. 41: Apple corer

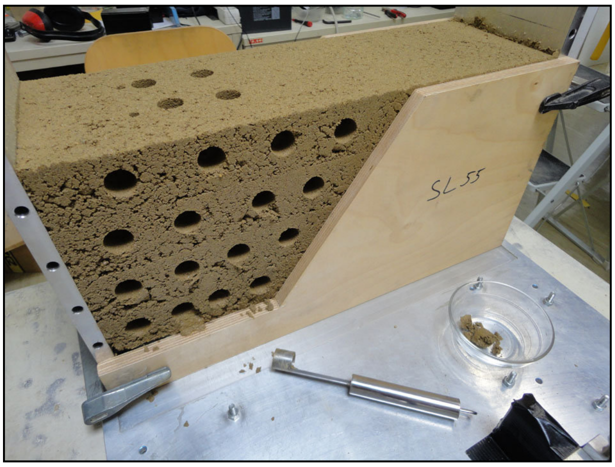


Fig. 42: Model with samples taken

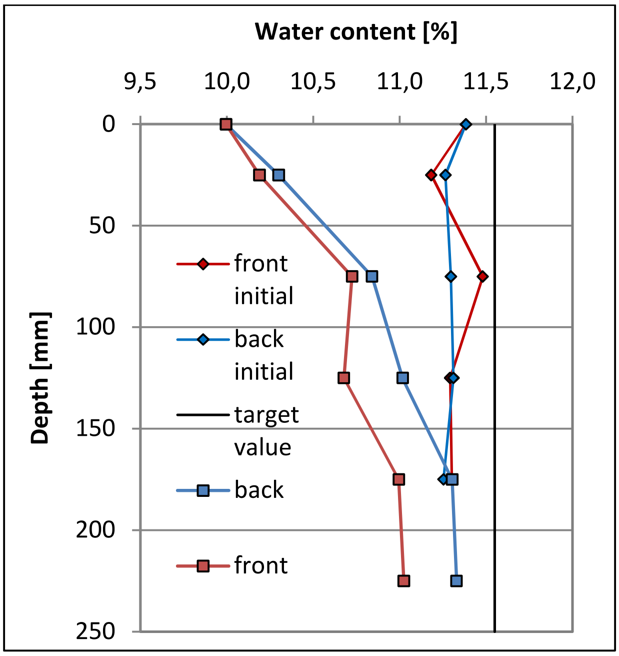


Fig. 43: Results of water content tests

## 3.6 Data processing

The pictures which were taken every five seconds during the experiments were mainly processed with Matlab (THE MATHWORKS, INC). In order to follow the pre-deformations, the Matlab code introduced in WHITE & TAKE (2002) was used. They developed these files for applying a method called PIV (Particle Image Velocimetry). With self-created Matlab-scripts (Appendix II), the vertical settlements per layers of 5 mm were calculated afterwards. Fig. 44 illustrates the schematic layout of the analyzed region. The red frame stands for the area of a photo. The grey area (bright plus dark) for the whole model and the dark grey area is the part which was actually analyzed. This area was chosen, as all important soil movements could be captured. Besides, an area of higher geometrical complexity would have led to wrong results due to interpolation effects of the PIV software.

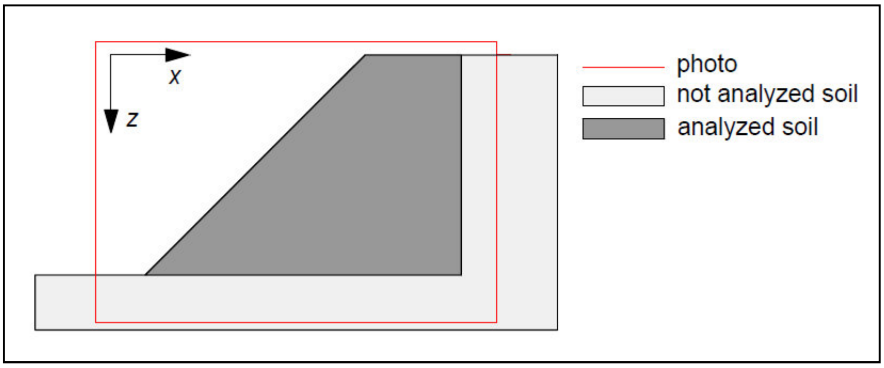


**Fig. 44: Analyzed area**

### 3.6.1 PIV-Analysis

In the following chapter, the necessary steps as well as the considerations and problems during data processing with the GeoPIV-analysis from WHITE & TAKE (2002) are described.

**Selection of proper images**

The relevant pre-failure-deformations occur in the time immediately before actual failure. Hence, all pictures of the last 50 seconds prior to failure were chosen for processing. Prior to that, pictures with a difference of 10 g were selected. In times of lens-deformation due to the rising centrifugal forces, additional pictures had to be chosen for being able to describe the movement. This especially occurred in vertical direction during the rise up to n = 4 and in horizontal direction between n = 10 and n = 20. Such movement could be eliminated from the actual soil deformation, using the point markers on the acrylic glass.

**Defining the mesh of patches**

The PIV-analysis works with patches, defined parts of the images of which the location is tracked during the time of the experiment. The size as well as the distance to each other can be chosen.

The more and smaller patches are used, the finer will be the resolution. But the computation time is longer and the results of the strain analysis are not necessarily better.

Fig. 45 shows the incremental maximum shear strain from all pictures of experiment 7. On the left side, a patch-size of 50 pixels was chosen, where on the right side, the strains of the same experiment with a patch size of 40 pixels can be seen. The advantage of the smaller patch size is the fact, that the shear-band is narrower and shows higher values which make it more visible. On the contrary, the whole model appears to be patchy. As the shear band can sufficiently be detected and the computation time is significantly lower, a patch-size of 50 pixels was used for the analysis of all experiments.

The distance of the patches to each other was set in a way, which left no areas without patches covering them. Hence, the whole model was analyzed.

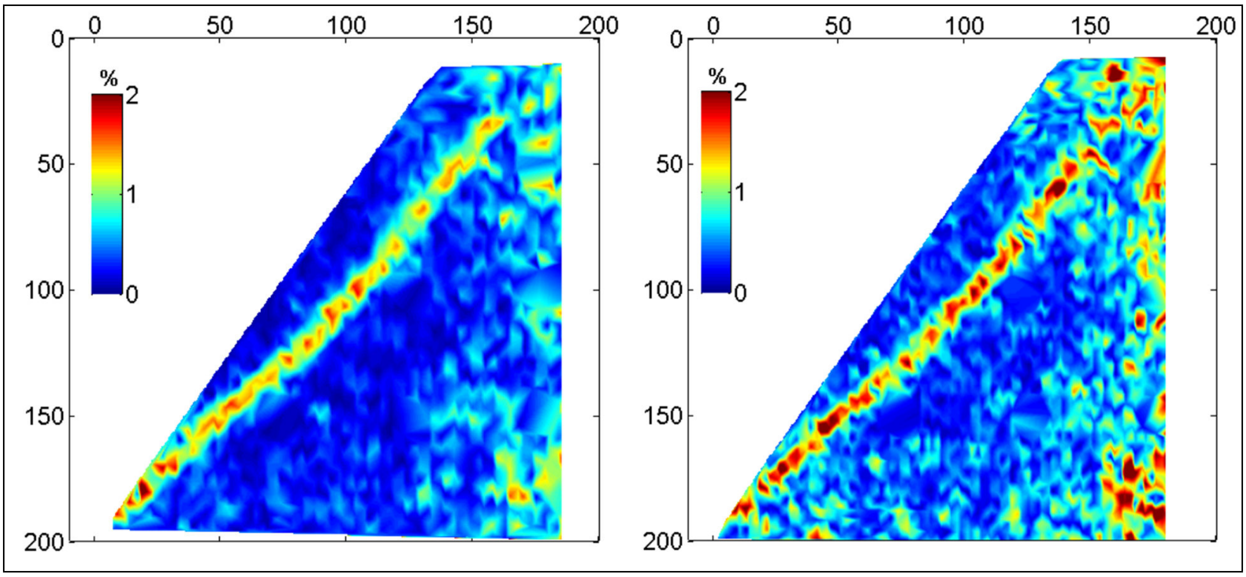


**Fig. 45: Strains with different patch-sizes**

### Analysis of the pictures

During the analysis, the program searches for similar patterns in brightness within the distance of a pre-defined search zone. This zone was determined with 30 pixels for most experiments. The result of soil deformation can be displayed by a vector field, showing the movement of patches.

### Removing wild vectors

As a separate step, vectors of this field, which are obviously wrong, have to be visually detected and manually removed. Such vectors are caused by non-moving point markers or reflections of the lighting system, for instance. The visualized vector-fields of the results always show gaps, were the point markers are located as those vectors had to be removed.

**Correction of image distortion and movement of lens**

Black point markers with white background at known real-scale coordinates and a diameter of about 3 mm are used for this purpose (Fig. 46).

**Fig. 46: Point marker**

First, they have to be tagged manually, and then the exact centers are detected semi-automatically by using the high difference in brightness of white and black parts of the markers. Similar to the analysis of the soil movement, the positions of the markers are tracked over all images. Finally, the real x- and y-values are assigned to the points, and the undistorted positions of the patches are calculated.

**Illustration of results**

The vector-fields were thinned out before plotting them as otherwise the amount of arrows would have been too high. For this purpose, a Matlab-script (Appendix II) was written to fulfill this task. It automatically removes every second vector and the correct offset from line to line was taken into account. Subsequently, the vector field was plotted.

Three different types of strains can be calculated and visualized. The total maximum shear strain (TMSS), the total volumetric strain (TVS) and the incremental maximum shear strain (IMSS). The TMSS sums up all strains until a certain image, the IMSS plots the strains between an image and the one before it. With the TVS, changes in volume can be visualized.

Additionally, a Matlab-script was created for separating the horizontal and vertical movements.

### 3.6.2 Calculation of settlements

Vertical settlements over model height are of special interest, as inconsistencies in density can be detected. Furthermore, the general change in density during the experiments can be back-calculated. Matlab-scripts (Appendix II) were written in order to obtain settlements over the slope height in 5 mm increments. The value of 5 mm results from the patch size.

In the course of the GeoPIV-analysis, 3-dimensional arrays of the x- and y-coordinates from the patches during movement are created. Each line contains the data of a patch, each row the data per image and the third dimension of the array divides the data in x- and y-coordinates. Using these arrays, the cumulated as well as the settlements per 5 mm could be calculated.

# 4 Results and Discussion

## 4.1 Conducted experiments - an overview

Table 11 and Table 12 contain important data of the conducted experiments. In Appendix I, more detailed data is presented for relevant experiments. Due to optimization processes, not all experiments could be used for further analysis.

**Table 11: Overview of experiments - part 1**

| | |
|---|---|
| **1** | Inclination [deg] |
| **2.1** | Dry density $\rho_d$ [g/cm³] – before centrifuge |
| **2.2** | Dry density $\rho_d$ [g/cm³] – after centrifuge |
| **3.1** | Water content w [%] – soil preparation |
| **3.2** | Water content w [%] – before centrifuge (mean) |
| **3.3** | Water content w [%] – after centrifuge (mean) |
| **3.4** | Water content w [%] – after centrifuge (layer at toe) |
| **4.1** | Max. revolutions per minute [rpm] |
| **4.2** | Max. g-level [g] |
| **4.3** | Max. height [m] |
| **5** | Sealing system (none = n, tape inside = ti, basin = b, tape between = tb) |
| **6** | Failure (Yes/No) |

**Table 12: Overview of experiments - part 2**

| Nr | 1 | 2.1 | 2.2 | 3.1 | 3.2 | 3.3 | 3.4 | 4.1 | 4.2 | 4.3 | 5 | 6 |
|---|---|---|---|---|---|---|---|---|---|---|---|---|
| 01 | 55 | 1.53 | - | - | 11.00 | 10.51 | 11.01 | 262.0 | 95.0 | 19.0 | n | N |
| 02 | 55 | 1.53 | - | 11.53 | 11.13 | - | - | 270.0 | 100.9 | 20.2 | n | N |
| 03 | 55 | 1.40 | 1.42 | 11.06 | 11.16 | 10.98 | 11.42 | 126.0 | 22.0 | 4.4 | n | Y |
| 04 | 55 | 1.45 | 1.48 | 11.53 | 11.36 | 10.98 | 11.36 | 167.0 | 38.6 | 7.7 | n | Y |
| 05 | 55 | 1.45 | 1.48 | 11.62 | 11.31 | 10.92 | 11.34 | 168.5 | 39.3 | 7.9 | n | Y |
| 06 | 55 | 1.50 | 1.51 | 11.63 | 11.22 | 10.91 | 11.15 | 204.1 | 57.7 | 11.5 | n | Y |
| 07 | 55 | 1.53 | 1.54 | 11.66 | 11.30 | 10.76 | 11.15 | 209.6 | 60.8 | 12.2 | n | Y |
| 08 | 45 | 1.45 | 1.51 | 11.63 | 11.10 | 10.47 | 11.01 | 270.0 | 100.9 | 20.2 | n | N |
| 09 | 55 | 1.53 | 1.58 | 18.12 | 17.36 | 11.90 | 13.00 | 268.0 | 99.4 | 19.9 | n | N |
| 10 | 55 | 1.45 | 1.53 | 17.86 | 17.05 | 14.15 | 15.63 | 188.6 | 49.2 | 9.8 | ti | Y |
| 11 | 55 | 1.53 | 1.59 | 17.96 | 17.34 | 11.82 | 13.28 | 268.0 | 99.4 | 19.9 | b | N |
| 12 | 55 | 1.45 | 1.56 | 17.98 | 17.43 | 15.14 | 16.53 | 160.7 | 35.7 | 7.1 | b | Y |
| 13 | 55 | 1.53 | 1.60 | 17.97 | 17.92 | 11.56 | 13.17 | 264.5 | 96.8 | 19.4 | b | N |
| 14 | 55 | 1.53 | 1.60 | 18.19 | 17.99 | 14.62 | 16.35 | 200.2 | 55.5 | 11.1 | tb | Y |

Fig. 47 and Fig. 48 illustrate the relation of n at failure and the dry density for soils compacted at two different water contents. Fig. 47 contains the densities before the experiment. Inside the centrifuge during flight they increase, as illustrated in Fig. 48, where soil with higher water content is more prone to compaction. The green points of Fig. 48 are estimated, since an analysis of the exact compaction with GeoPIV was not possible due to missing point markers during the first experiments. All experiments which led to a failure of the model slope are included, except number 10 as it resulted in unrealistic values due to an incorrect testing procedure. The functions with the blue and green dots include the values of the experiments with an initial water content of about 11.55 %. The functions with the red dots include the values of w-initial = 18 %.

Generally, a higher stability at lower water contents and higher dry densities can be observed. The n-factor is proportional to the height until the slope is stable. The functions of the dryer soils show excellent $R^2$ of 0.98 and 0.95.

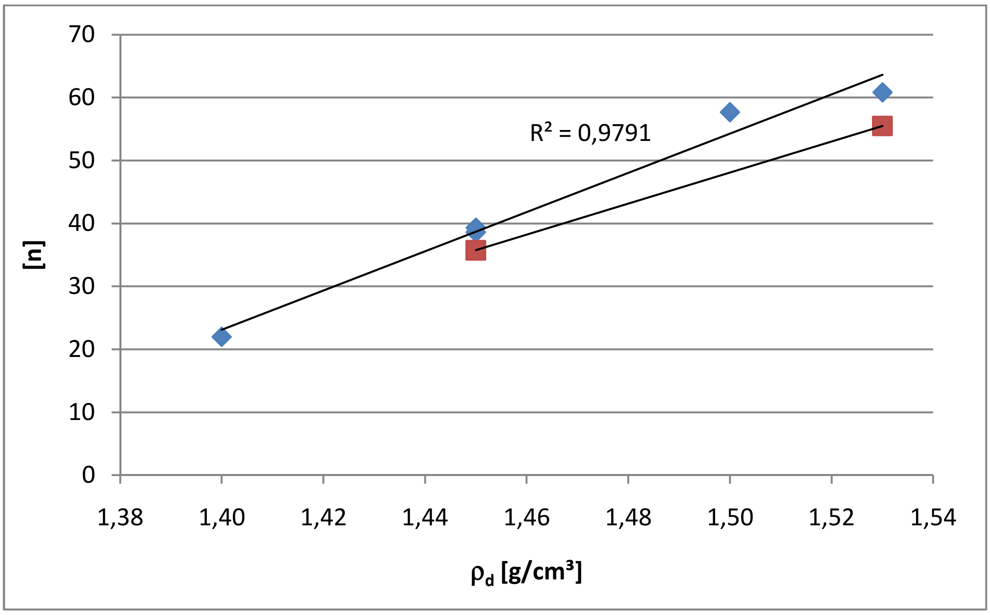


**Fig. 47: Density and n at failure; 2 different initial water contents; initial densities**

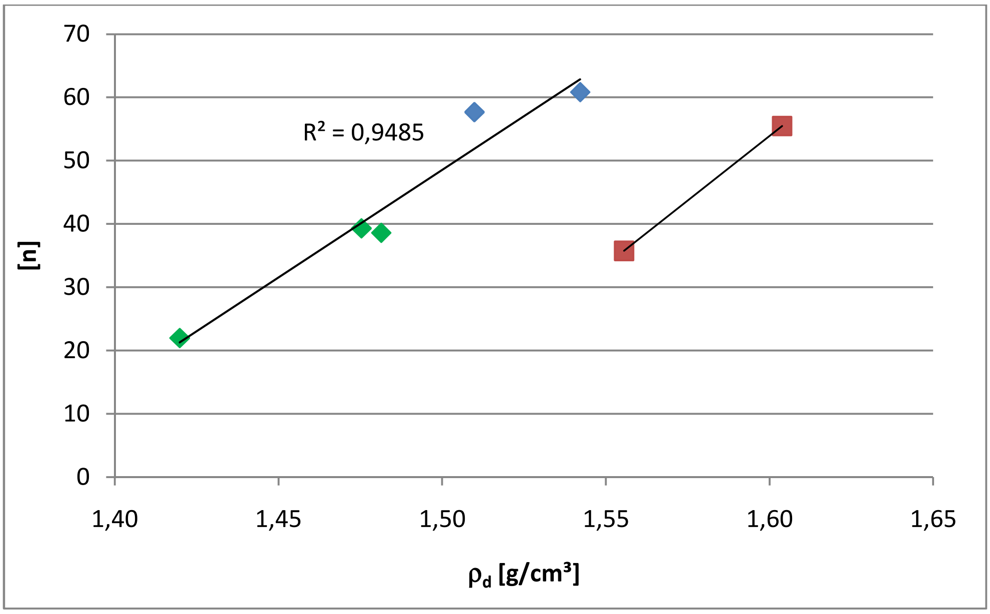


**Fig. 48: Density and n at failure; 2 different initial water contents; densities after centrifuge**

## 4.2 Soil Density

A clear correlation between higher densities and higher slope stability can be observed, as one can see in the two figures of Chapter 4.1.

### 4.2.1 Changes in density over time of experiment

During the experiments, the soil gets compacted as a result of the high centrifugal forces. Fig. 49 and Fig. 50 show the mean surface settlements over time of experiment 12 and 14. Additionally, n over time is illustrated. The chosen time span reaches up to around one minute before failure, in order to eliminate most of the movement from the slope failure process.

During experiment 12, at 10, 20 and 30 n, pauses in increase of n were made in order to allow the soil to rest. Although settlement rates decrease significantly over the time of a pause, more time would be necessary for achieving an entire stop of the process. Both at experiment 12 and 14, considerable settlements start after around 4 n. This might result from the fact, that the soil was already compacted during the process of soil preparation. Hence a certain minimum stress is necessary for achieving significant settlements in the centrifuge.

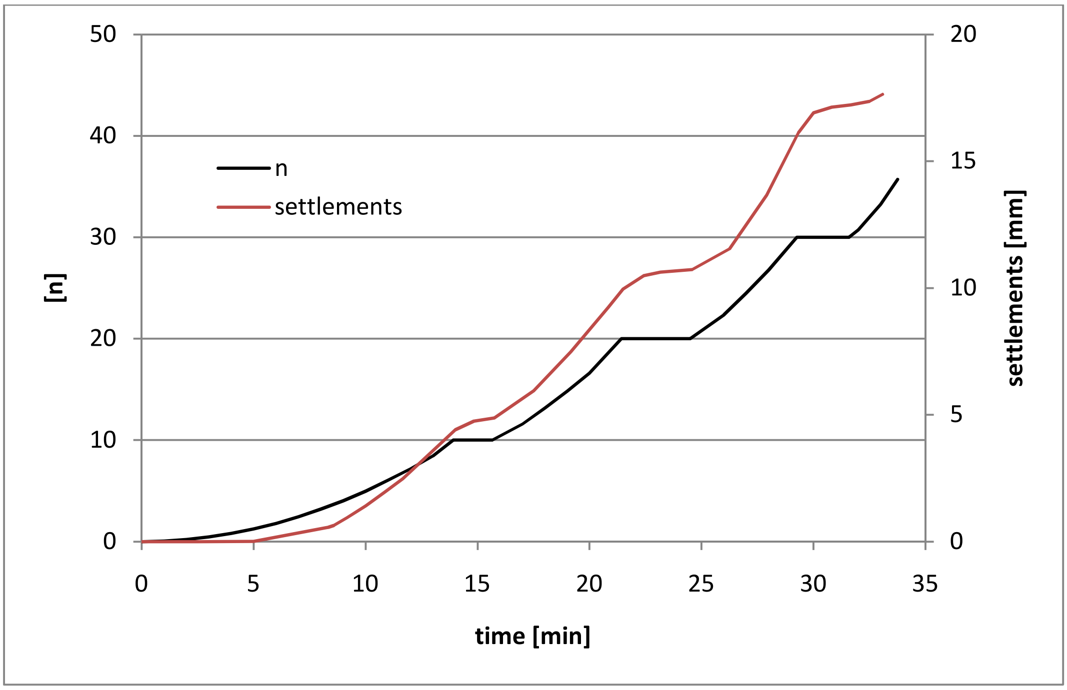


**Fig. 49: Settlements of experiment 12 over time**

At experiment 14, linear settlements over time can be observed after around 10 n. This is of special interest, as n rises in a non-linear way. A possible explanation of this phenomenon is the fact, that with increasing soil density, a stronger increase of the applied forces is needed for maintaining a constant rate of compaction. Further research would be necessary to explain the exactly linear correlation.

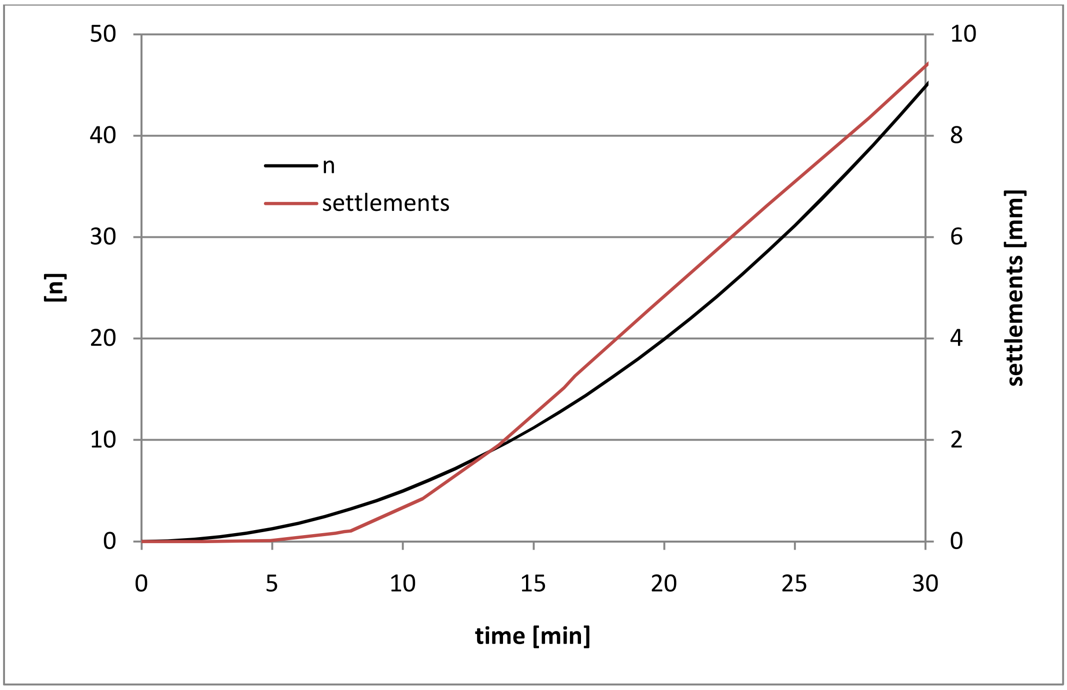


**Fig. 50: Settlements of experiment 14 over time**

In Table 13, results of penetrometer-tests and surface settlements as well as important corresponding data such as water content are presented.

**Table 13: Penetrometer results and max. settlements**

| Nr. | $\rho_d$ - initial | w [%] - initial | w [%] - after | w – diff. [%] | max. g-level [g] | ratio penetrometer [] | max. settlements [mm] |
|---|---|---|---|---|---|---|---|
| 06 | 1.50 | 11.22 | 10.91 | 2,76 | 57.7 | - | 1.64 |
| 07 | 1.53 | 11.30 | 10.76 | 4,78 | 60.8 | 1.06 | 1.98 |
| 08 | 1.45 | 11.10 | 10.47 | 5,68 | 100.9 | 1.45 | 10.09 |
| 09 | 1.53 | 17.36 | 11.90 | 31,45 | 99.4 | 3.88 | 8.18 |
| 10 | 1.45 | 17.05 | 14.15 | 17,01 | 49.2 | 2.34 | 13.19 |
| 11 | 1.53 | 17.34 | 11.82 | 31,83 | 99.4 | 4.02 | 8.97 |
| 12 | 1.45 | 17.43 | 15.14 | 13,14 | 35.7 | 1.47 | 16.97 |
| 13 | 1.53 | 17.92 | 11.56 | 35,49 | 96.8 | 5.58 | 10.53 |
| 14 | 1.53 | 17.99 | 14.62 | 18,73 | 55.5 | 1.93 | 11.51 |

The row 'w [%] – initial' contains the mean water content before the experiment, 'w [%] – after' the mean water content after the experiment and 'w – diff. [%]' is the difference of these two values in percent. The 'ratio penetrometer' expresses the proportion of the mean penetrometer-strikes before and after the centrifuge. The max. surface settlements are the results of the GeoPIV-analysis.

Row 2 to 6 contain values, which have an influence on the settlements. Row 7 and 8 illustrate the settlements and the change in density. The interaction of influencing and influenced values is complex. Hence each single influencing value will be described individually.

- A high initial dry density decreases the compressibility of the soil and leads to less settlements. For the penetrometer tests, heavier weights had to be used. But this does not influence the 'ratio penetrometer'.
- A higher max. g-level increases the settlements, as one can see in Fig. 49 and Fig. 50.
- The water content has a strong influence on the settlements and on the penetrometer results. Soils with an initial water content of around 11.55 % showed relative settlements between 0.7 % to 2.1 %. Soils with an initial water content of around 18 % range between 3.3 % and 6.8 %. Fig. 51 illustrates the relationship between 'ratio penetrometer' and 'w-difference'. A significant correlation exists between these two values, which both express a ratio between the initial and the final state of the soil. This comes from the fact, that the penetrometer enters the soil notably easier when the water content is higher. No such strong correlation was found for the 'ratio penetrometer' and the ratio of the dry density before and after the experiment.

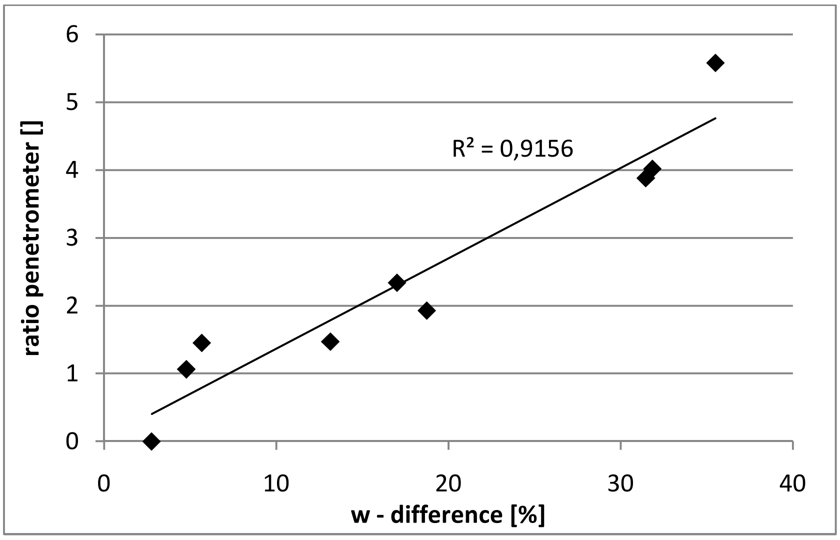

**Fig. 51: Correlation of penetrometer-ratio and change in water content**

### 4.2.2 Inhomogeneities in density

With the penetrometer tests, inhomogeneities in density could be found which occur due to the method of soil preparation. Fig. 52 shows the results of experiment 8. First, an increase in density can be observed after the experiment. Second, an inhomogeneity in the layer between 100 mm and 150 mm is revealed. Normally the number of strikes increases continuously until a maximum. Between 100 mm and 150 mm, however, the number of strikes is constant, which can be interpreted as an inhomogeneity as it starts to rise again in the layer below. The values of Fig. 52

are average values of two or three penetrometer tests. It has to be stated that significant differences in density could be found for tests performed at various profiles of the soil.

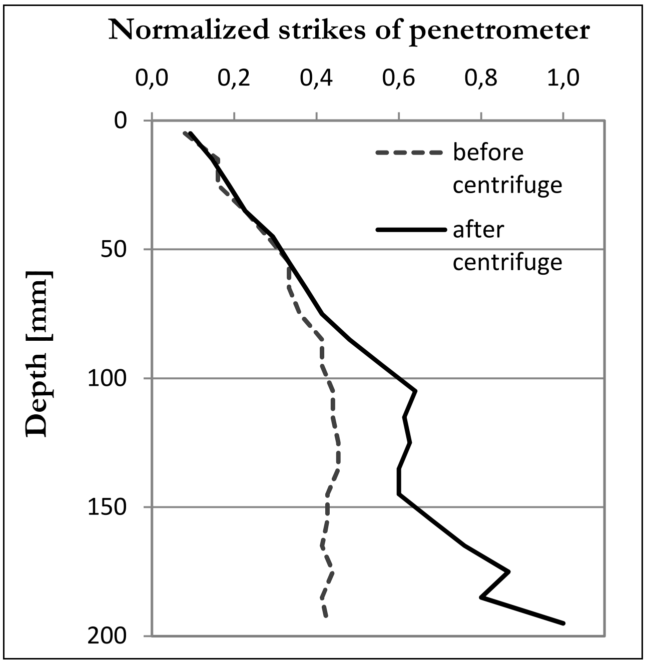

Fig. 52: Penetrometer results of experiment 8

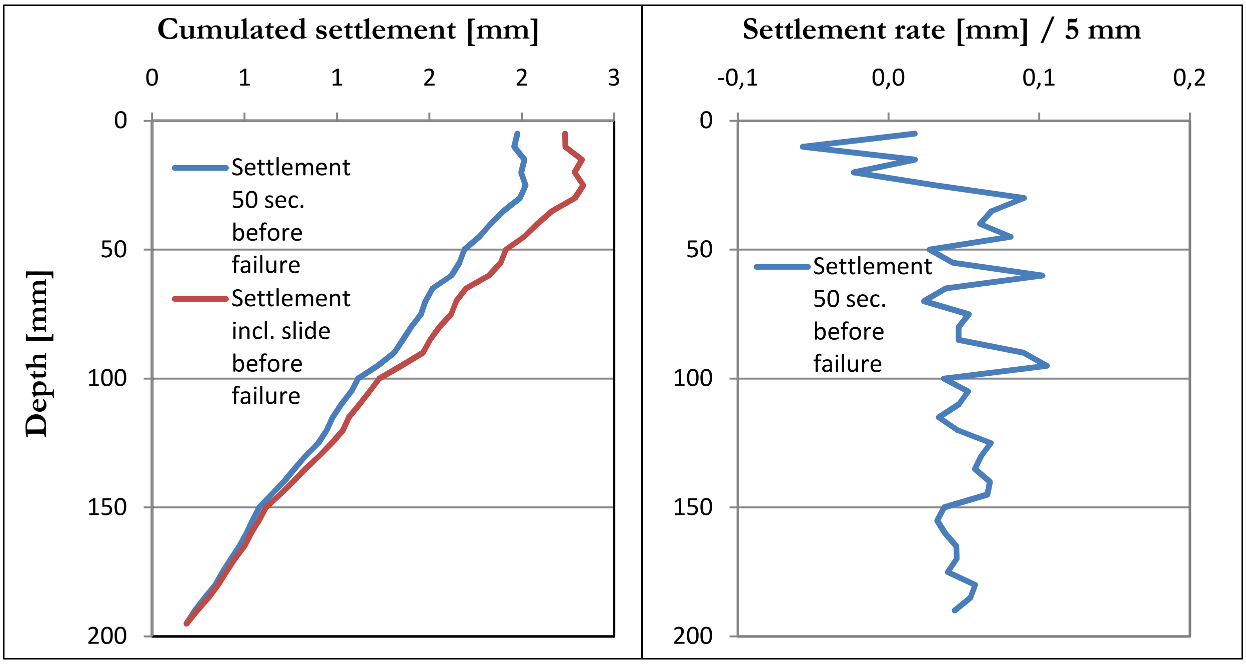

Fig. 53: Settlements of experiment 7

Fig. 53 illustrates the results of the GeoPIV-analysis of experiment 7. On the left hand side, the total settlements can be seen. One time 50 seconds before soil failure and one time directly before this event. In the upper half of the first layer, the total settlements do not increase notably. This can be interpreted as a result of the missing weight of the overlaying material. Under this zone, a constant settlement rate can be observed. On the right hand side, the settlements per 5 mm are shown. The difference within the layers is probably a result of the inhomogeneity of the soil at initial state after preparation. At this experiment, those inhomogeneities are negligibly small, but for instance at experiment 10 they are significant.

The total volumetric strain of experiment 8 is shown in Fig. 54. This is the only experiment, where the inclination of the slope was 45°. No failure of the soil model was observed, and so the max. g-level was 100.9, allowing the soil to compact without any pre-failure mechanism.

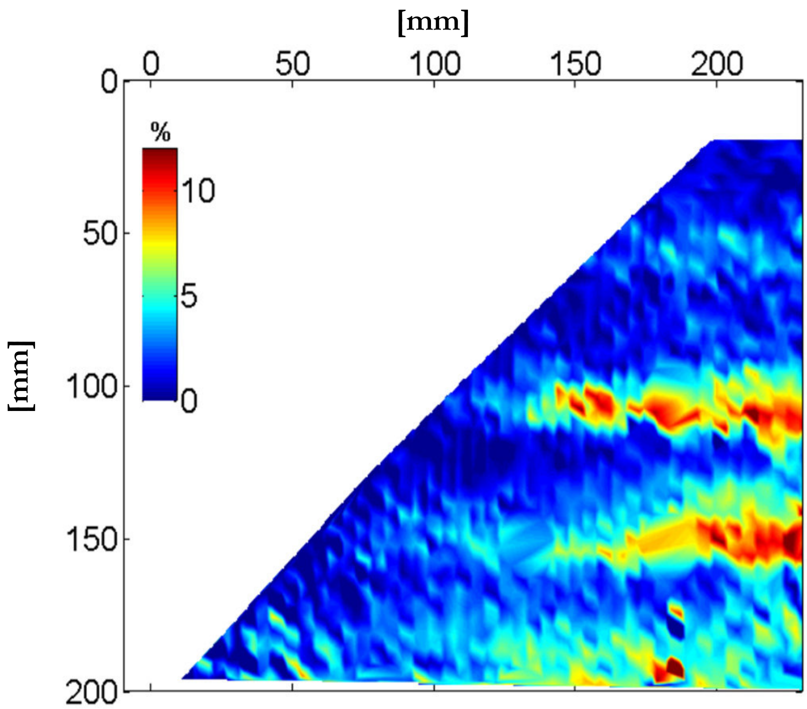


**Fig. 54: Total volumetric strain of experiment 8**

The inhomogeneities in density are revealed, as the parts which were initially less compacted, show larger volumetric strains.

## 4.3 Water content

The two figures of Chapter 4.1 reveal a clear connection between water content and slope stability. Higher water content results in lower stability. But it has to be taken into account, that for this soil, slopes with the higher initial water content of 18 % show an enhanced compressibility in comparison with soils of 11.55 % initial water content. This indirectly causes an increased stability due to a denser soil.

The soil water characteristics curve (Fig. 22) explains the relationship between suction and water content. A lower suction due to higher water content decreases the stability of the soil.

Of special interest is the loss of water during experiments as a result of an insufficient sealing system. This was not considered to be a problem for soils with 11.55 % initial water content. For soils with 18 % initial water content it had great influence.

- Experiment 9 was the first slope with higher water content. The problem of leakage was not known yet, and hence no sealing system was used. This resulted in a relative loss of water content of 31.45 %. First, the high initial water content facilitated the compaction of the soil, enhancing the stability. Second, the low final water content additionally increased the stability. No failure could be observed.
- For experiment 11, a basin was used for sealing. After the experiment, it turned out to have a hole. Thus the process was similar to experiment 9 in all aspects described above.
- During experiment 13, the sealing system did not work either, preventing failure as a consequence.
- Experiment 12 and 14 were considered to be representative for the high water content, as the sealing systems worked relatively well.

Fig. 55 illustrates the water content distribution of experiment 8. The target value of 11.55 % is approached in the lower layer, especially after the experiment. In the upper layer, the water content is less than 11.55 %, indicating a declining behavior over the height.
The decreased water content after the experiment shows the sparse loss of water even for the dryer soils. Samples from the front side of the slope generally have lower water content in comparison samples from the back side as no vertical screws were used for connecting the front wall to the ground plate.

In Fig. 56, the water content distributions of experiment 9 and 12 can be observed. Besides the same characteristics of experiment 8, experiment 9 shows the high loss of water due to the missing sealing system. At experiment 12, the effect of the sealing system can be seen.

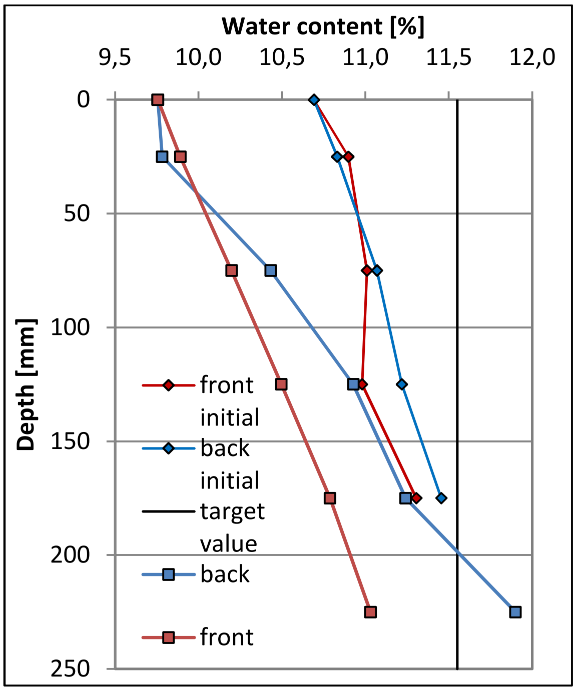

Fig. 55: Water content of experiment 8

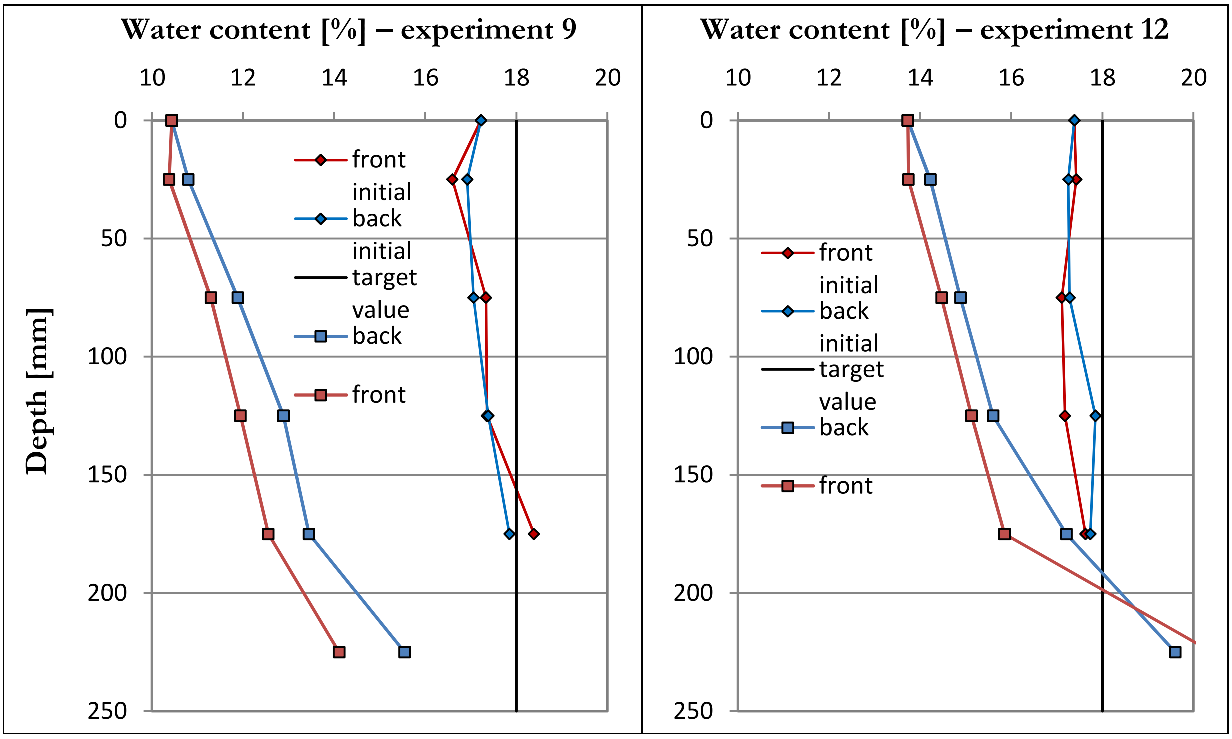

Fig. 56: Water contents of experiment 9 and 12

## 4.4 Slope angle

For all experiments, except for experiment 8, a slope angle of 55° was used. Experiment 8 was run with 45°. Fig. 54 shows, that no pre-failure deformations could be observed, although the slope model was accelerated up until 100.9 g. This finding led to a slope angle of 55° for all following experiments.

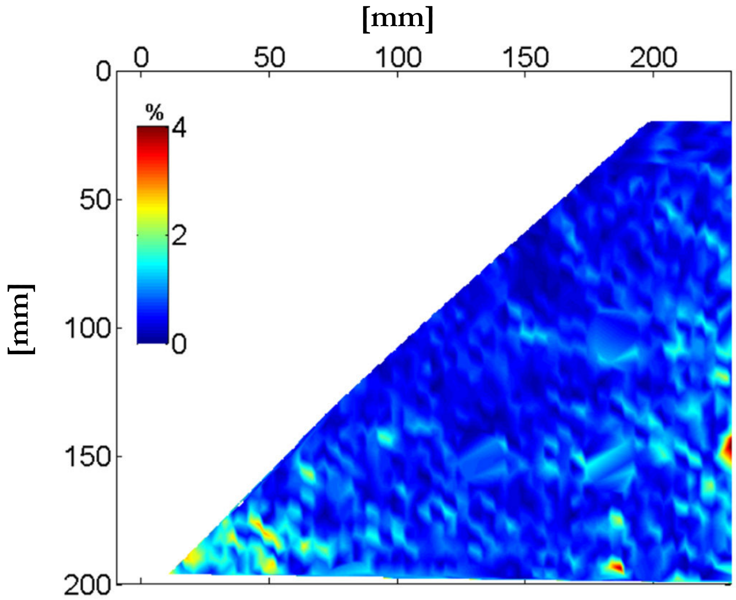

**Fig. 57: IMSS of last picture before determination of the test (experiment 8)**

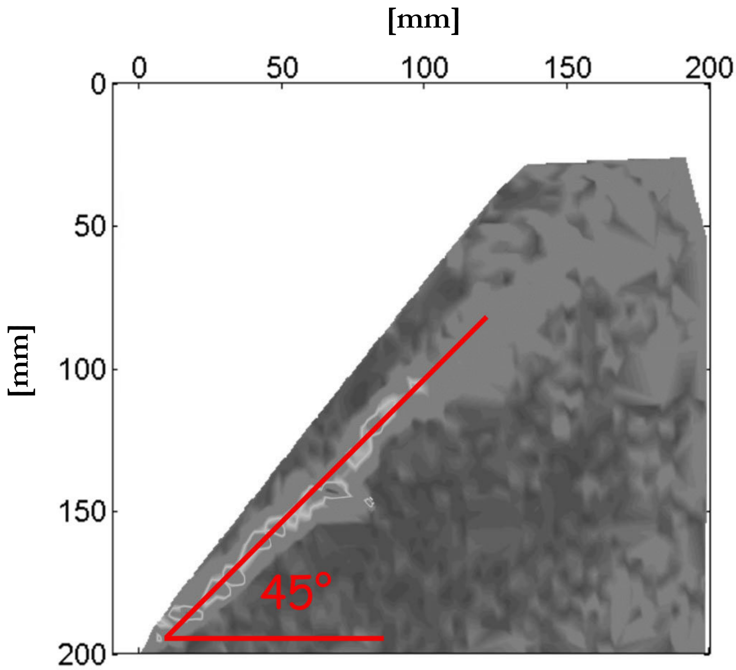

**Fig. 58: IMSS of last picture before failure of experiment 12; incl. 45° - line in red**

Fig. 58 illustrates the pre-failure deformations of experiment 12 a few seconds before actual failure. The red line shows that the shear band has about an angle of 45°. This is in accordance with the fact, that at experiment 8 with an initial slope angle of 45°, no pre-failure deformations could be found. Further details on the observed inclination of the shear bands are discussed in Chapter 4.6.1.

## 4.5 Soil structure

The two different water contents during soil preparation led to a significant variation in soil structure, as already described in Chapter 3.2.2. The initial density has additional influence. The denser, the more homogeneous the soil tends to be.

**Experiment 8**
$w = 11.10\ \%$, $\rho_d = 1.45\ g/cm^3$

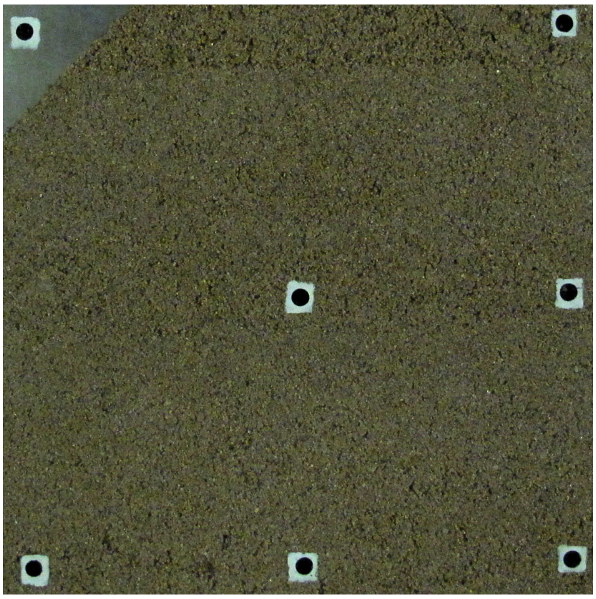

**Experiment 7**
$w = 11.30\ \%$, $\rho_d = 1.53\ g/cm^3$

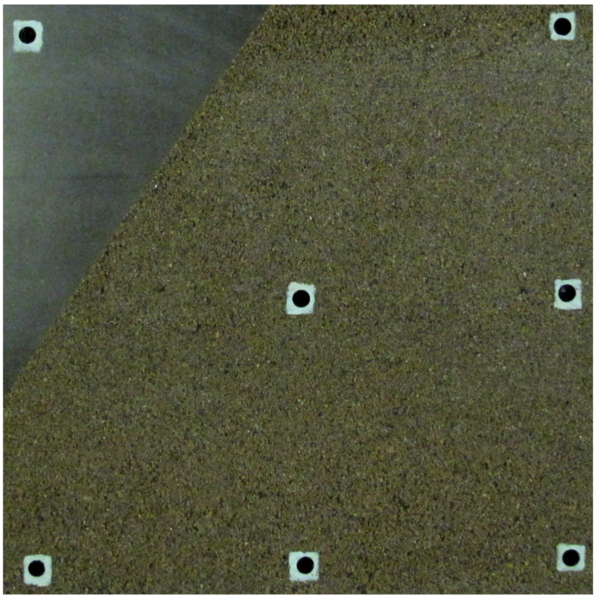

**Experiment 12**
$w = 17.43\ \%$, $\rho_d = 1.45\ g/cm^3$

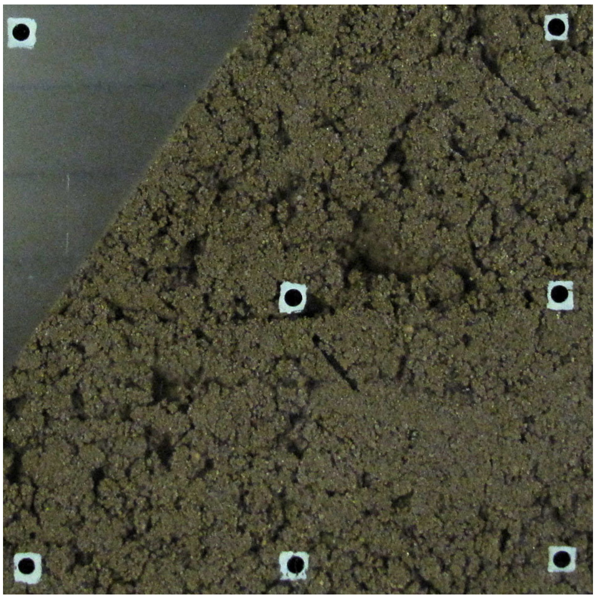

**Experiment 14**
$w = 17.99\ \%$, $\rho_d = 1.53\ g/cm^3$

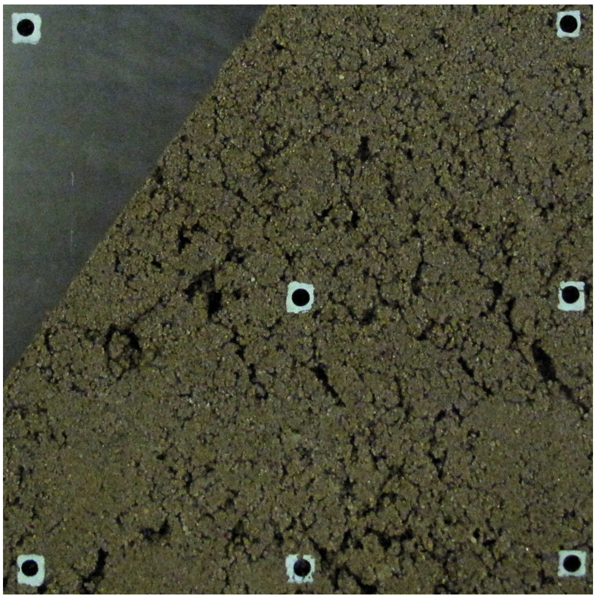

**Fig. 59: Soil structures**

In Fig. 59, sections of soils with different water content and dry density are illustrated. While both dryer soils can be considered homogenous regarding their structure, the wetter ones must be regarded inhomogenous. The soil of experiment 12 has a significant amount of macro pores.

Also the soil of experiment 14, but the pores are already smaller due to the stronger initial compaction. This process goes on during the experiment in the centrifuge.

Fig. 60 shows a time-series of experiment 12. During the experiment, the structure changed notably as a result of the process of compaction. For instance the macro pore marked by the red circles collapsed progressively.

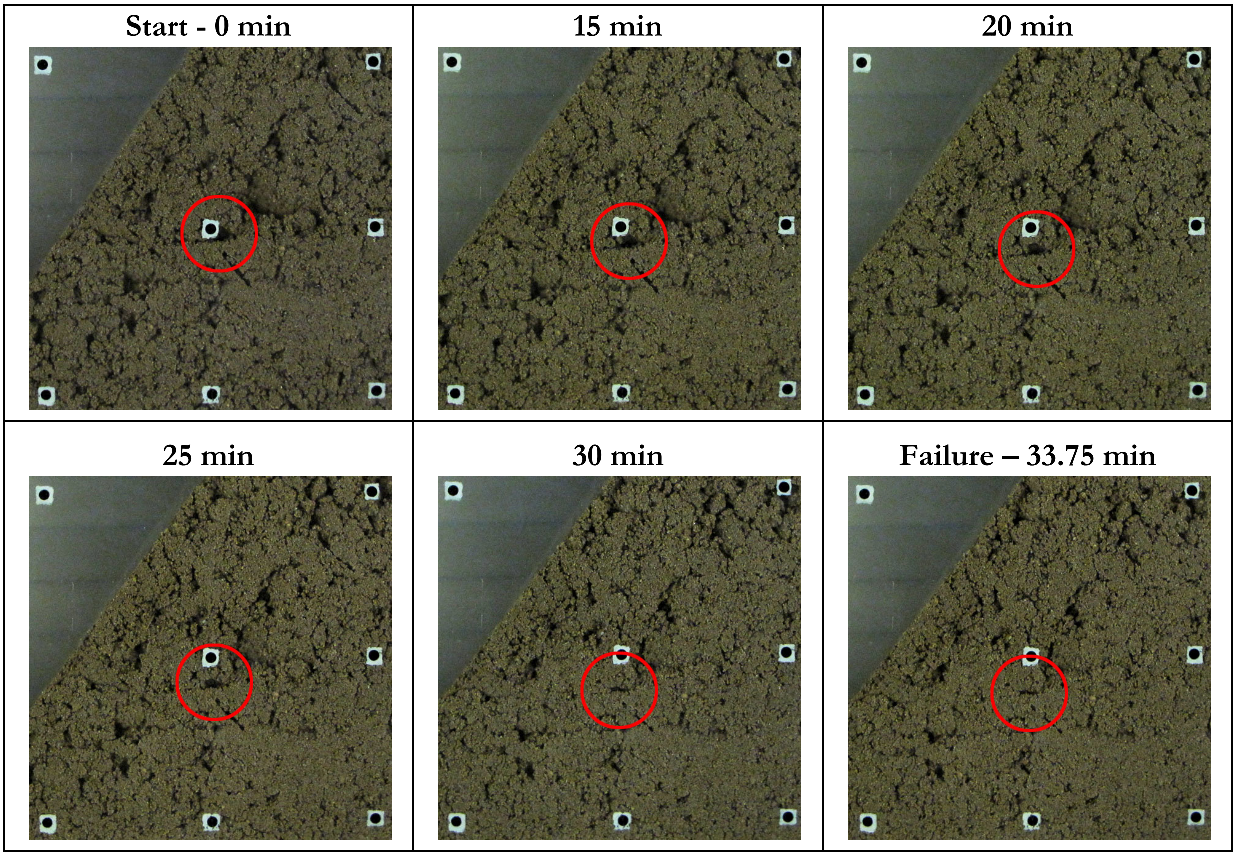


**Fig. 60: Time series of experiment 12**

Taking into account the findings above, soils with different initial water content are not fully comparable. Other soil preparation methods would be necessary for receiving soils of equal structure.

## 4.6 Shape and characteristics of (pre-) failure mechanism

Experiment 6 to 14 were analyzed with GeoPIV-code. This allowed to calculate and plot various types of strains and vector-graphics, enabling an interpretation of the shape of the shear bands. The failure process itself was documented during experiment 5 with a high speed camera. Due to the lower quality, a GeoPIV-analysis of those pictures did not lead to good results in consequence of the course mesh and the big proportion of wild vectors.

### 4.6.1 Shape of shear bands

In Fig. 62 the borders and the centre-lines of different shear bands are illustrated. They are based on shear band-illustrations such as the ones of Fig. 68. All experiments of Fig. 62 led to failure except number 9, although clear pre-failure deformations were already visible. The angle of the shear bands ranges around 45° (Fig. 63), where the wetter soils tend to show slightly lower angles. The length of the shear bands is strongly influenced by the time the photo was taken. It can range in between zero to five seconds before failure, as one picture was taken every five seconds. The lowest point of the shear bands is not necessarily at the toe of the slope. This is just the case at experiment 7 and 12. Experiment 6 and 10 show a similar behavior, but the lowest point of the shear band is slightly above the toe of the slope. Experiment 9 never failed, but the shear band of the pre-deformations leaves the slope about 50 mm above the toe of the slope. This is in accordance with the settlements (Fig. 64). In the layer between 150 mm and 200 mm they decrease significantly, probably resulting from a higher compaction during the soil preparation, which led to a higher stability in this layer, preventing the formation of a shear band. The shear band of experiment 14 has its lowest point also about 50 mm above the toe of the slope. The form of the mobilized soil mass, limited by the shear band, can be approximated as a triangle, both for dryer and wetter soils and gets steeper at the end (Fig. 61). An additional crack is visible in Fig. 61, similar to the cracks which can be observed at the high-speed photos of experiment 5.

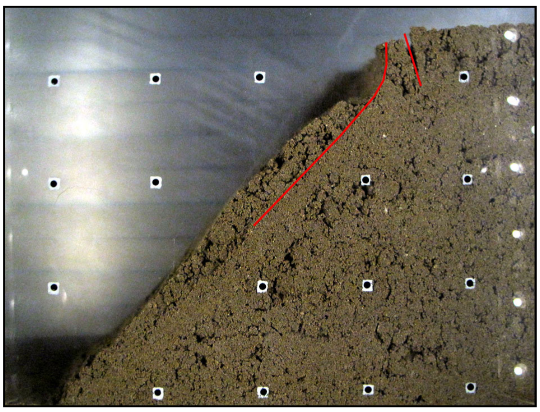

**Fig. 61: Experiment 12 - shape of slide**

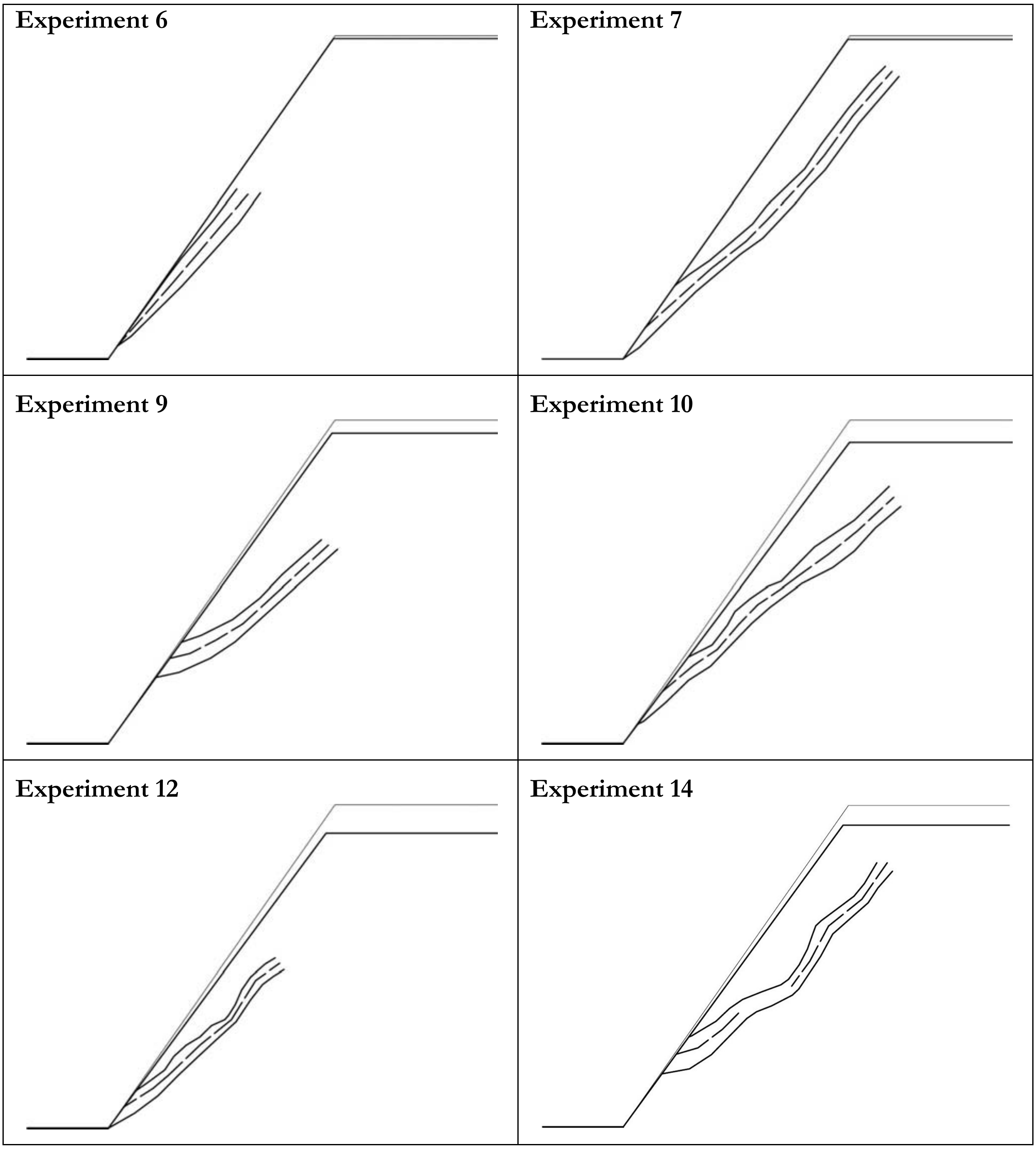


**Fig. 62: Shapes of shear bands – slope before compaction in thinner lines**

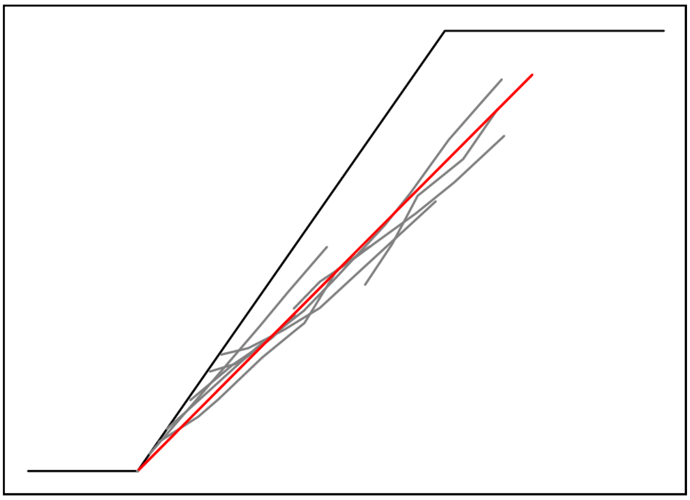

Fig. 63: Shear bands in grey and 45° angle in red

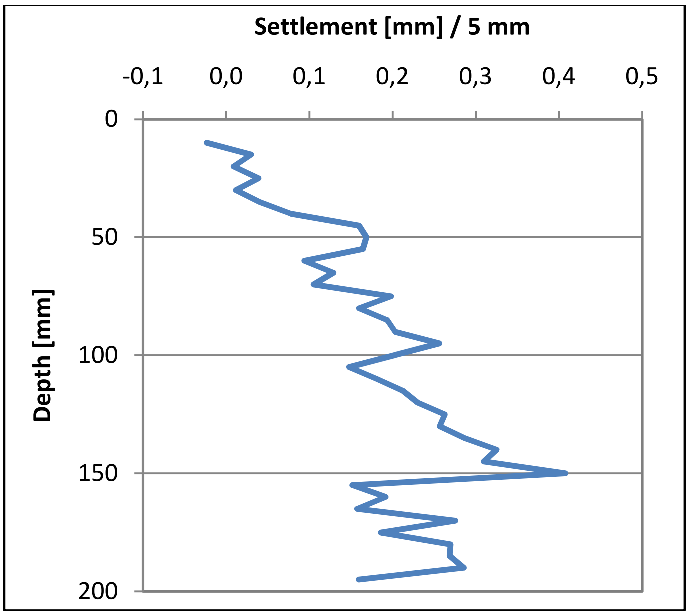


Fig. 64: Settlements of experiment 9

### 4.6.2 Vector-graphics

The movement of the patches analyzed with GeoPIV-code can be illustrated with a vector graphic. As an example, the vector-fields of Experiment 12 will be discussed.

The total vectors of the experiment (Fig. 65) contain both the settlements as well as the movements directly before failure. The vectors in the upper part generally have higher values as they also include the settlement of lower parts of the slope. The beginning movement of the slide can be observed, as the orientation of the vectors near the surface approximate the slope angle, where the vectors located more inside the soil are of smaller value and tend to approach the vertical alignment.

Clearly notable movement of the soil exists during pre-failure state (Fig. 66). The left and the right picture differ 20 seconds from each other, where on the right picture the high increase of the vector-values directly before failure is visible.

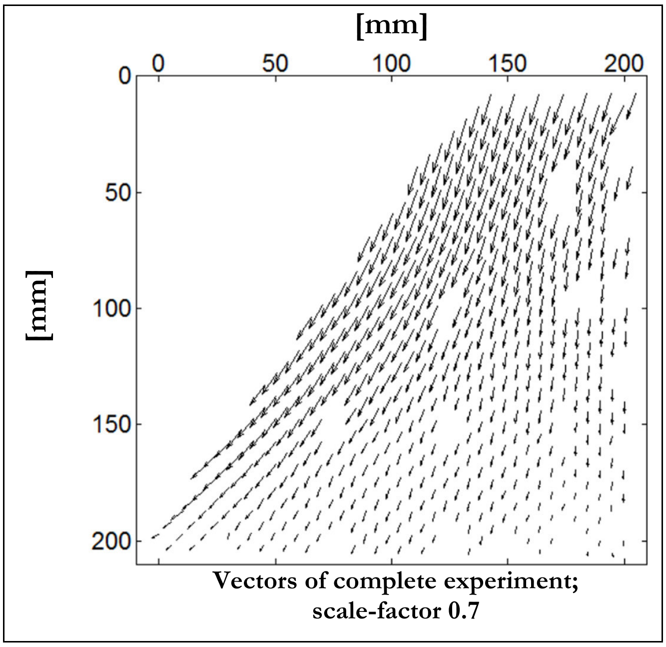


**Fig. 65: Total vectors of experiment 12**

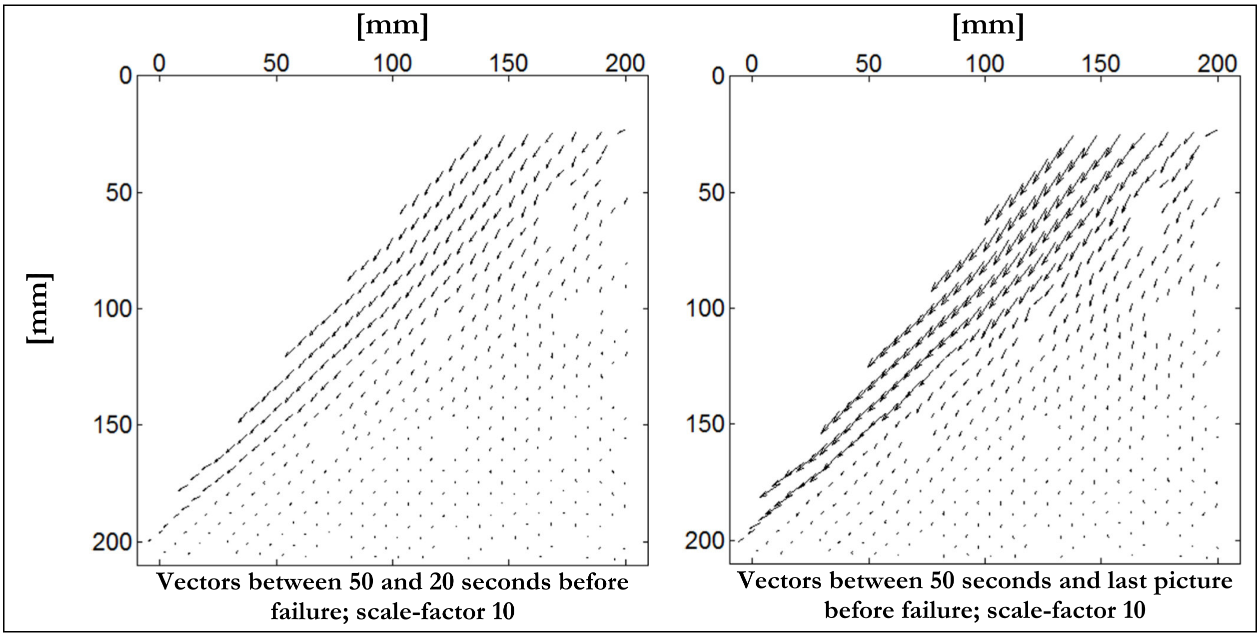


**Fig. 66: Vectors of experiment 12 - shortly before failure**

### 4.6.3 Begin of failure mechanism

The progressive nature of the failure mechanism can be made visible by plotting a time-series of the total maximum shear strains before failure (Fig. 67 and Fig. 68).

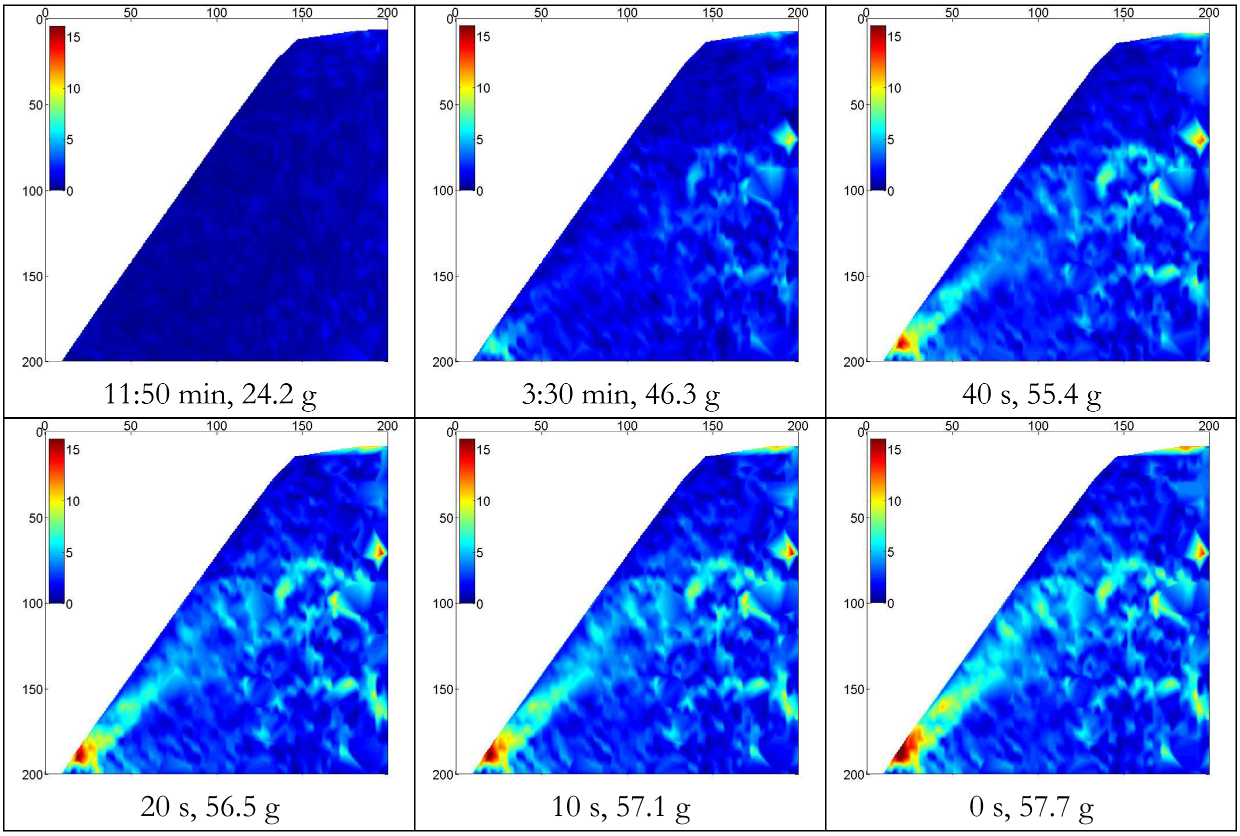


**Fig. 67: Total maximum shear strain - experiment 6, with time before failure and g-level**

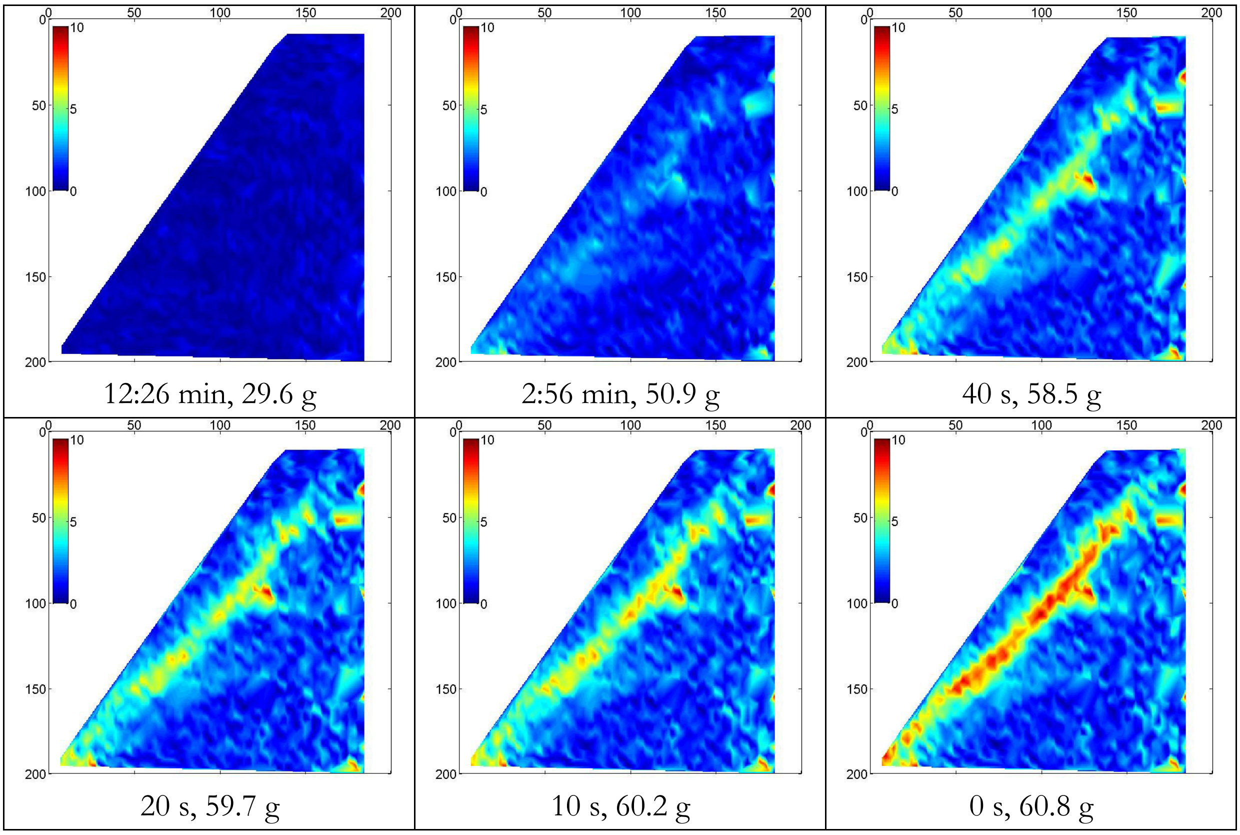


**Fig. 68: Total maximum shear strain - experiment 7, with time before failure and g-level**

At experiment 6, the failure mechanism was observed to initiate at the toe of the slope. Experiment 7 reveals a different behavior. The shear band is already identifiable over the whole length at an early stage.

### 4.6.4 Process of failure

The photo series of experiment 5 during failure (Fig. 69) consist of images from the high speed camera with a time difference of 1/60 s. The whole process of failure took around 1/6 s.

First signs of failure are visually recognized at the top of the slope. Probably, at this point the mobilized soil mass gets ripped away from the non-moving soil and subsequently the whole slide starts to move.

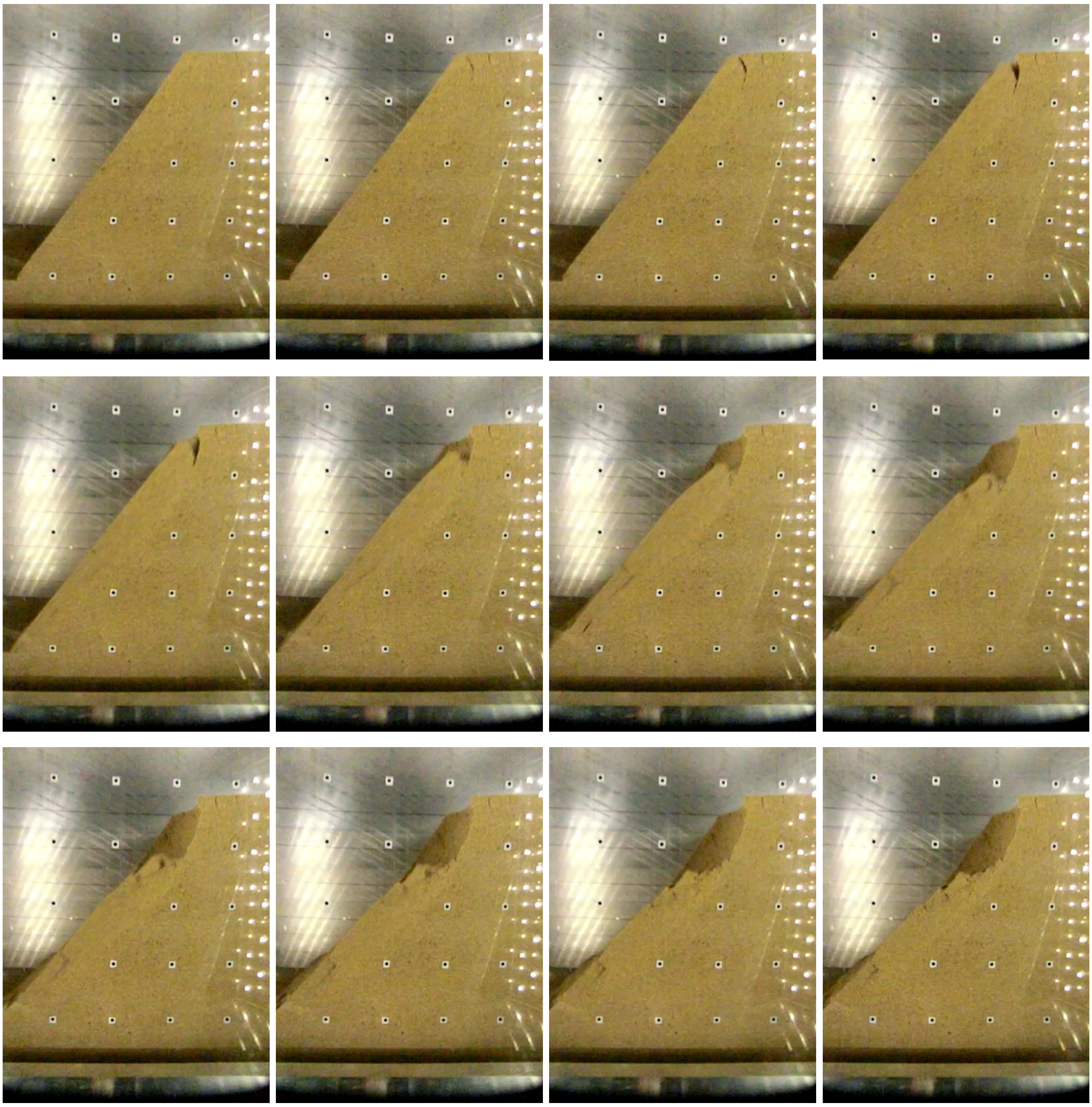

**Fig. 69: Failure at experiment 5**

It can be observed, that three cracks exist at the crest. The one nearest to the slope becomes part of the shear band. The slide itself does not consist of one undisturbed block. In the lower third, it is torn apart.

During the failure process, the moving part of the slope is blurry. A more powerful high-speed camera and a brighter light would be necessary to reduce the shutter time and get sharp images as a consequence.

### 4.6.5 Shape after failure

Fig. 70 illustrates the shape of the deposited soil mass as well as the stable part. The thinner line shows the slope directly before failure. The external borders of the mobilized mass could be reconstructed with the photos. The internal boundaries are estimations, as they are not precisely detectable by using the pictures. It can be observed, that slightly longer run-outs exist at experiments with dryer soils (Experiment 6 and Experiment 7). The average angle of those two failed slope ranges around 45°. The experiments with wetter soil (12 and 14) show shorter run-outs and an average angle of about 48°. Experiment 6 and 7 formed a second crack at the top of the slope which did not fail. At experiment 12, such a crack also exists and is even wider.

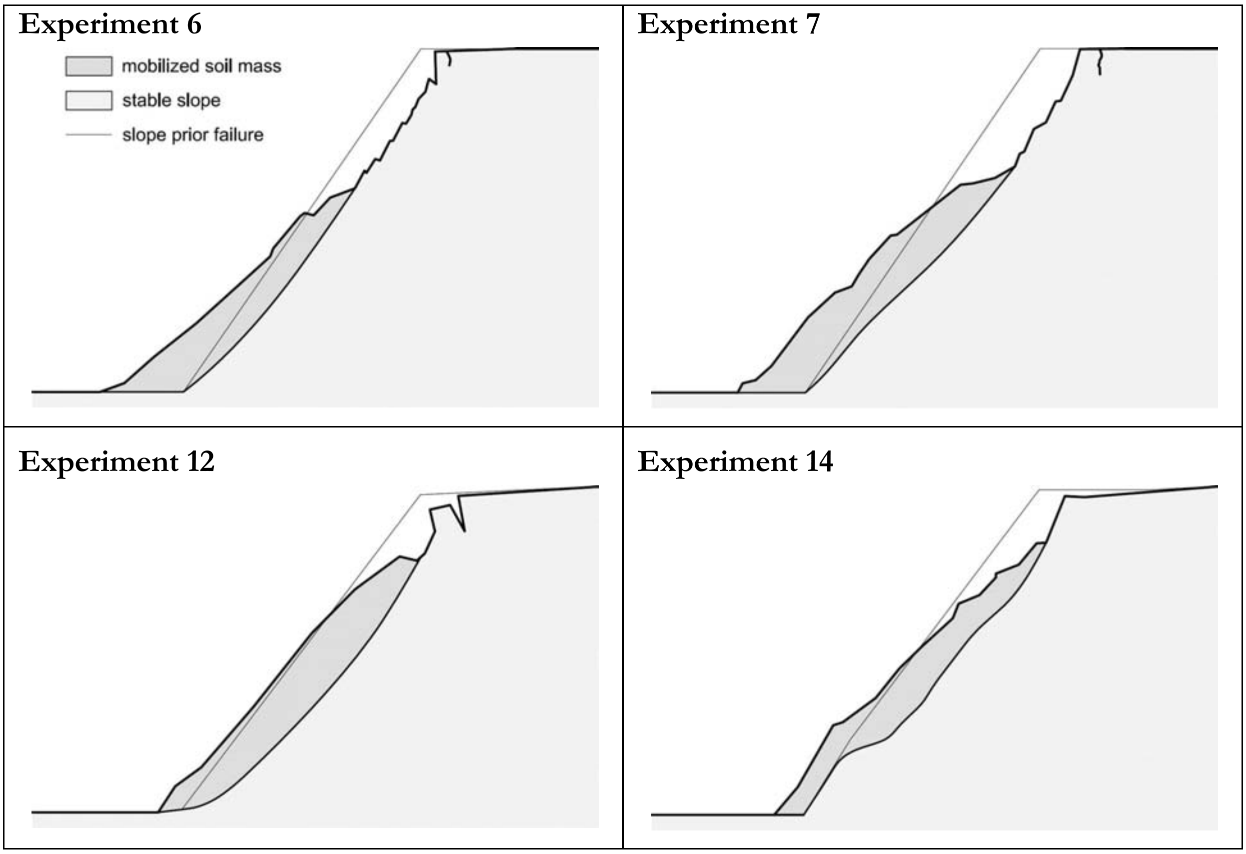


**Fig. 70: Shape of failed slopes**

### 4.6.6 Horizontal and vertical deformations

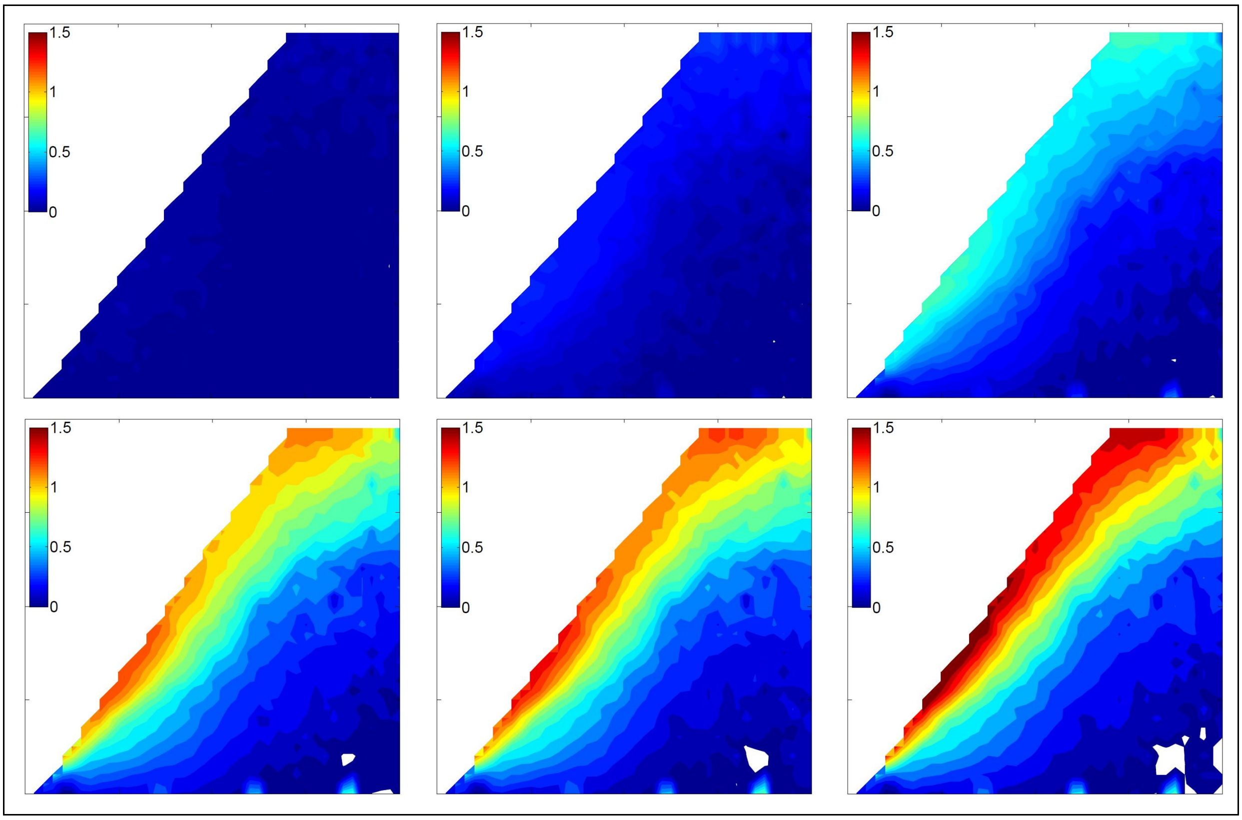


Fig. 71: Progressive horizontal deformations - Exp. 6

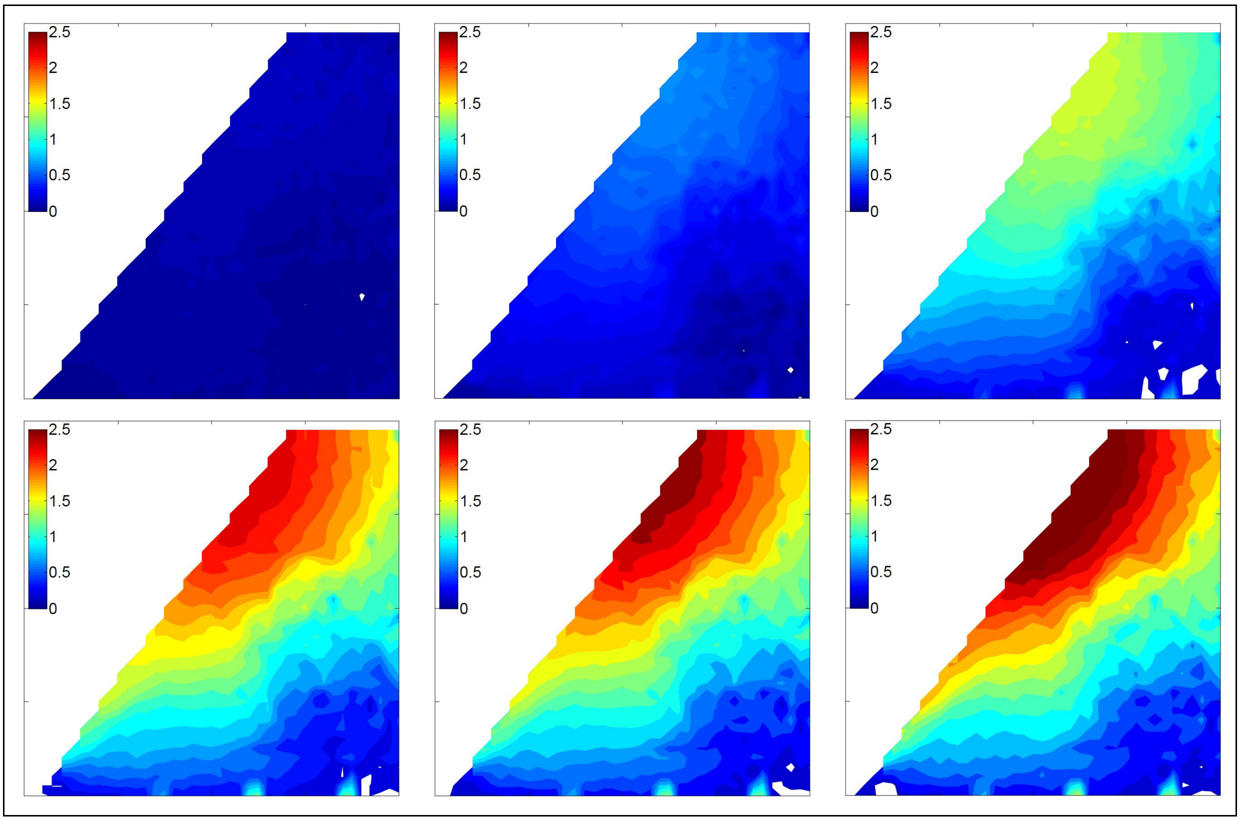


Fig. 72: Progressive vertical deformations - Exp. 6

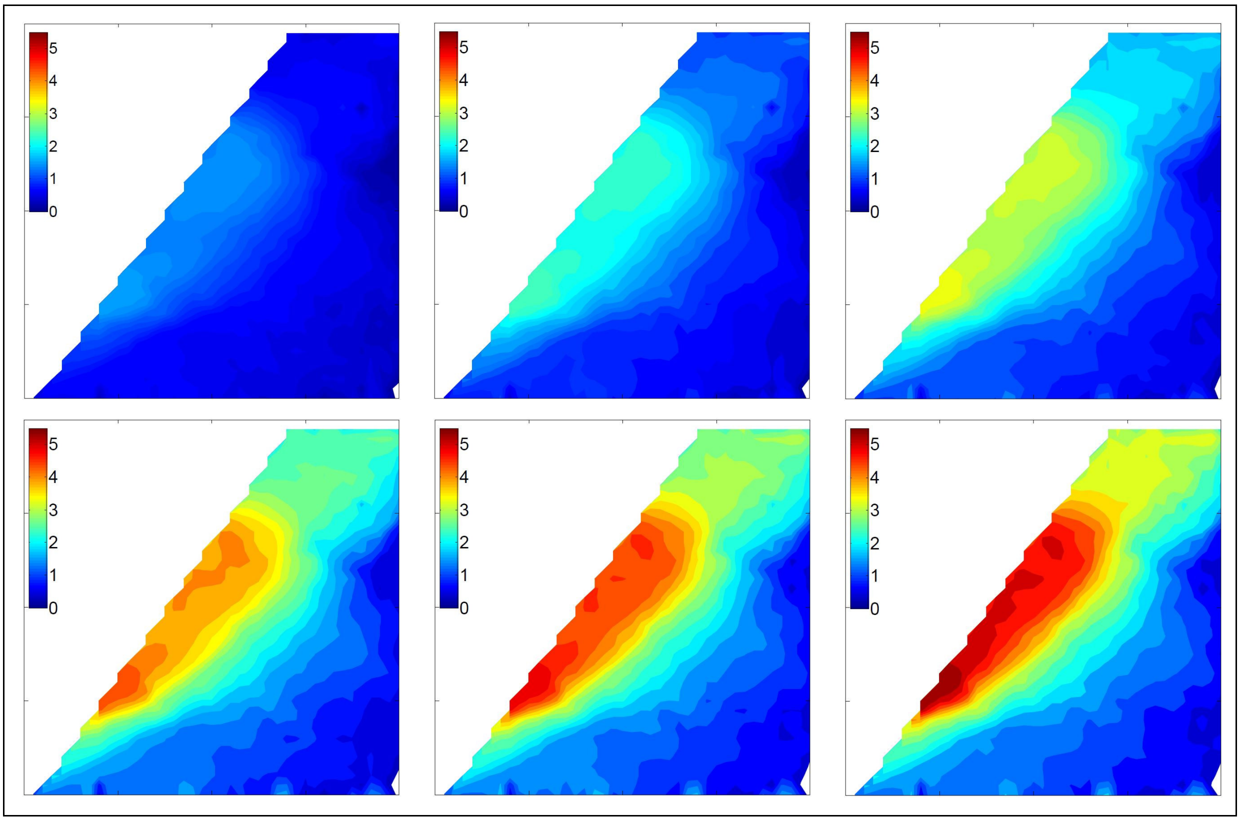


Fig. 73: Progressive horizontal deformations - Exp. 14

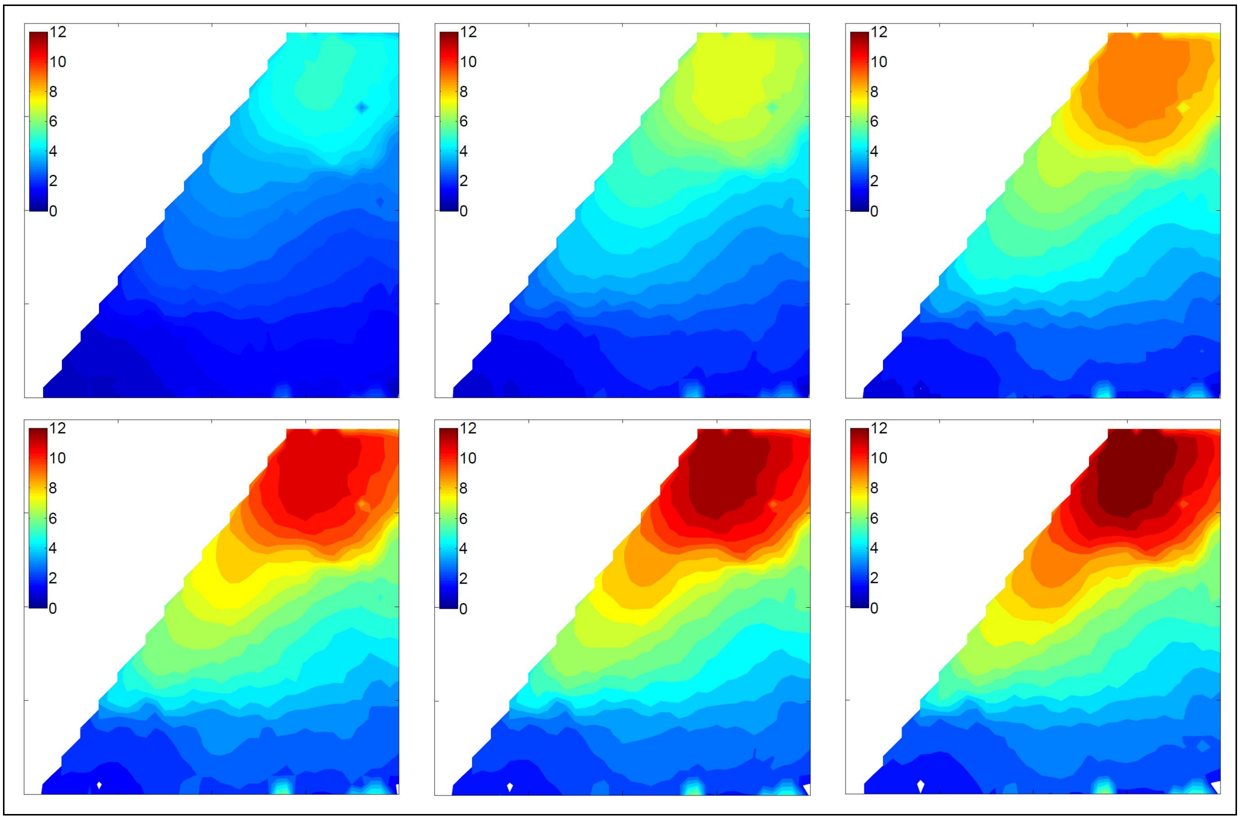


Fig. 74: Progressive vertical deformations - Exp. 14

Fig. 71, Fig. 72, Fig. 73 and Fig. 74 illustrate the differences in vertical and horizontal pre-failure deformations where experiment 6 is one with dryer soil and experiment 14 with wetter. A different scaling was chosen for vertical and horizontal values, coming from the respective maximum. The vertical deformations mainly result from the settlements, where the horizontal ones mostly come from the slide.

In Fig. 73 it can be observed, that the shear band leaves the slope between layer three and four. This probably results from inhomogeneities within the soil. Experiment 6 shows a shallower slide than experiment 14, which is more profound. At experiment 14, the top of the slope reveals relatively small horizontal deformations.

### 4.6.7 Slopes in three dimensional space

In engineering practice, the analyses of slope stability are usually based on plane strain assumptions. However, none slope is infinitely long or wide. Most slopes are three dimensional structures. During experiment 6 for instance, at the top only the front part of the slope failed. From there towards the toe of the slope the sliding mass becomes wider. This phenomenon probably results from the inhomogeneities in density caused by the method of soil preparation, which gave rise to density variations between the front and the back parts of the model slope.

# 5 Summary and Conclusion

In this thesis, some centrifuge tests with model slopes of partially saturated sandy material were conducted. The following parameters were varied:

- Density,
- Water content,
- Slope angle

Some technical problems were encountered during the tests, e.g. shut-down of the centrifuge due to unbalanced counterweights, breakdown of the lighting system and leakage of the model box.

- The problem concerning the unbalanced counterweights could be solved by distributing them as similar as possible to the weight of the model box.
- The lighting system was exposed to strong vibrations as a result of the unbalanced counterweights. Fixing the first problem could also mitigate the lighting problem. Additionally, smaller lighting panels with a stronger construction were used, which improved the resistance against vibrations.
- One of the several systems tested for preventing leakage could improve the model box significantly. It is recommended to use model boxes which are completely waterproof for future research on soils with a high degree of saturation, as the leakage of soil water leads to wrong results due to changing soil parameters and mechanical behavior.

The optimization and validation of the model slope preparation was another task of this research. The following conclusions and recommendations can be given:

- Compacting the soil in layers is a convenient method to obtain the desired density and water content. However, some care is needed in order to obtain homogenous model soil. Additionally, the thickness of the layers needs to be limited.
- Pre-compaction should be conducted in the middle of each layer, as the homogeneity in density increases that way.

The model preparation is validated by penetrometer tests and measurements of water content. Examining the water content was of high importance, as the leakage problem of the model box could be quantified in this way, and the water content at failure conditions could be estimated.

For data processing, the GeoPIV code from WHITE & TAKE (2002) as well as self-written scripts for Matlab were used. Matlab is capable of processing large amount of data in relatively short time. Moreover, Matlab allows user written codes to be included.

The main result of this research is the established relationship between soil density and the n-factor at slope failure. The tests showed excellent correlation with $R^2$ between 0.95 and 0.98. Further results are as follows:

- Lower slope stability at higher water contents could be observed.
- Failure occurred at slopes inclined at about 55° but not at 45°. For the model tests with the slope angle of 45° only vertical settlements were observed.
- The angle of the shear bands was around 45°. Wetter soils tend to give rise to slightly smaller angle of shear bands.
- Varying water content due to soil compaction leads to inhomogeneous soil structure, which makes it difficult to compare the tests.
- Usually slope failure begins at the toe of the slope but inhomogeneities can influence the point of initiation.
- The planar failure surface gives rise to a sliding body of triangular shape. The failure surface becomes steeper in the upper part of the slope.
- At some soil models, tension cracks could be found at the top of the slope.
- The slope after failure shows average angles of 45° for the dryer soils and 48° for the wetter soils, respectively.
- The time from failure initiation to deposition of the mobilized mass takes around 1/6 s at model scale.

These results and findings can be used for the validation of numerical models, which will eventually lead to better predictions of landslides in unsaturated soil.

# Appendix I

The protocols of some tests are provided in this appendix. Not all model slopes were included in the procedure of data processing as some formed part of optimization processes and hence did not lead to suitable results. The absence of point markers on the acrylic glass during the first experiments, shut-down of the centrifuge due to unbalanced counterweights, breakdown of the lighting system and leakage of the model box prevented a proper testing procedure at some experiments.

The abbreviations used are:

TMSS … Total maximum shear strain

TVS … Total volumetric strain

IMS … Incremental maximum shear strain

For each experiment, a picture of the soil after failure is attached and the most important data is summarized in a table. Different strains and vector-graphics from the PIV-analysis as well as diagrams for the water content distribution, the penetrometer tests and the cumulated and single settlements are presented.

# Experiment 6

**Table 14: Characteristics of the experiment**

| | |
|---|---|
| Inclination [deg] | 55 |
| Dry density $\rho_d$ [g/cm³] – before centrifuge | 1.50 |
| Dry density $\rho_d$ [g/cm³] – after centrifuge | 1.51 |
| Water content w [%]<br>- soil preparation<br>- before centrifuge (mean)<br>- after centrifuge (mean)<br>- after centrifuge (layer at toe) | <br>11.63<br>11.22<br>10.91<br>11.15 |
| Max. revolutions per minute [rpm] | 204.1 |
| Max. g-level [g] | 57.7 |
| Max. height [m] | 11.5 |
| Failure | Yes |

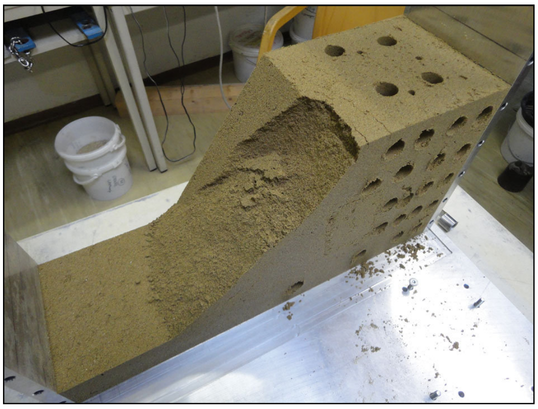

**Fig. 75: Soil after centrifuge**

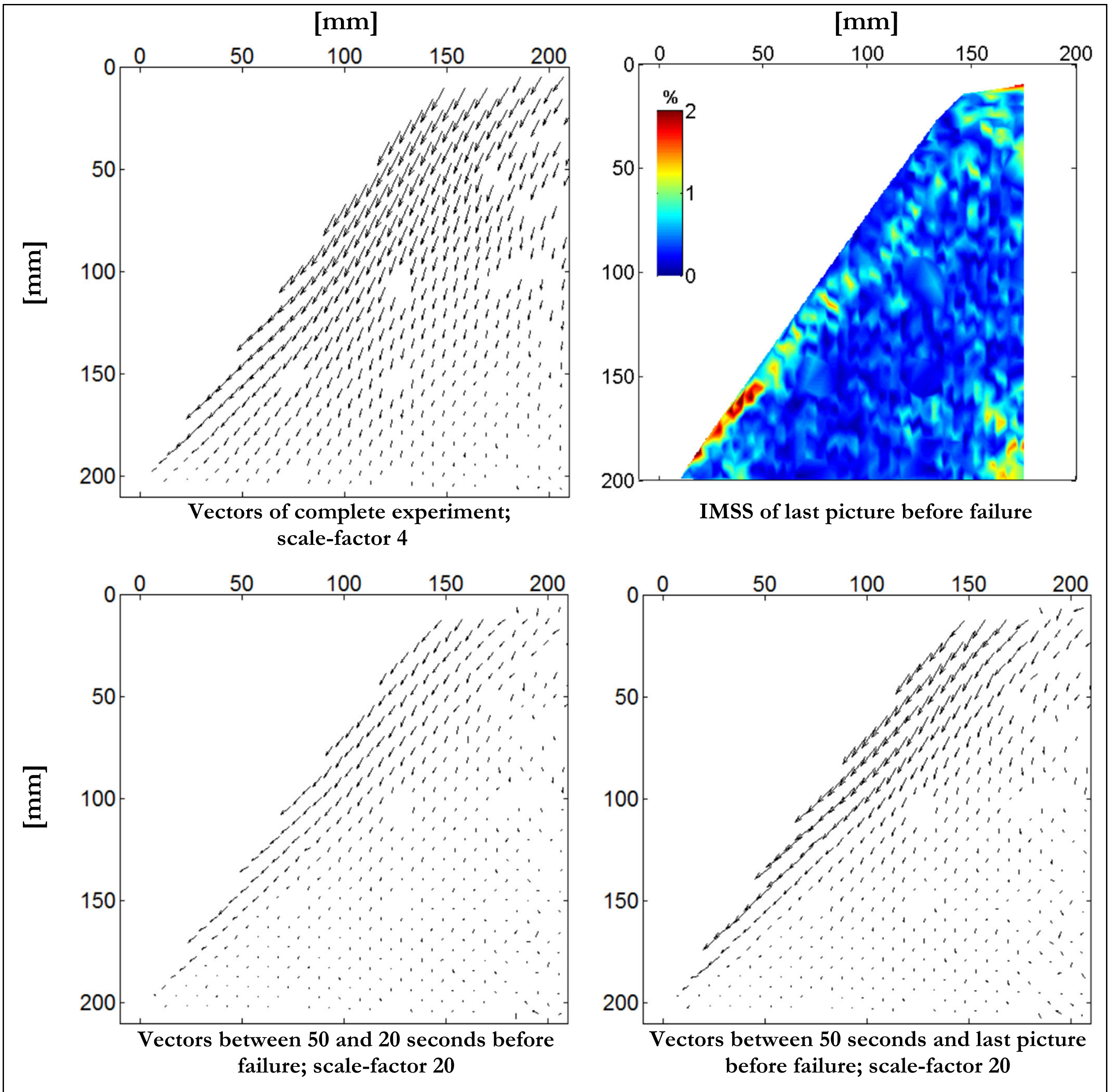


**Fig. 76: Results of PIV-analysis**

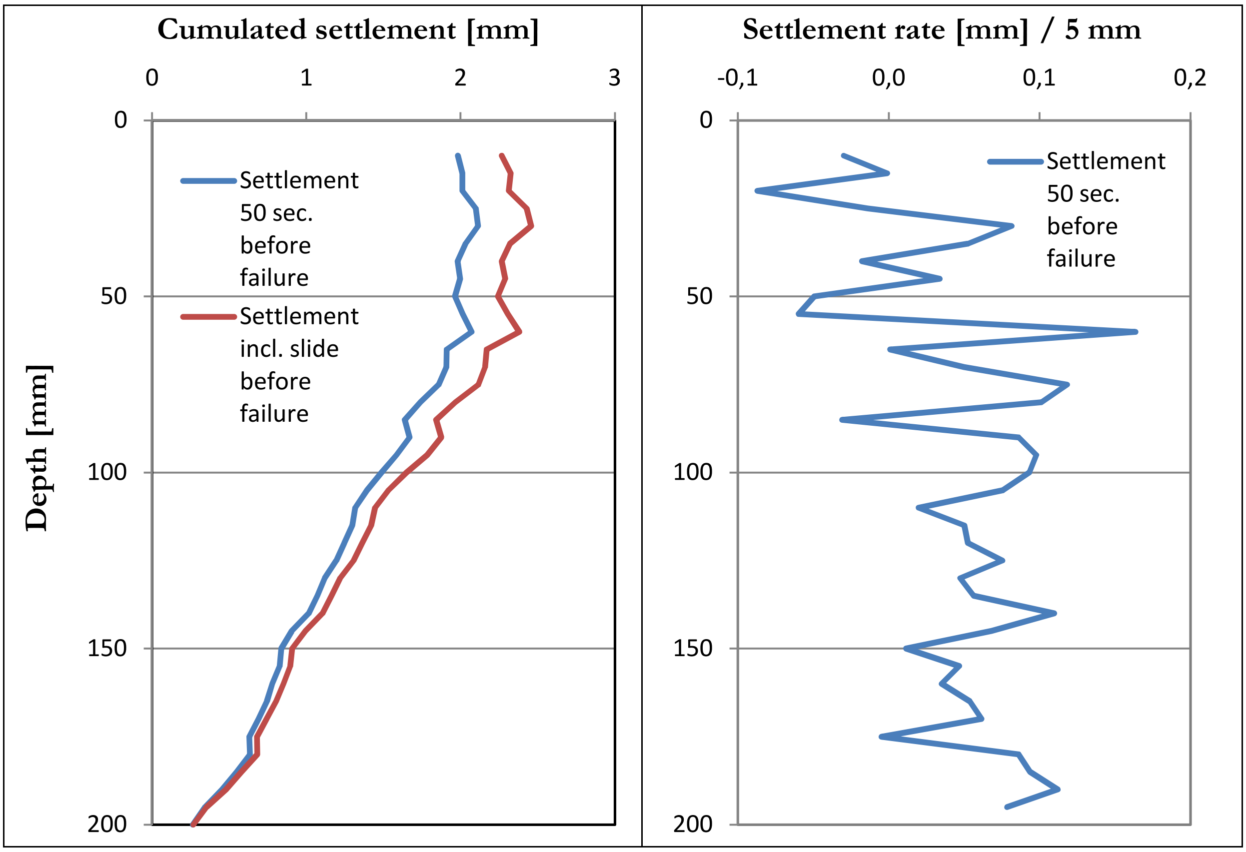


Fig. 77: Settlements of the soil in centrifuge

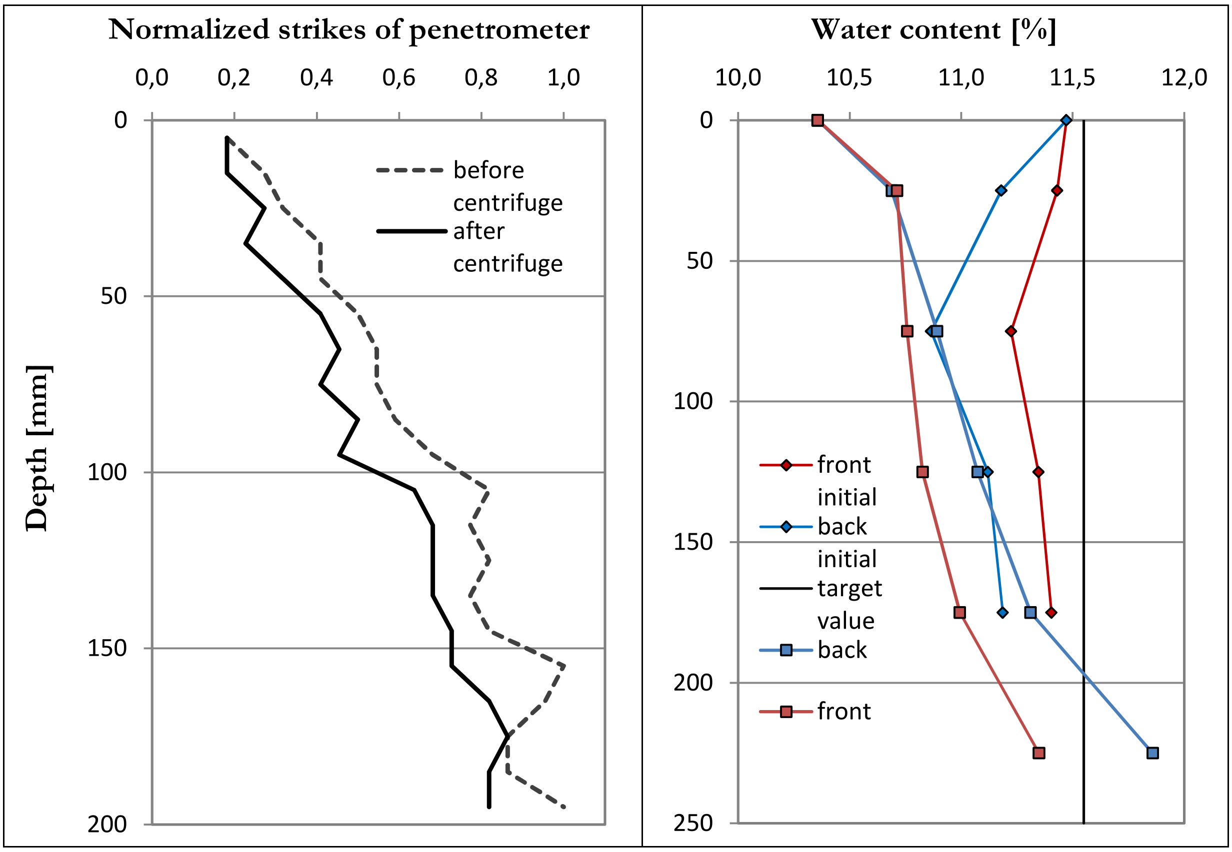


Fig. 78: Results of penetrometer-tests and measurements of water content

# Experiment 7

**Table 15: Characteristics of the experiment**

| | |
|---|---|
| Inclination [deg] | 55 |
| Dry density $\rho_d$ [g/cm³] – before centrifuge | 1.53 |
| Dry density $\rho_d$ [g/cm³] – after centrifuge | 1.54 |
| Water content w [%]<br>- soil preparation<br>- before centrifuge (mean)<br>- after centrifuge (mean)<br>- after centrifuge (layer at toe) | <br>11.66<br>11.30<br>10.76<br>11.15 |
| Max. revolutions per minute [rpm] | 209.6 |
| Max. g-level [g] | 60.8 |
| Max. height [m] | 12.2 |
| Failure | Yes |

**Fig. 79: Soil after centrifuge**

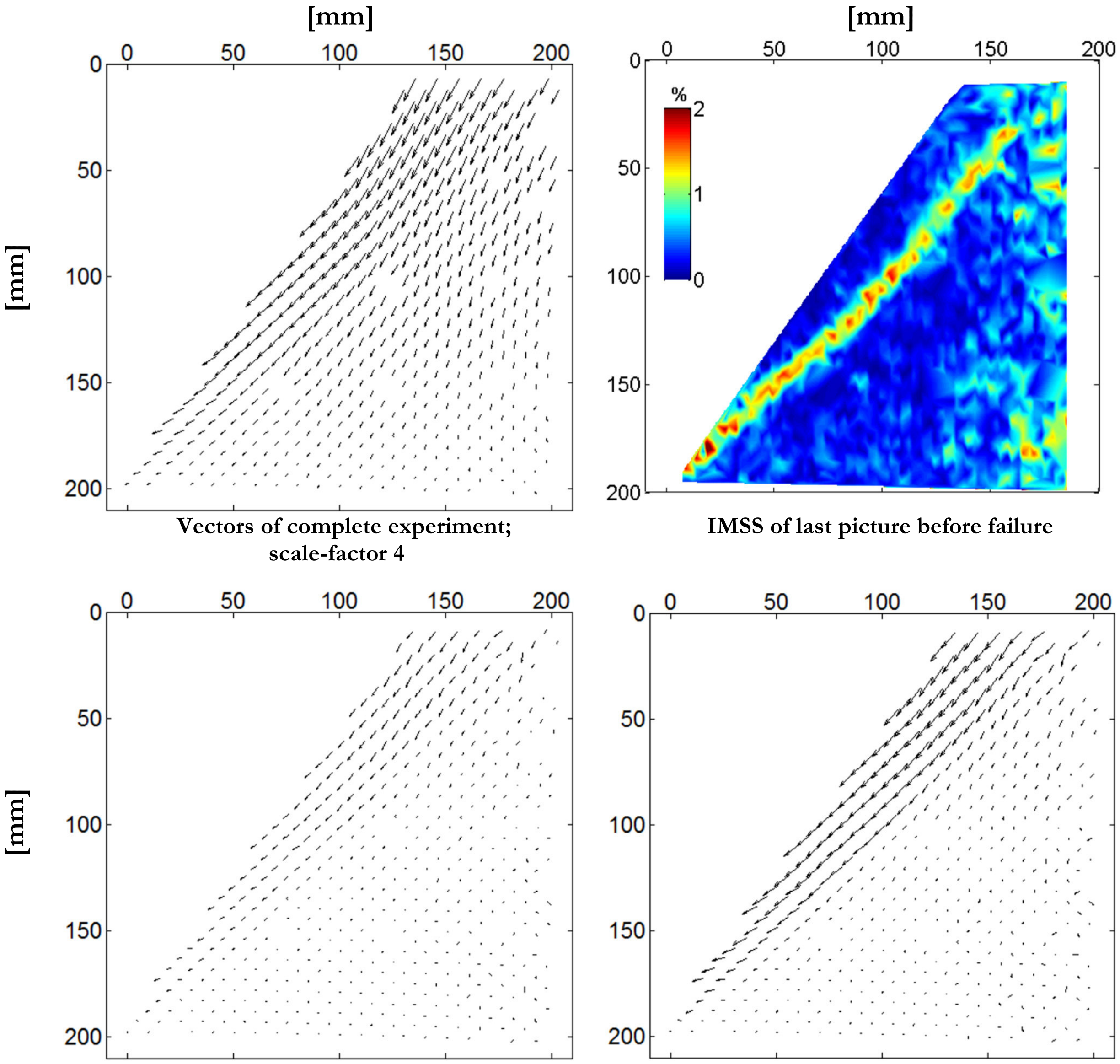


Vectors of complete experiment; scale-factor 4

IMSS of last picture before failure

Vectors between 50 and 20 seconds before failure; scale-factor 20

Vectors between 50 seconds and last picture before failure; scale-factor 20

**Fig. 80: Results of PIV-analysis**

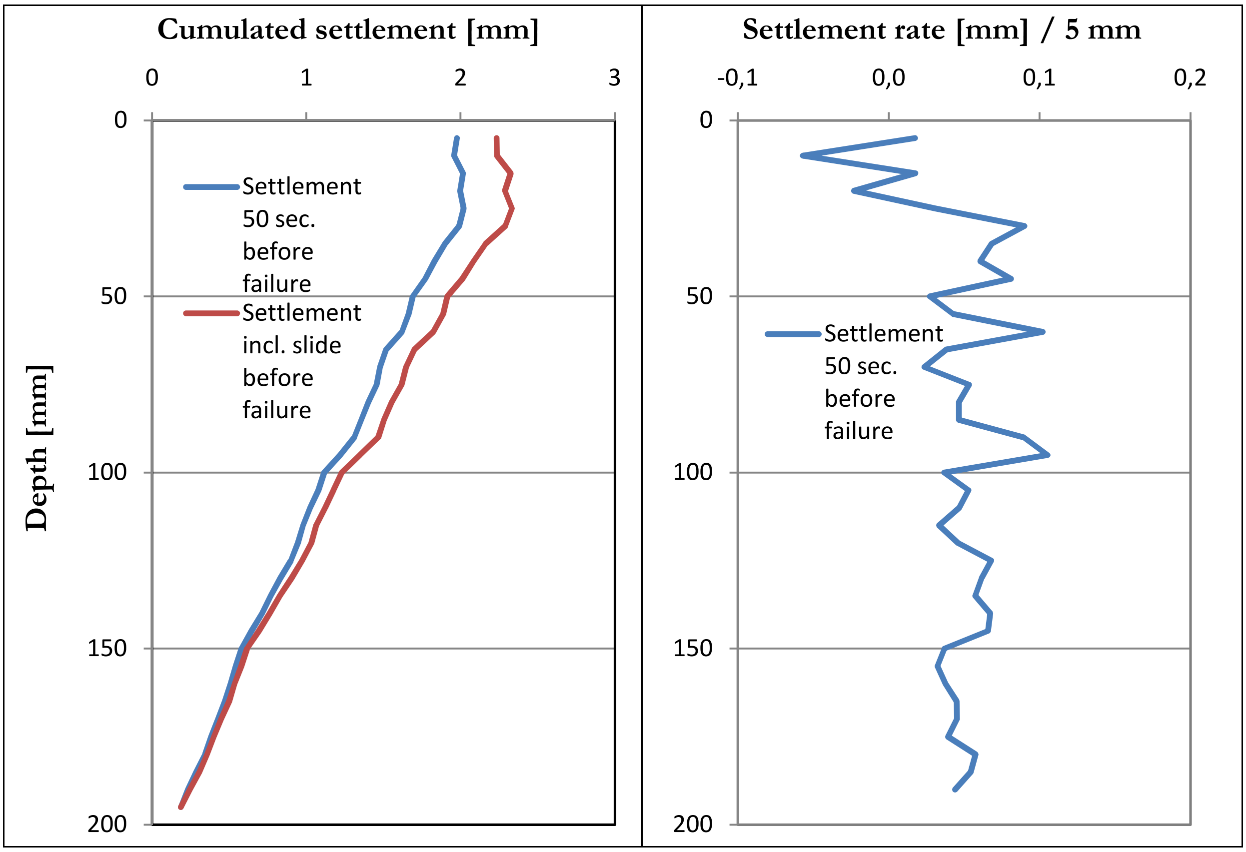


Fig. 81: Settlements of the soil in centrifuge

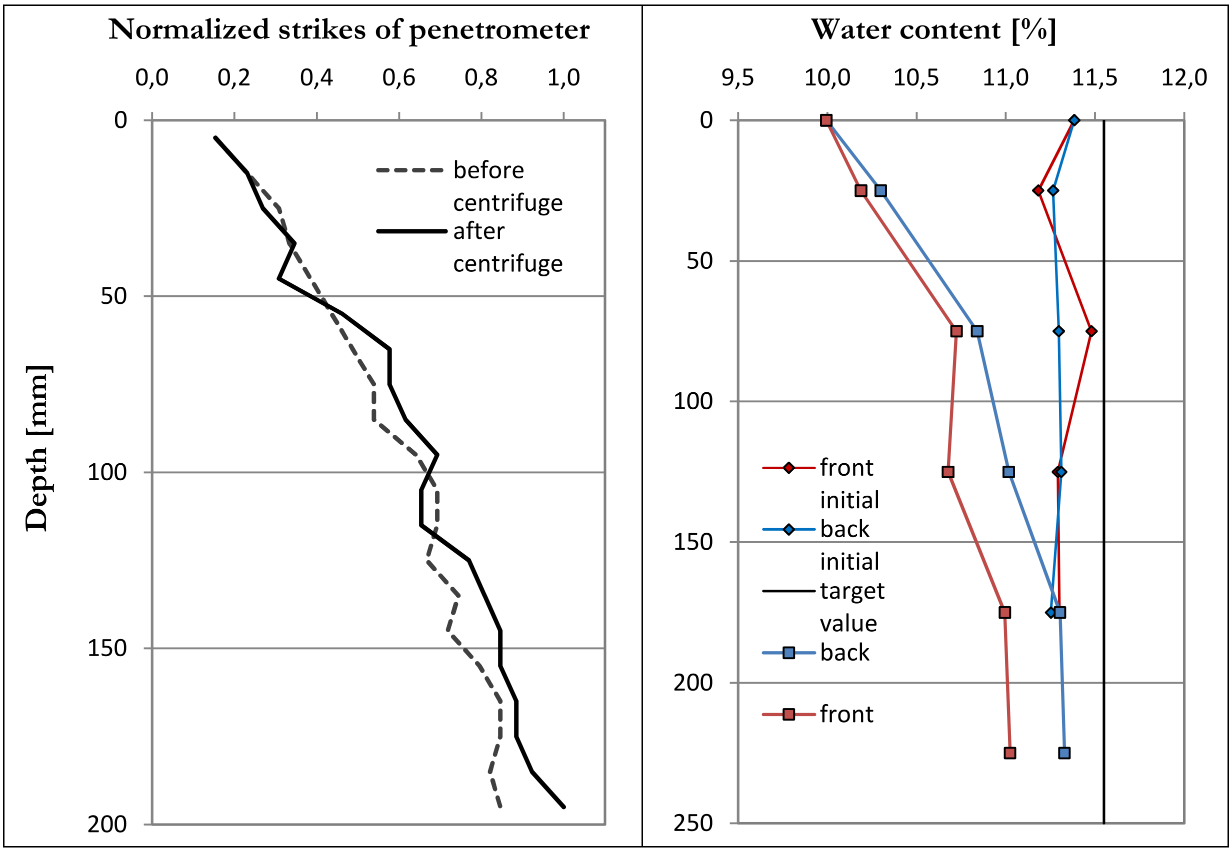


Fig. 82: Results of penetrometer-tests and measurements of water content

# Experiment 8

**Table 16: Characteristics of the experiment**

| | |
|---|---|
| Inclination [deg] | 45 |
| Dry density $\rho_d$ [g/cm³] – before centrifuge | 1.45 |
| Dry density $\rho_d$ [g/cm³] – after centrifuge | 1.51 |
| Water content w [%]<br>- soil preparation<br>- before centrifuge (mean)<br>- after centrifuge (mean)<br>- after centrifuge (layer at toe) | <br>11.63<br>11.10<br>10.47<br>11.01 |
| Max. revolutions per minute [rpm] | 270 |
| Max. g-level [g] | 100.9 |
| Max. height [m] | 20.2 |
| Failure | No |

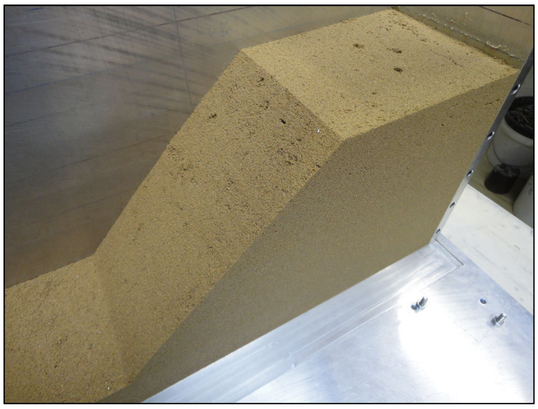

**Fig. 83: Soil after centrifuge**

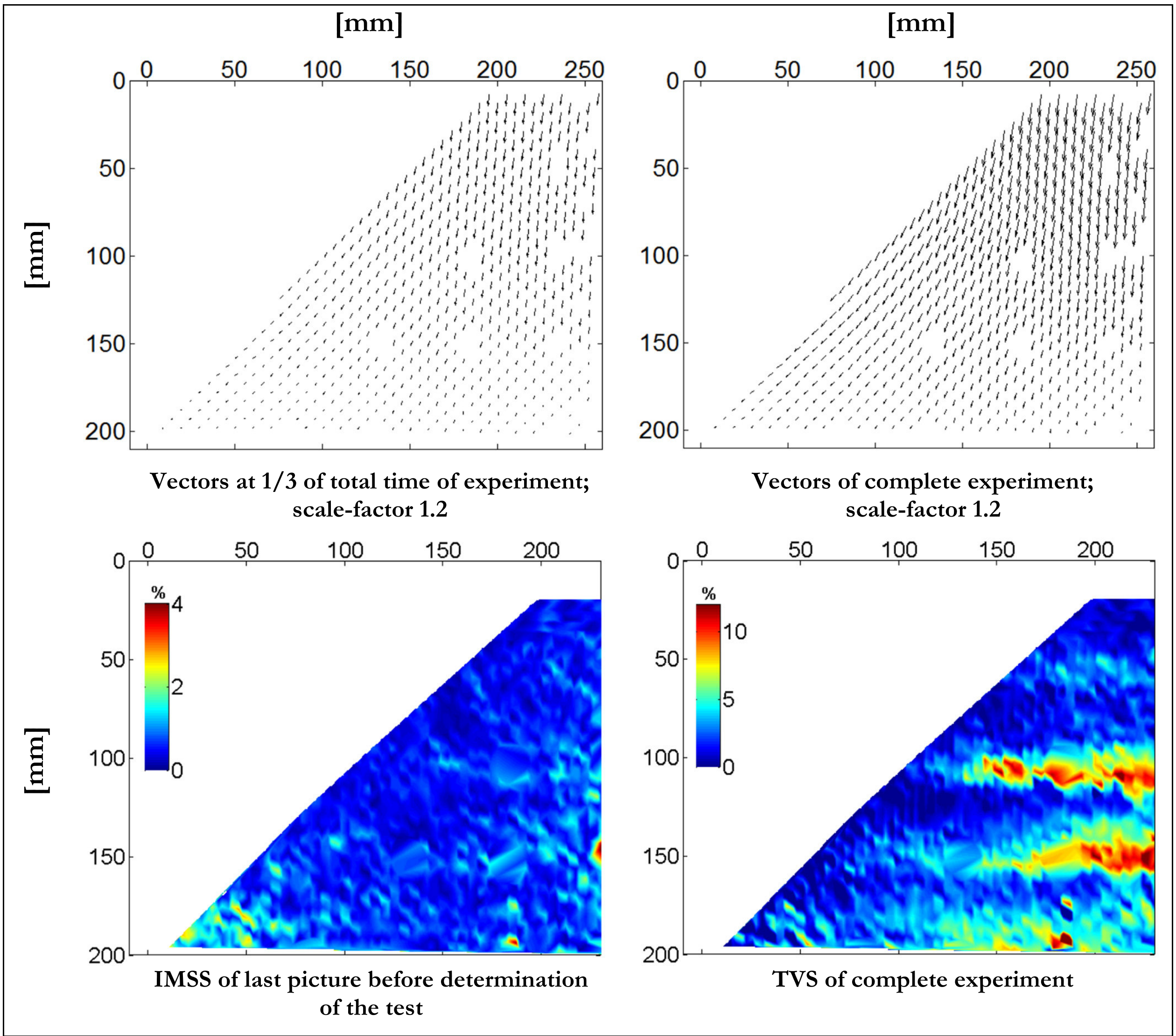


**Fig. 84: Results of PIV-analysis**

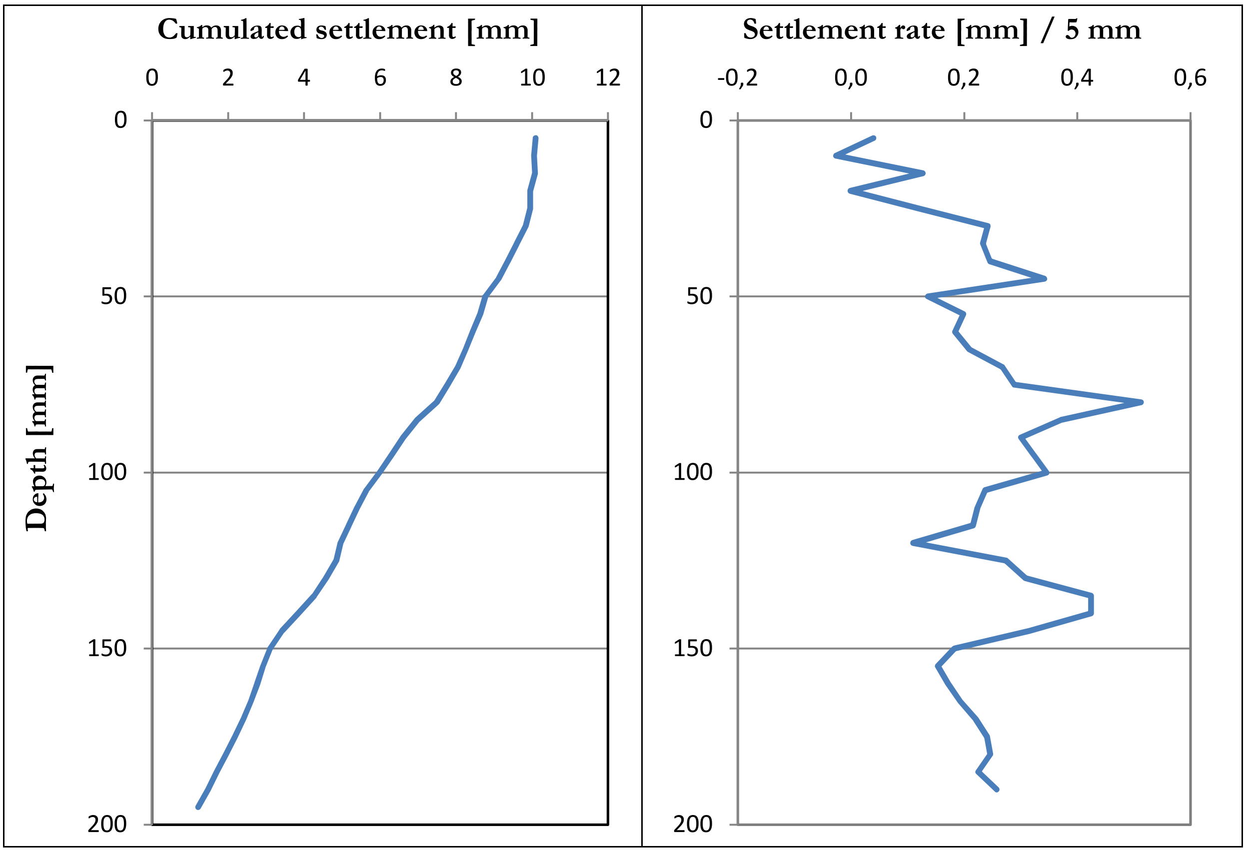


Fig. 85: Settlements of the soil in centrifuge

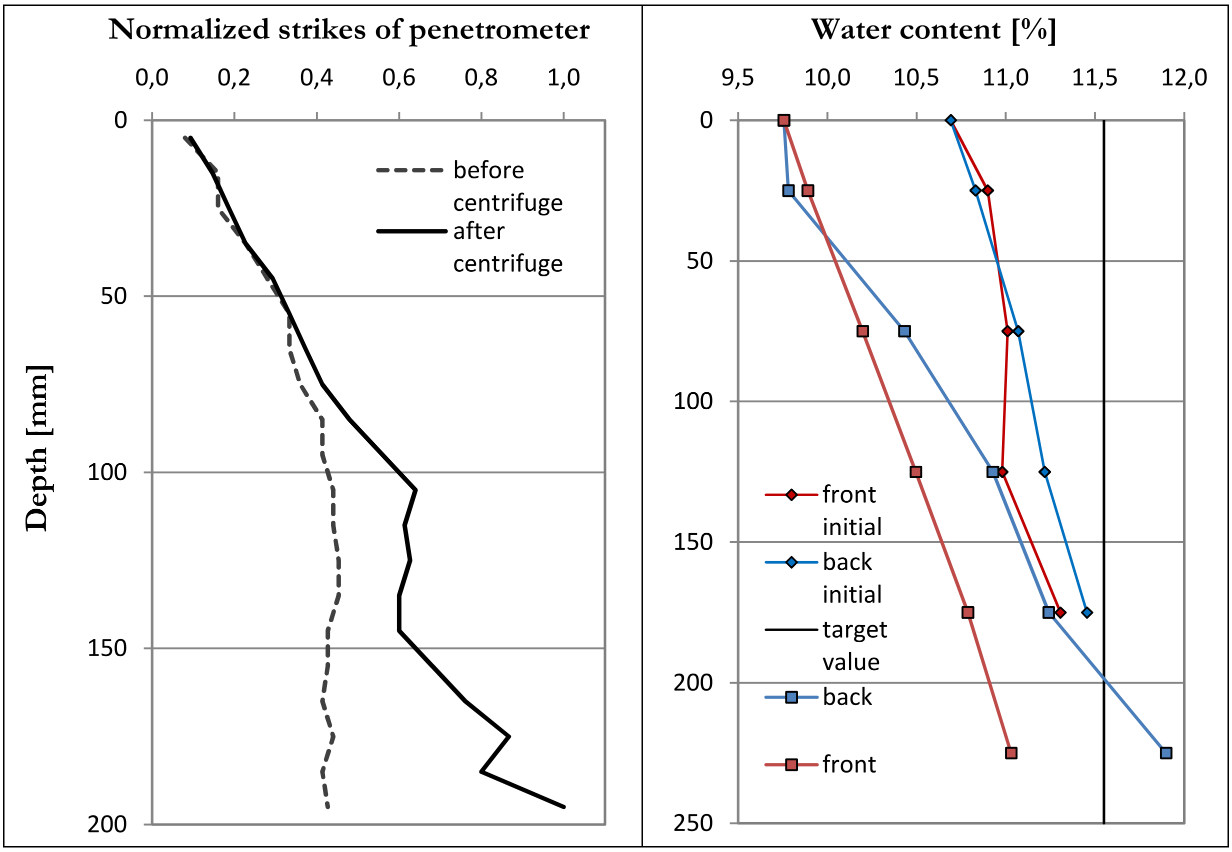


Fig. 86: Results of penetrometer-tests and measurements of water content

# Experiment 9

**Table 17: Characteristics of the experiment**

| | |
|---|---|
| Inclination [deg] | 55 |
| Dry density $\rho_d$ [g/cm³] – before centrifuge | 1.53 |
| Dry density $\rho_d$ [g/cm³] – after centrifuge | 1.58 |
| Water content w [%]<br>- soil preparation<br>- before centrifuge (mean)<br>- after centrifuge (mean)<br>- after centrifuge (layer at toe) | <br>18.12<br>17.36<br>11.90<br>13.00 |
| Max. revolutions per minute [rpm] | 268 |
| Max. g-level [g] | 99.4 |
| Max. height [m] | 19.9 |
| Failure | No |

**Fig. 87: Soil after centrifuge**

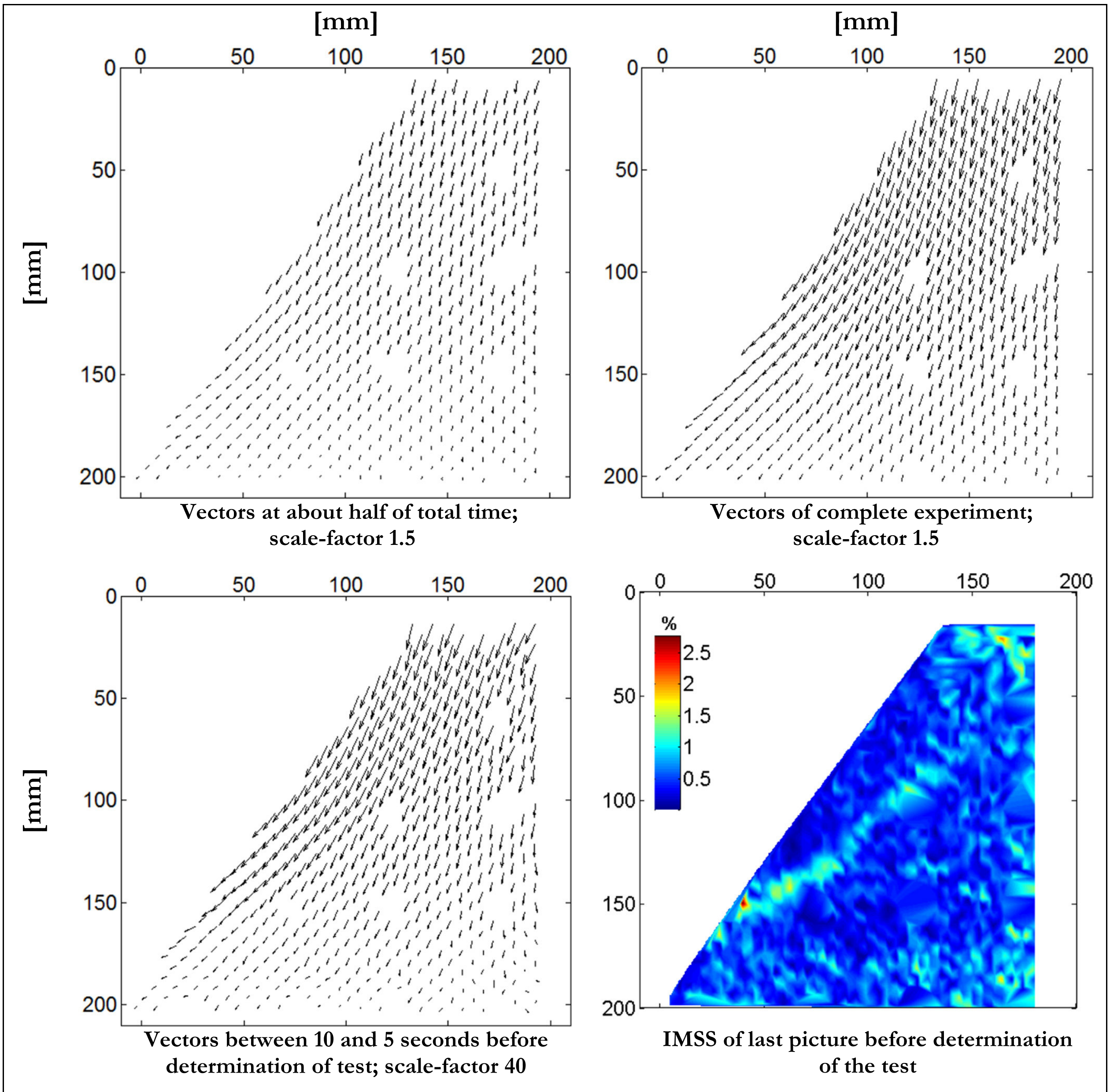


**Fig. 88: Results of PIV-analysis**

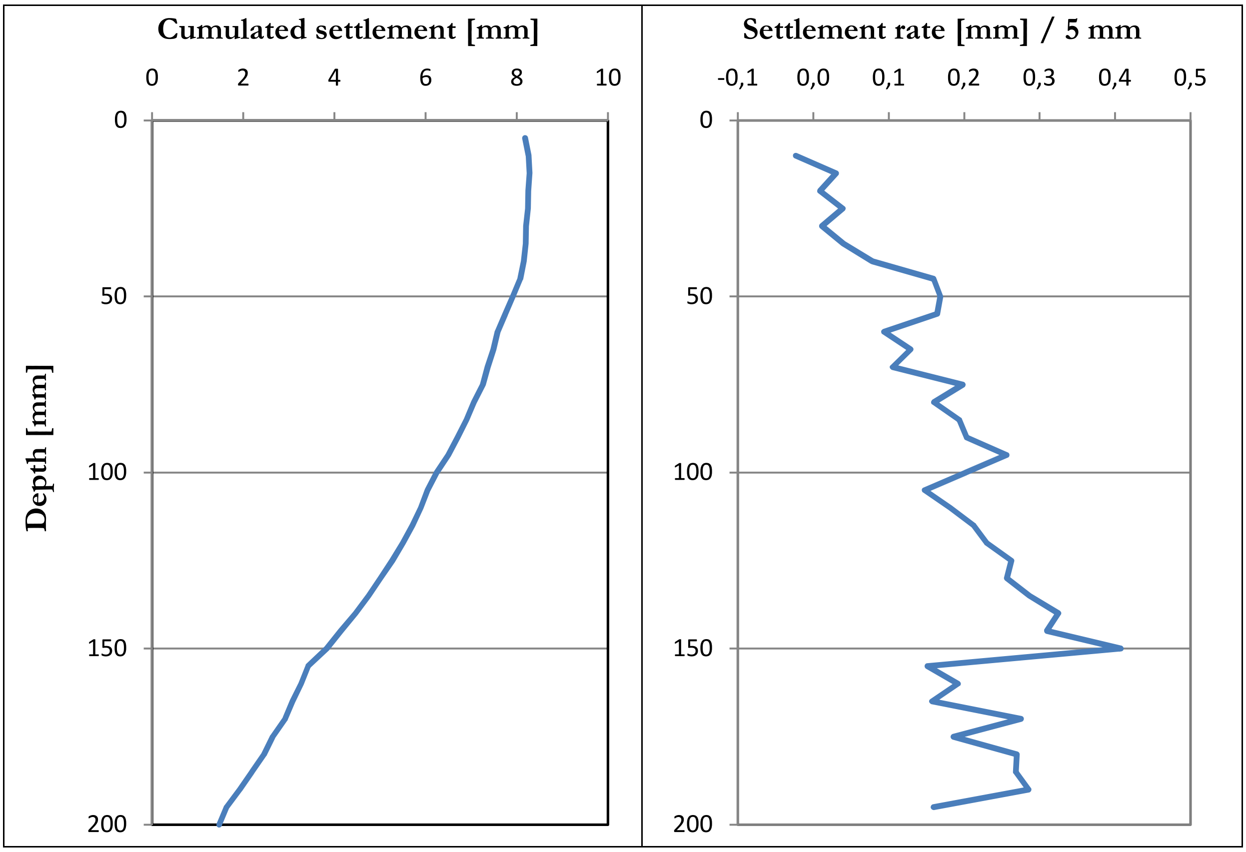


Fig. 89: Settlements of the soil in centrifuge

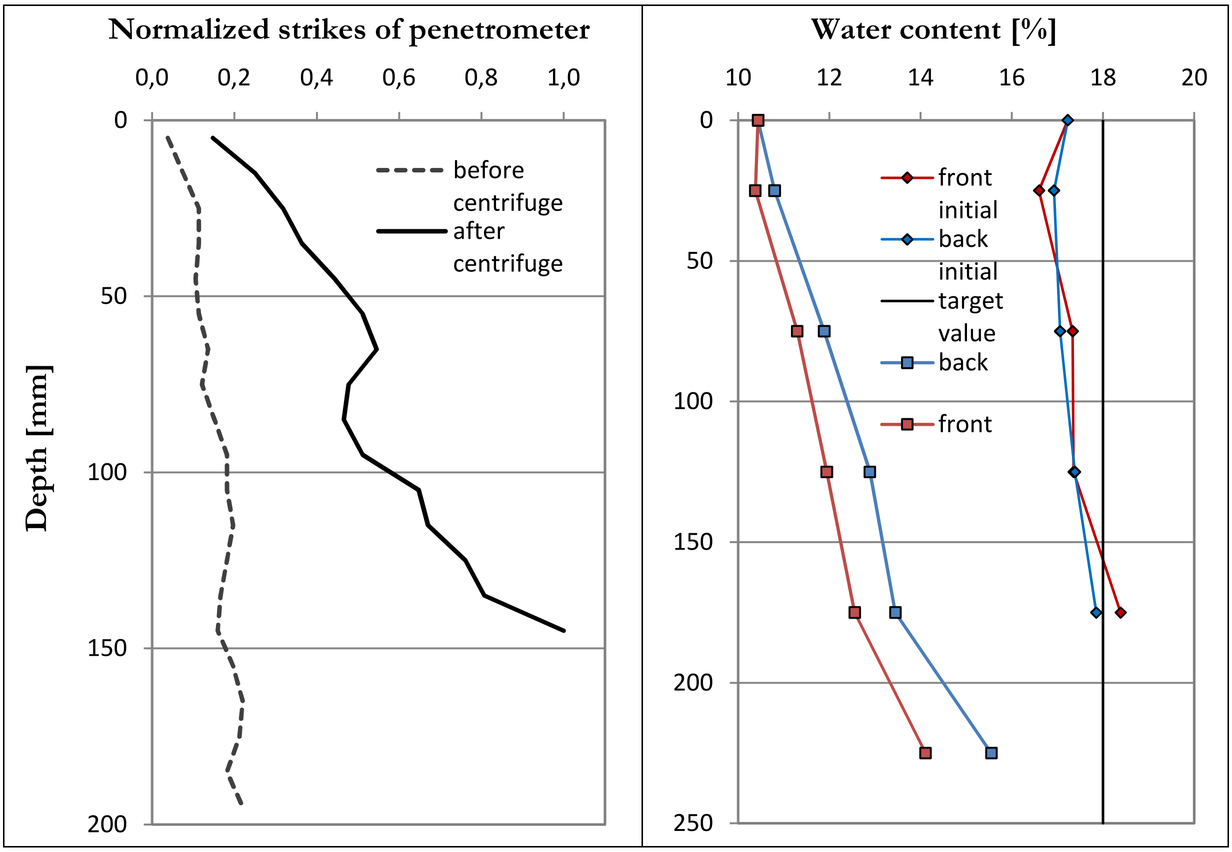


Fig. 90: Results of penetrometer-tests and measurements of water content

## Experiment 10

**Table 18: Characteristics of the experiment**

| | |
|---|---|
| Inclination [deg] | 55 |
| Dry density $\rho_d$ [g/cm³] – before centrifuge | 1.45 |
| Dry density $\rho_d$ [g/cm³] – after centrifuge | 1.53 |
| Water content w [%]<br>- soil preparation<br>- before centrifuge (mean)<br>- after centrifuge (mean)<br>- after centrifuge (layer at toe) | <br>17.86<br>17.05<br>14.15<br>15.63 |
| Max. revolutions per minute [rpm] | 188.6 |
| Max. g-level [g] | 49.2 |
| Max. height [m] | 9.8 |
| Failure | Yes |

**Fig. 91: Soil after centrifuge**

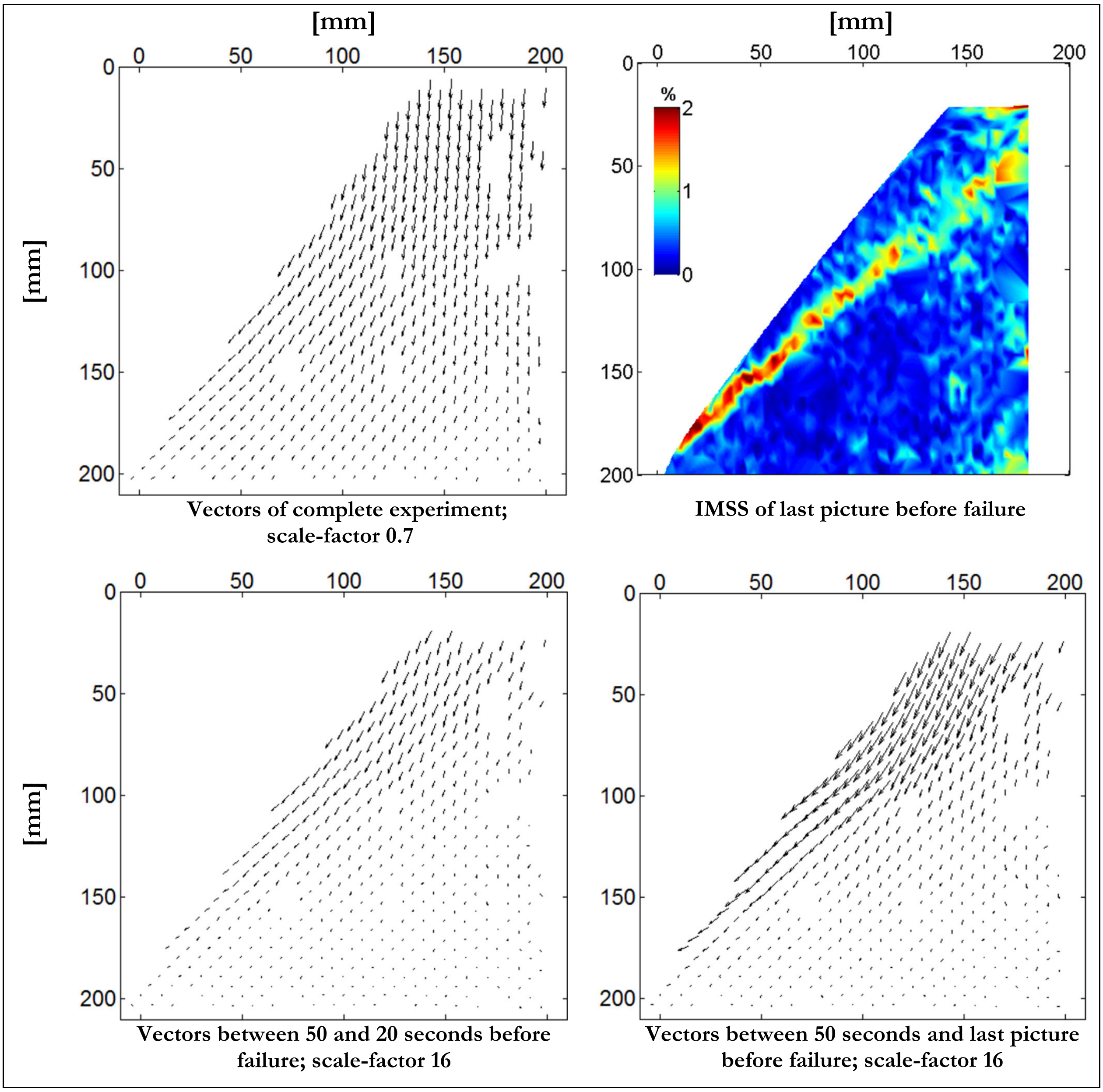


**Fig. 92: Results of PIV-analysis**

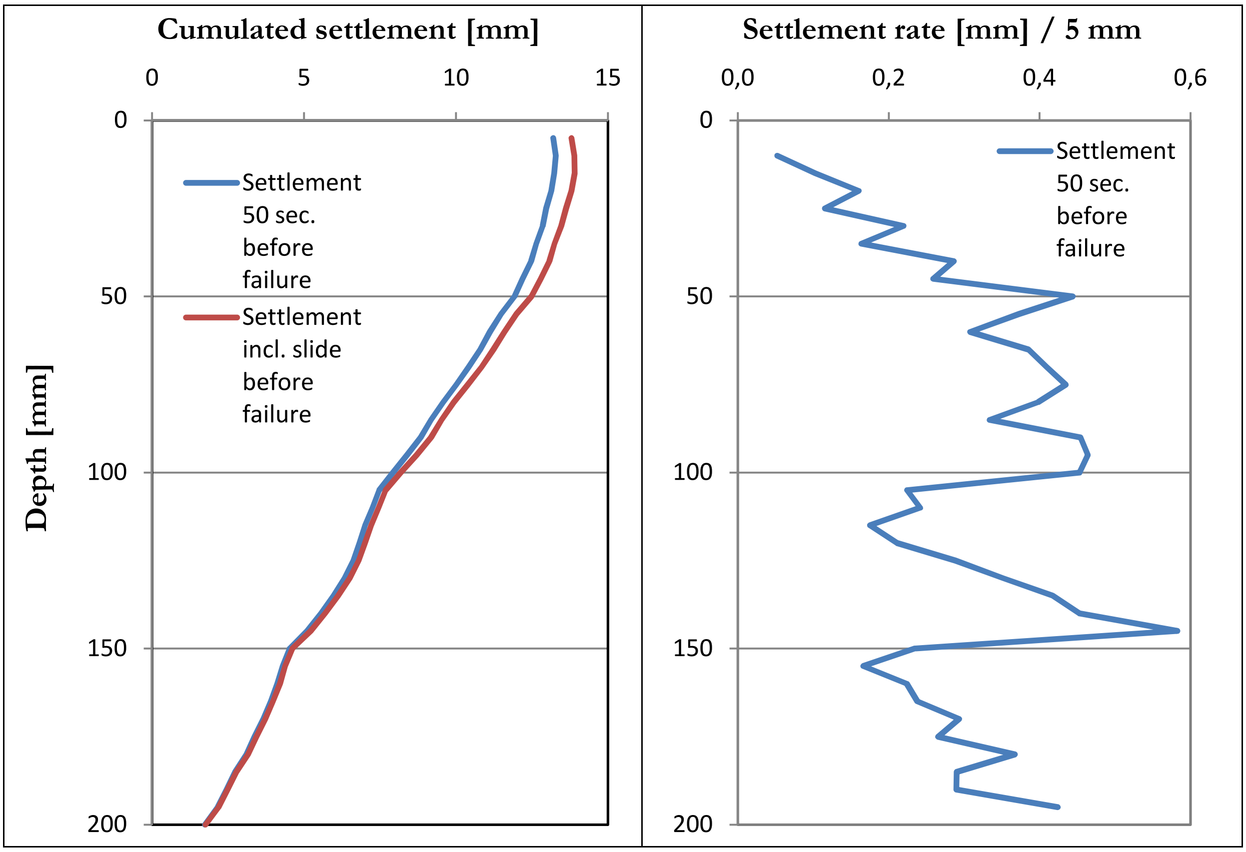


Fig. 93: Settlements of the soil in centrifuge

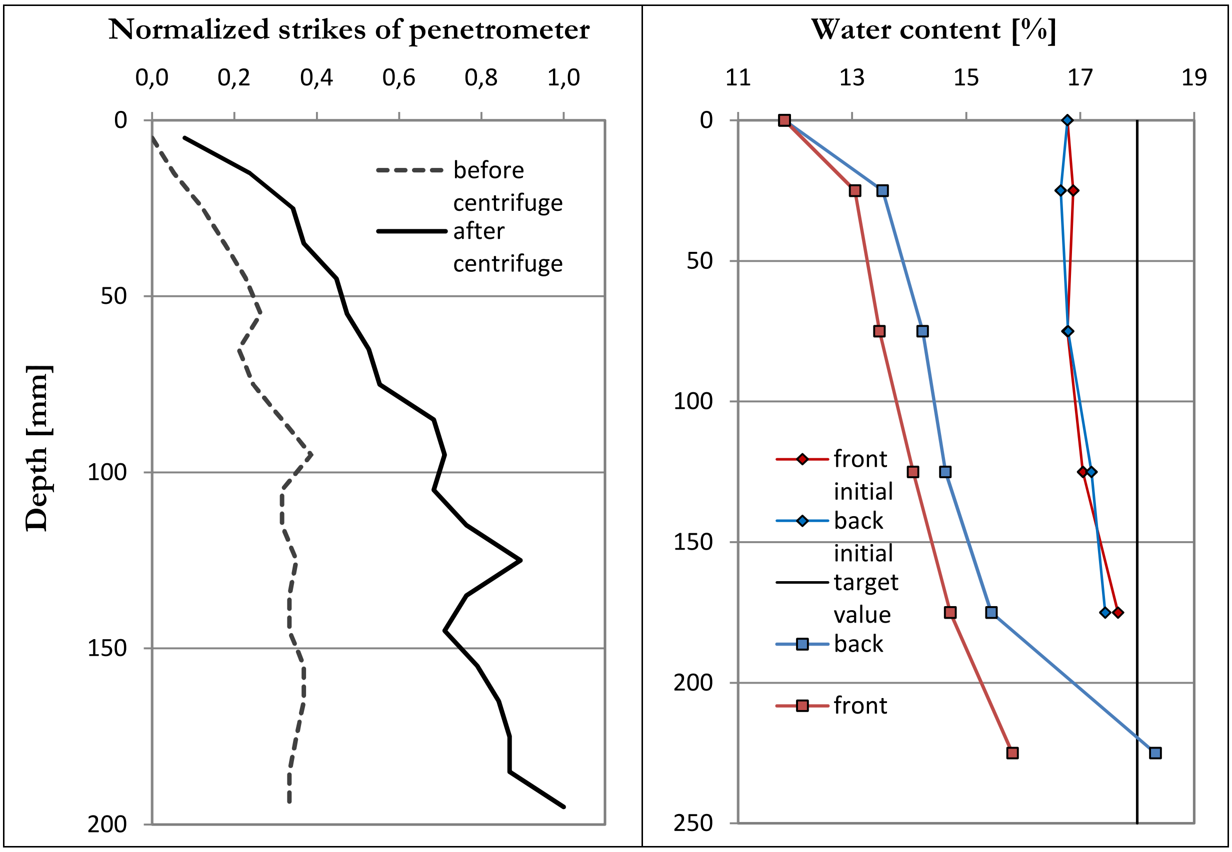


Fig. 94: Results of penetrometer-tests and measurements of water content

## Experiment 11

**Table 19: Characteristics of the experiment**

| | |
|---|---|
| Inclination [deg] | 55 |
| Dry density $\rho_d$ [g/cm³] – before centrifuge | 1.53 |
| Dry density $\rho_d$ [g/cm³] – after centrifuge | 1.59 |
| Water content w [%]<br>- soil preparation<br>- before centrifuge (mean)<br>- after centrifuge (mean)<br>- after centrifuge (layer at toe) | <br>17.96<br>17.34<br>11.82<br>13.28 |
| Max. revolutions per minute [rpm] | 268 |
| Max. g-level [g] | 99.4 |
| Max. height [m] | 19.9 |
| Failure | No |

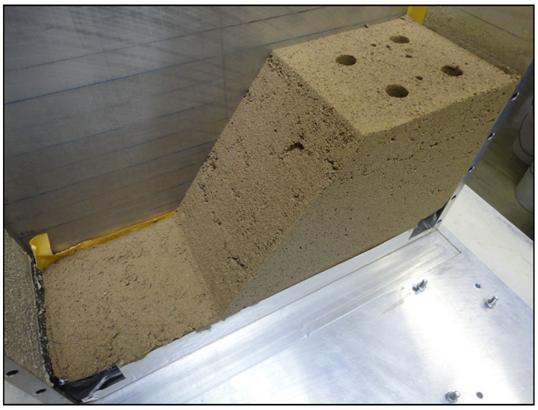

**Fig. 95: Soil after centrifuge**

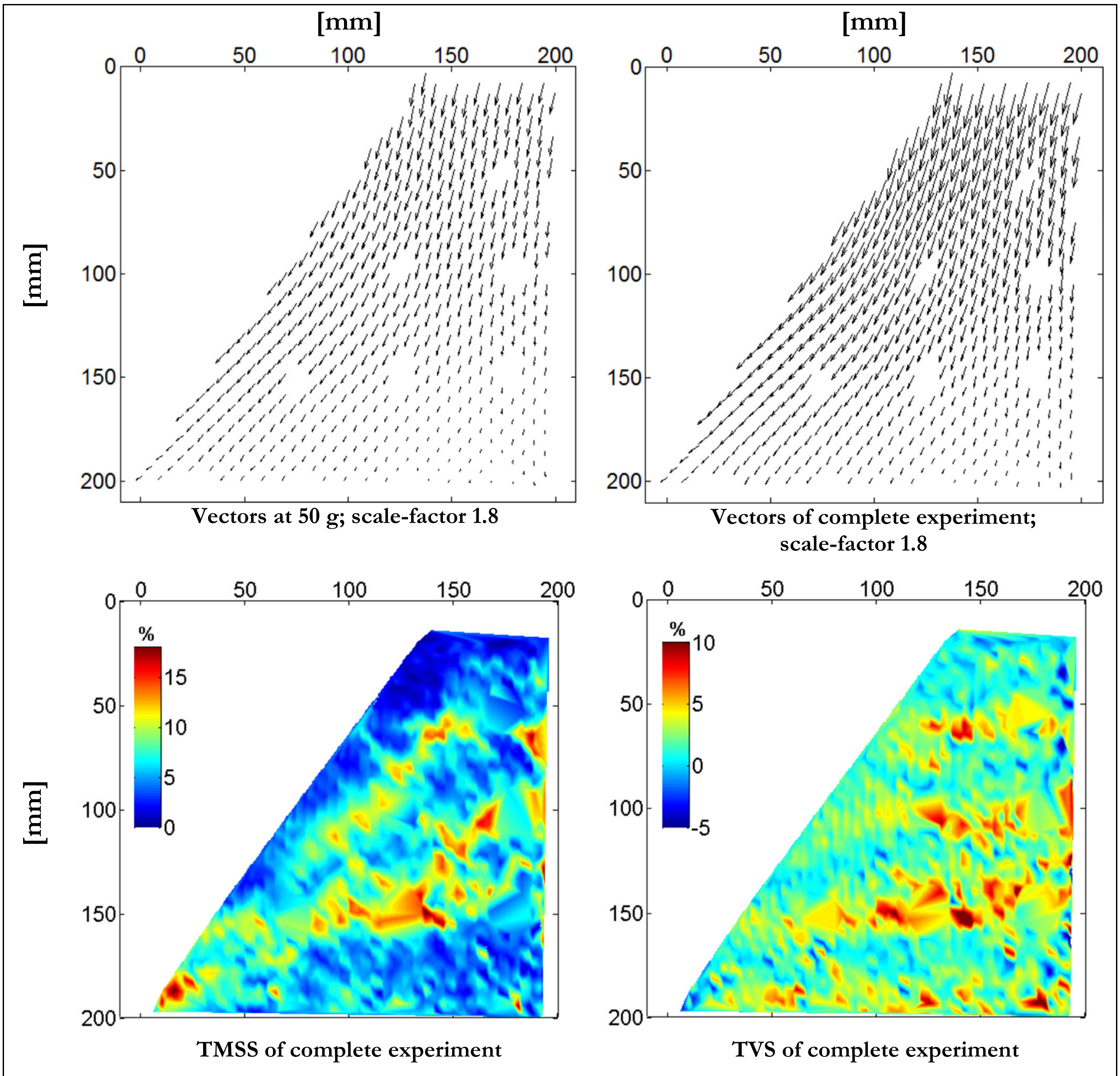


**Fig. 96: Results of PIV-analysis**

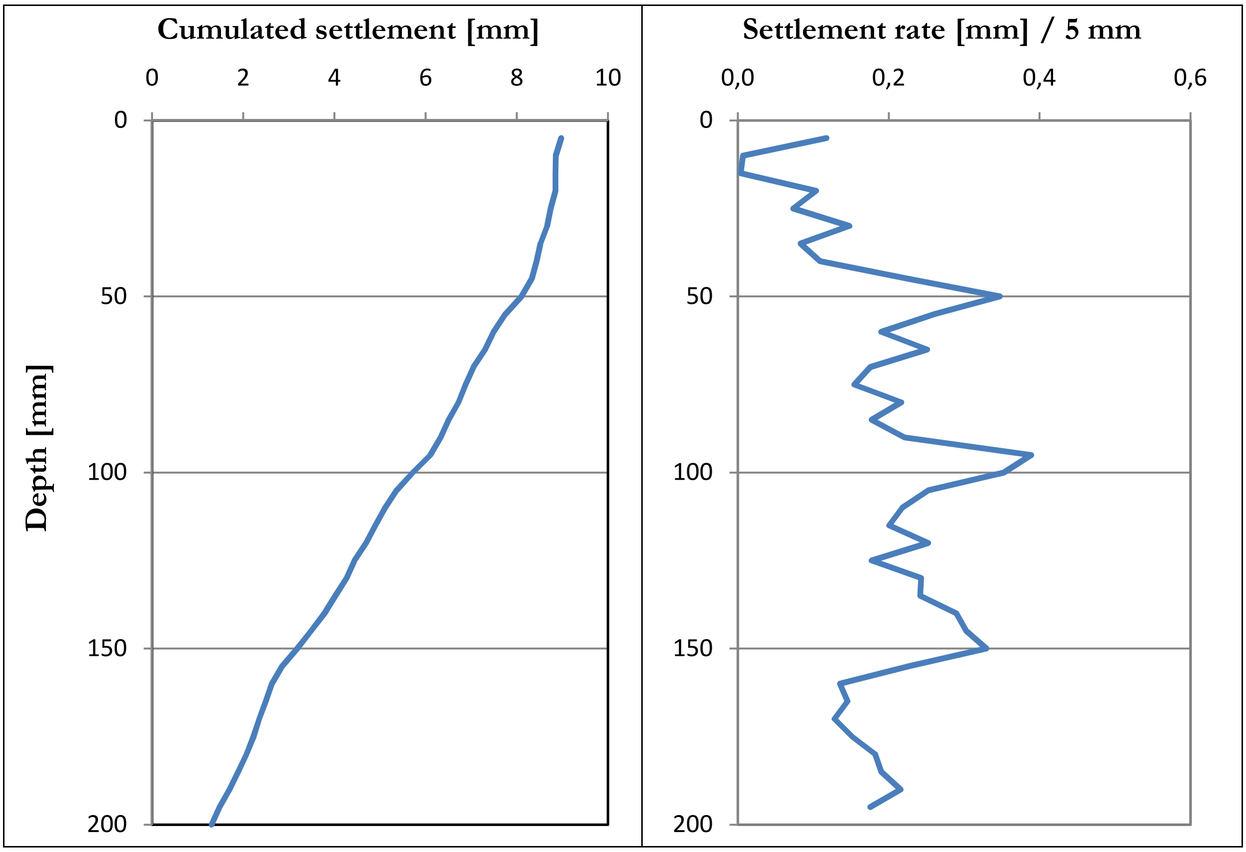


Fig. 97: Settlements of the soil in centrifuge

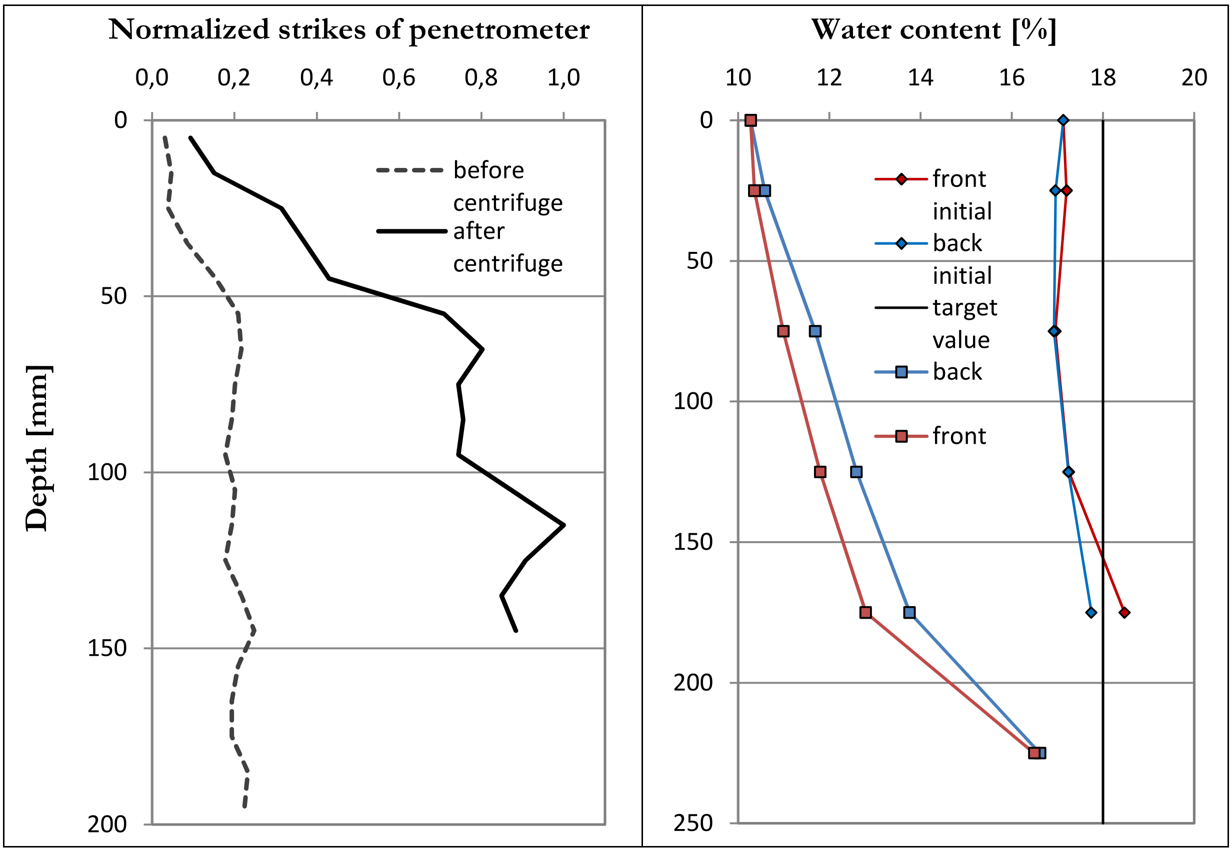


Fig. 98: Results of penetrometer-tests and measurements of water content

# Experiment 12

**Table 20: Characteristics of the experiment**

| | |
|---|---|
| Inclination [deg] | 55 |
| Dry density $\rho_d$ [g/cm³] – before centrifuge | 1.45 |
| Dry density $\rho_d$ [g/cm³] – after centrifuge | 1.56 |
| Water content w [%]<br>- soil preparation<br>- before centrifuge (mean)<br>- after centrifuge (mean)<br>- after centrifuge (layer at toe) | <br>17.98<br>17.43<br>15.14<br>16.53 |
| Max. revolutions per minute [rpm] | 160.7 |
| Max. g-level [g] | 35.7 |
| Max. height [m] | 7.1 |
| Failure | Yes |

**Fig. 99: Soil after centrifuge**

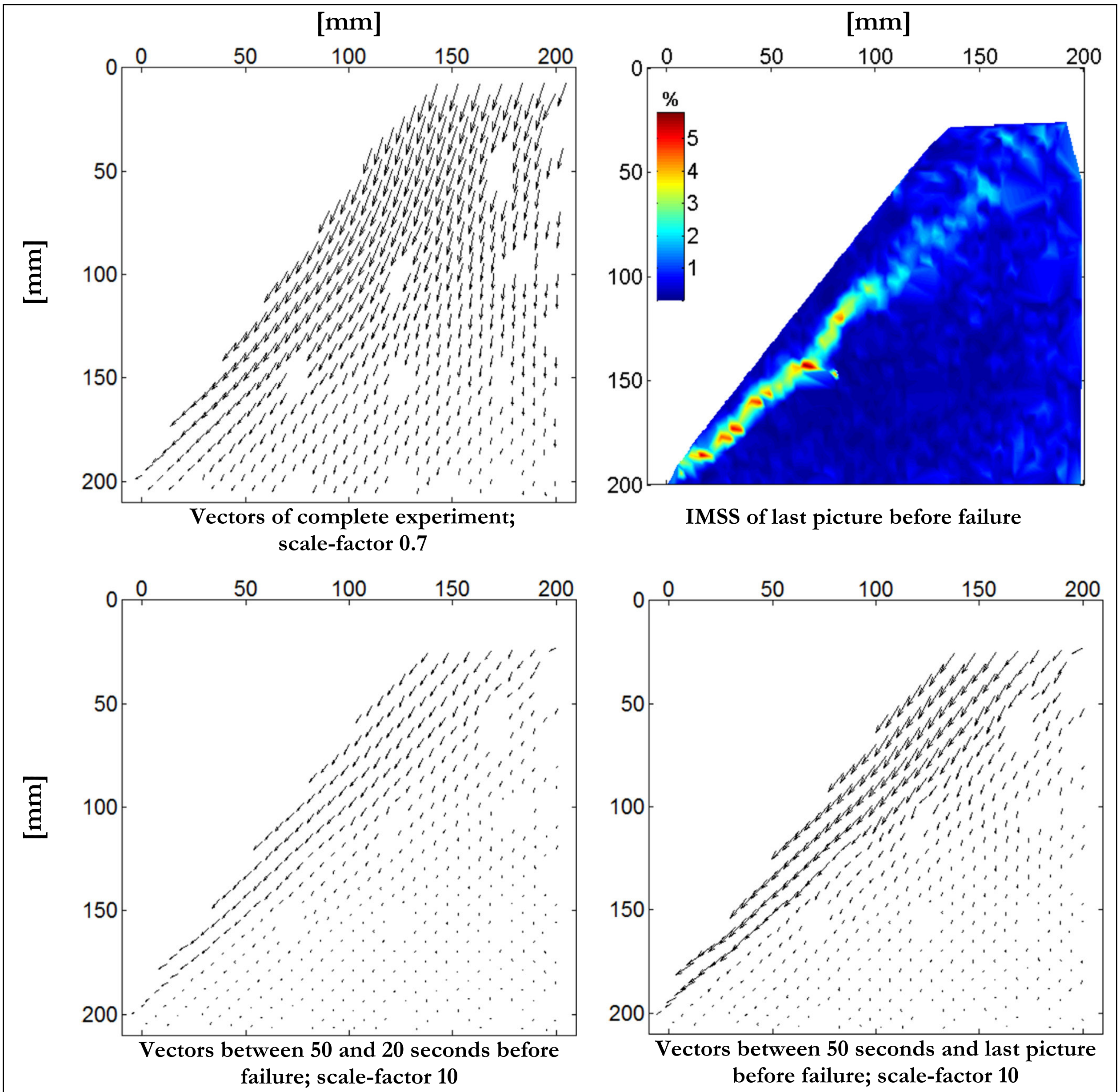


**Fig. 100: Results of PIV-analysis**

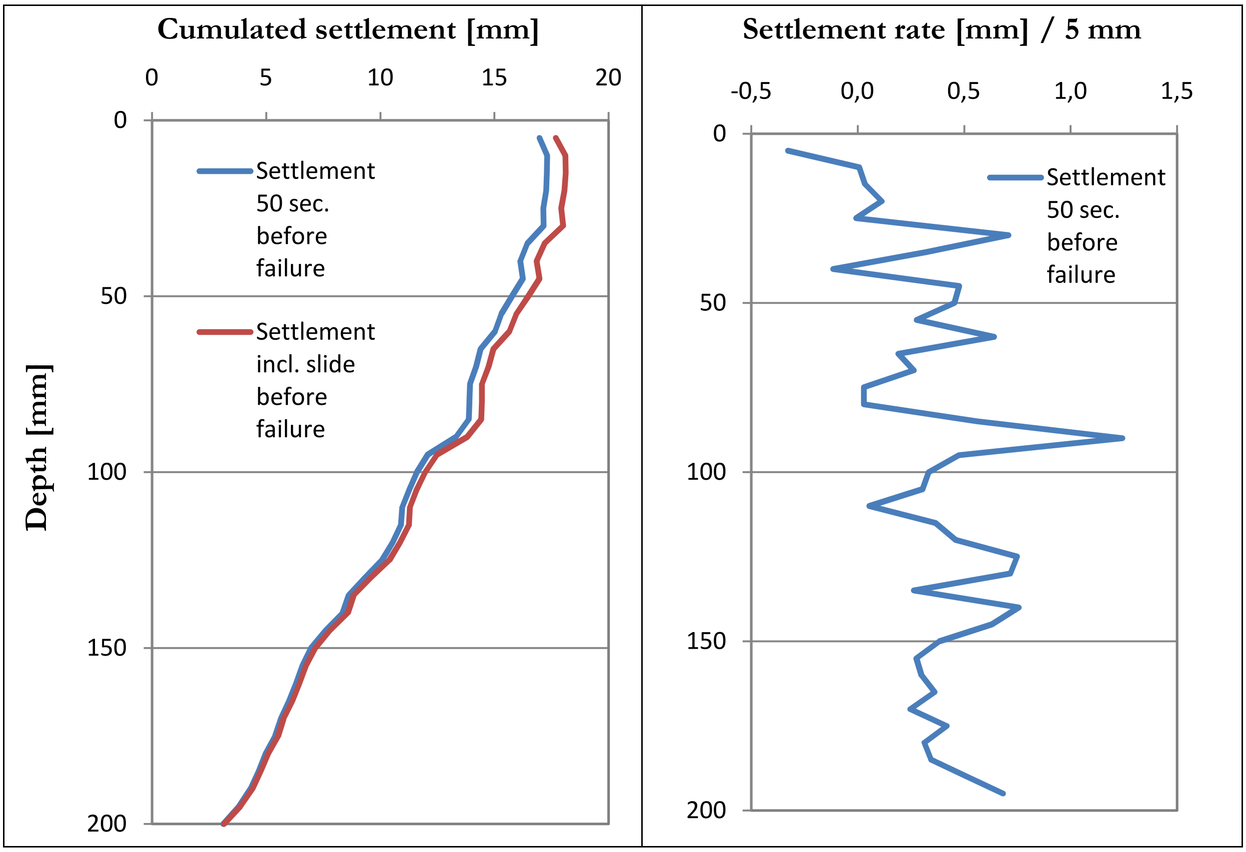

Fig. 101: Settlements of the soil in centrifuge

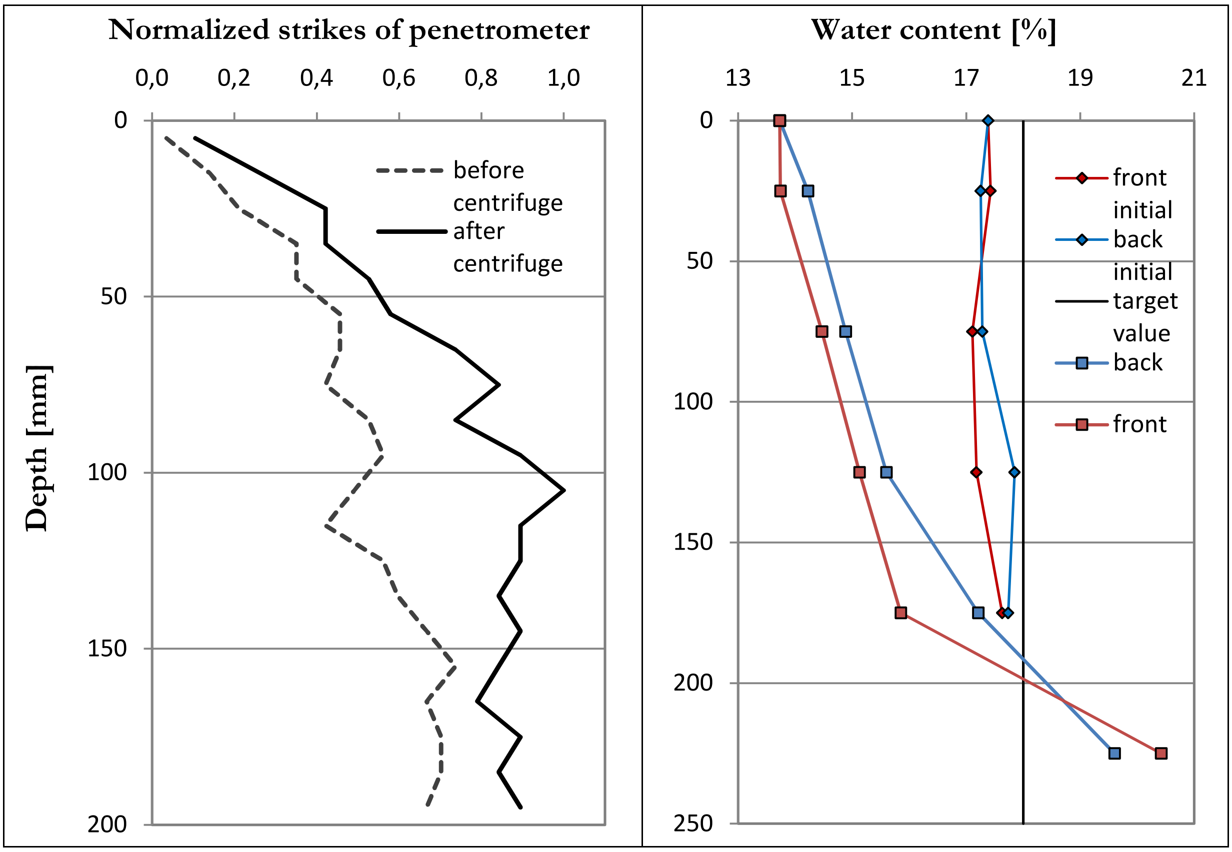

Fig. 102: Results of penetrometer-tests and measurements of water content

# Experiment 14

**Table 21: Characteristics of the experiment**

| | |
|---|---|
| Inclination [deg] | 55 |
| Dry density $\rho_d$ [g/cm³] – before centrifuge | 1.53 |
| Dry density $\rho_d$ [g/cm³] – after centrifuge | 1.61 |
| Water content w [%]<br>- soil preparation<br>- before centrifuge (mean)<br>- after centrifuge (mean)<br>- after centrifuge (layer at toe) | <br>18.19<br>17.99<br>14.62<br>16.35 |
| Max. revolutions per minute [rpm] | 200.2 |
| Max. g-level [g] | 55.5 |
| Max. height [m] | 11.1 |
| Failure | Yes |

**Fig. 103: Soil after centrifuge**

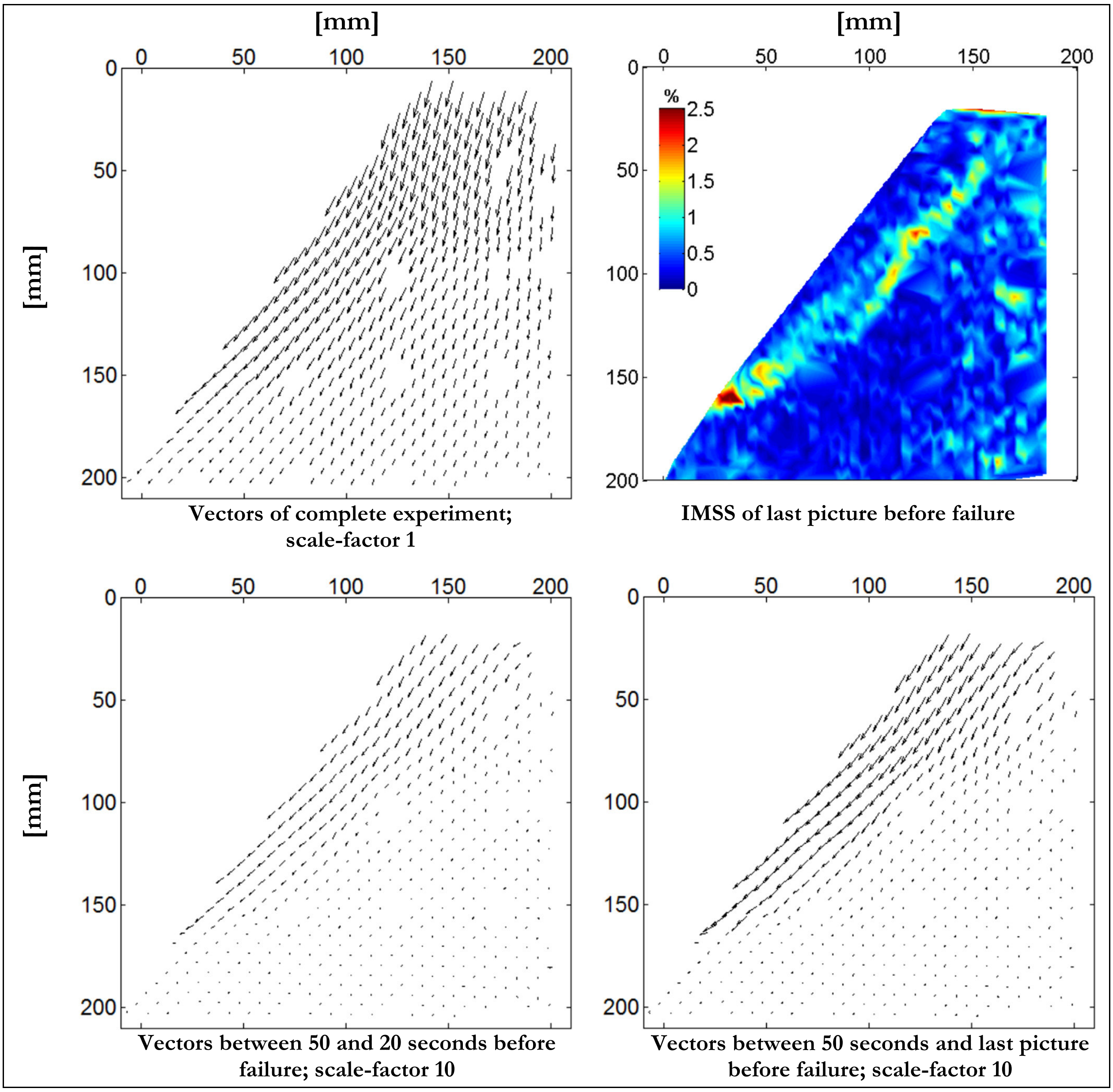


**Fig. 104: Results of PIV-analysis**

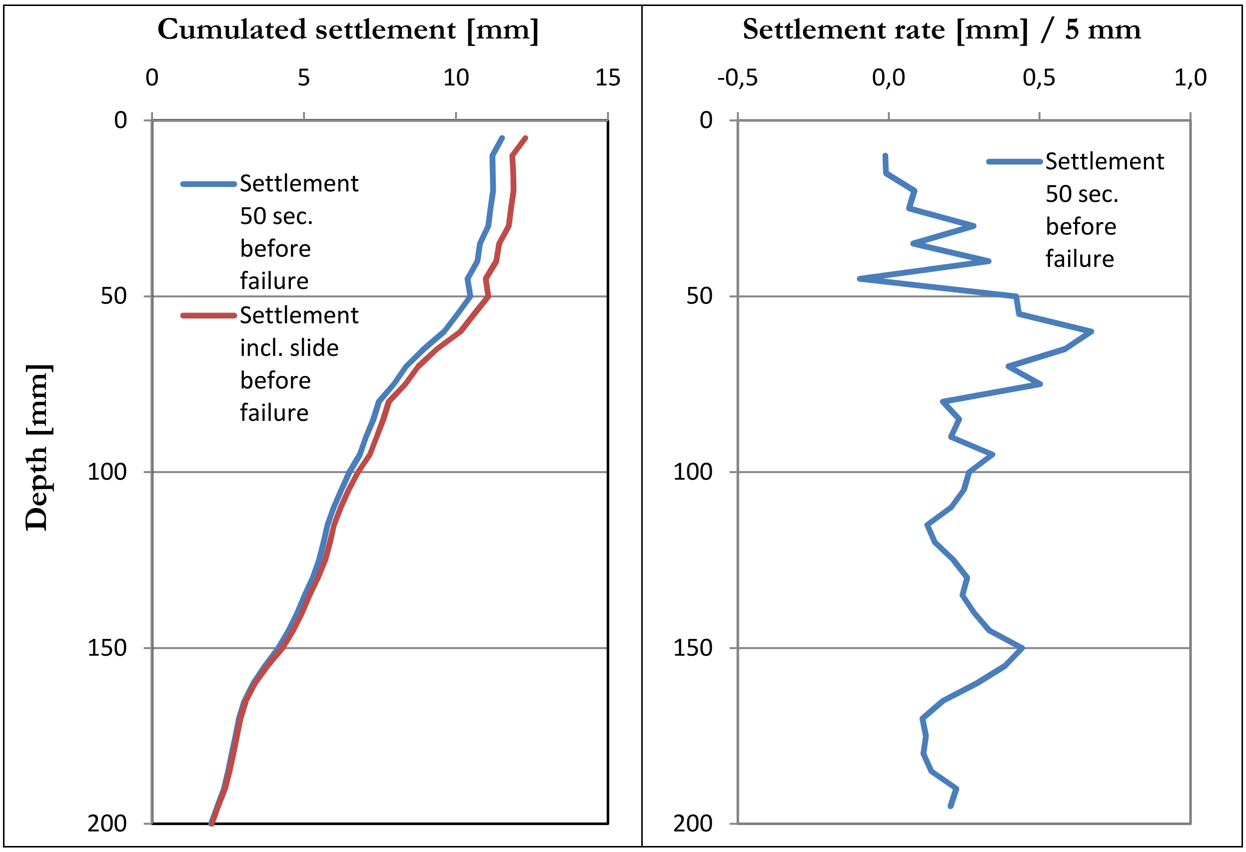


Fig. 105: Settlements of the soil in centrifuge

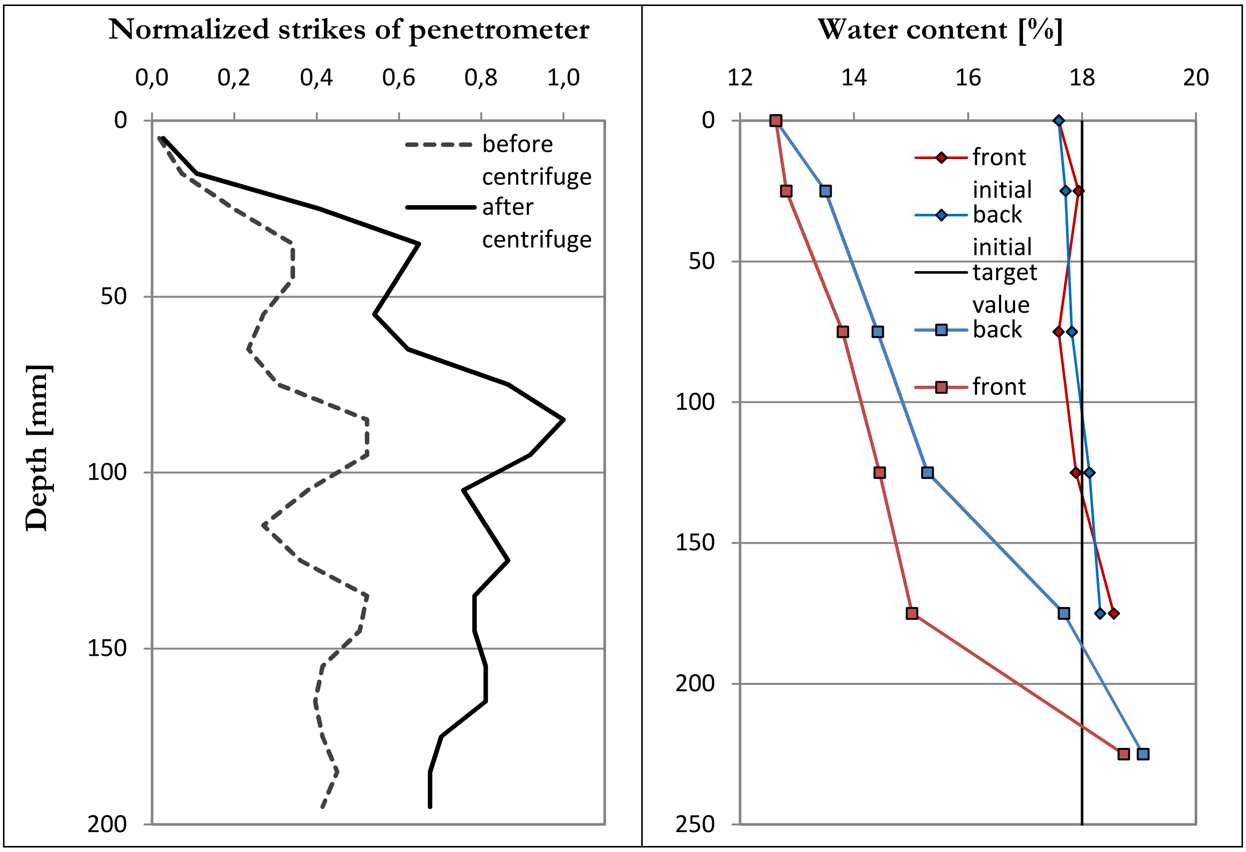


Fig. 106: Results of penetrometer-tests and measurements of water content

# Appendix II

Matlab-scripts which were written for the conducted research are presented in this chapter. The function 'spatial_matrix' arranges the data in a way that vertical settlements, time-series of deformations, etc. can be calculated. The function 'XYdata_half' deletes every second patch to achieve an enhanced visualization of the vector-graphics.

## Function 'spatial_matrix'

```
function [XYmatrix_spatial] =
spatial_matrix(uvdataclean, XYdata, patch_distance)
    %creates a matrix out of the XYdata, where
    %the first two dimensions stand for x- and y-position,
    %the third for the picture-number,
    %and the fourth divides the data in x- and y-coordinates

    Xmin = min(uvdataclean(:,2,1));
    Xmax = max(uvdataclean(:,2,1));
    Ymin = min(uvdataclean(:,2,2));
    Ymax = max(uvdataclean(:,2,2));

    %creating the matrix filled with nan-values and the correct
    %4D-dimensions
    max_X_matrix = ((Xmax - Xmin)/patch_distance) + 1;
    max_Y_matrix = ((Ymax - Ymin)/patch_distance) + 1;
    max_Z_matrix = length(uvdataclean(1,:,1)) - 1;

    XYmatrix_spatial(1:max_X_matrix, 1:max_Y_matrix, 1:max_Z_matrix, 1:2)
      = nan;

    %filling the matrix
    number_of_patches = length(uvdataclean(:,1,1));

    for m = 1:number_of_patches
        x_position = ((uvdataclean(m,2,1) - Xmin) / patch_distance) + 1;
        y_position = ((uvdataclean(m,2,2) - Ymin) / patch_distance) + 1;

        for n = 1:max_Z_matrix
            XYmatrix_spatial(y_position, x_position, n, 1)
              = XYdata(m, n+1, 1);
            XYmatrix_spatial(y_position, x_position, n, 2)
              = XYdata(m, n+1, 2);
        end
    end
end
```

## Function 'XYdata_half'

```
function [XYdata_half] =
thinning_patches(uvdataclean, XYdata, even_number_change)
    %deletes 50% of the patches in order to make an adequate visualization
    %possible

    number_of_patches = length(XYdata);
    delete = 0;
    m = 1;

    %determining the patches of the array which have to be deleted
    for i = 1:number_of_patches

        %at change of line, if even_number_change == 1, switch the variable
        %'delete' in order to generate an offset of the deleted patches
        if i > 1
            if (uvdataclean(i,2,2) ~= uvdataclean((i-1),2,2)) &&
            even_number_change == 1
                if delete == 1
                    delete = 0;
                else
                    delete = 1;
                end
            end
        end

        %saving patch-numbers, which have to be deleted later
        if mod(XYdata(i,1,1), 2) == delete
            delete_array(m) = i;
            m = m + 1;
        end
    end

    %deleting the patches
    XYdata_half = XYdata;
    XYdata_half(delete_array,:,:) = [];
end
```

# References


Aitchison, G. D. (1961): Relationships of moisture and effective stress functions in unsaturated soils. In Proc. Conf. on Pore Pressure and Suction in Soils. Butterworths, London, pp. 47–52.

Aklik, P. (2012): Model tests of geosynthetic reinforced slopes in a geotechnical centrifuge. Dissertation. BOKU, Wien. Institut für Geotechnik.

Aubertin, M.; Mbonimpa, M.; Bussiére, B.; Chapuis, R. P. (2003): A model to predict the water retention curve from basic geotechnical properties. In Canadian Geotechnical Journal 40 (6), pp. 1104–1122.

Bishop, A. W. (1959): The principle of effective stress. In Technisk Ukeblad 106 (39), pp. 859–863.

Bradshaw, A. S.; Baxter, C. D. P. (2007): Sample Preparation of Silts for Liquefaction Testing. In Geotechnical Testing Journal 30 (4).

Bucky, P. B. (1931): The use of models for the study of mining problems. Technical Publication 425, American Institute of Mining and Metallurgical Engineers.

Burdine, N. T. (1953): Relative Permeability Calculations From Pore Size Distribution Data. In Journal of Petroleum Technology 5 (3), pp. 71–78.

Delage, P. (2002): Experimental unsaturated soil mechanics. In J.F.T. Juca, T. M. P. De Campos, F. A. M. Marino (Eds.): Proc. 3rd Int. Conf. on Unsaturated Soils, UNSAT'2002. Recife, Brazil: Balkema (3), pp. 973–996.

Della, N.; Arab, A.; Belkhatir, M. (2011): Influence of specimen-reconstituting method on the undrained response of loose granular soil under static loading. In Acta Mechanica Sinica 27 (5), pp. 796–802.

Diwald, A. (2011): Untersuchung der Scherfestigkeit eines Modellbodens mittels Triaxialversuch. Masterarbeit. BOKU, Wien. Institut für Geotechnik.

Fredlund, D. G.; Morgenstern, N. R.; Widger, R. A. (1978): The shear strength of unsaturated soils. In Canadian Geotechnical Journal 15 (3), pp. 313–321.

Fredlund, D. G.; Rahardjo, H. (1993): Soil mechanics for unsaturated soils. New York: John Wiley & Sons Inc.

Fredlund, D. G.; Xing, A. (1994): Equations for the soil-water characteristic curve. In Canadian Geotechnical Journal 31 (3), pp. 521–532.

Garnier, J.; Gaudin, C.; Springman, S. M.; Culligan, P. J.; Goodings, D.; König, D. et al. (2007): Catalogue of scaling laws and similitude questions in centrifuge modelling. In International Journal of Physical Modelling in Geotechnics 7 (3), pp. 1–23.

Government Information Centre Hong Kong. Available online at http://www.info.gov.hk/gia/general/201402/20/P201402200347_photo_1065556.htm, checked on 16/10/2014.

Hungr, O.; Evans, S. G.; Bovis, M. J.; Hutchinson, J. N. (2001): A Review of the Classification of Landslides of the Flow Type. In Environmental & Engineering Geoscience 7 (3), pp. 221–238.

Idinger, G. (2010): Centrifuge model tests and numerical analysis on the face stability of shallow tunnels in dry sand. Masterarbeit. BOKU, Wien. Institut für Geotechnik.

Idinger, G. (2015): Experimental study on failure initiation in partially saturated slopes (working title - dissertation in process). BOKU, Wien. Institut für Geotechnik.

Khalili, N.; Khabbaz, M. H. (1998): A unique relationship for x for the determination of the shear strength of unsaturated soils. In Géotechnique 48 (5), pp. 681–687.

Konkol, J. (2014): Derivation of the scaling laws used in geotechnical centrifuge modelling-application of dimensional analysis and Buckingham Π theorem. In Technical Sciences 17 (1), pp. 31–44.

Ladd, R. S. (1978): Preparing Test Specimens Using Undercompaction. In Geotechnical Testing Journal 1 (1), pp. 16–23.

Ling, H. I.; Wu, M. H.; Leshchinsky, D.; Leshchinsky, B. (2009): Centrifuge Modeling of Slope Instability. In Journal of Geotechnical and Geoenvironmental Engineering 135 (6), pp. 758–767.

Mathews, J. (2013): Investigation of granular flow using silo centrifuge models. Dissertation. BOKU, Wien. Institut für Geotechnik.

Mualem, Y. (1976): A new model for predicting the hydraulic conductivity of unsaturated porous media. In Water Resources Research 12 (3), pp. 513–522.

Muir Wood, D. (2004): Geotechnical Modelling. London, New York: Spon Press. pp. 271, 272, 277, 278 f.

Mulilis, J. P.; Arulanandan, K.; Mitchell, J. K.; Chan, C. K.; Seed, H. B. (1977): Effects of Sample Preparation on Sand Liquefaction. In Journal of the Geotechnical Engineering Division 103 (2), pp. 91–108.

Ng, C. W. W.; Menzies, B. (2007): Advanced Unsaturated Soil Mechanics and Engineering. London, New York: Taylor & Francis. pp. 140, 142, 308

Nottingham Centre for Geomechanics / UK (2014): Scanning Electron Microscope (SEM) - photos of soil, 2014.

Nuth, M.; Laloui, L. (2008): Effective stress concept in unsaturated soils: Clarification and validation of a unified framework. In International Journal for Numerical and Analytical Methods in Geomechanics 32 (7), pp. 771–801.

Pham, H. Q.; Fredlund, D. G.; Barbour, S. L. (2003): A practical hysteresis model for the soil-water characteristic curve for soils with negligible volume change. In Géotechnique 53 (2), pp. 293–298.

Pietruszczak, S.; Haghighat, E. (2013): Assessment of slope stability in cohesive soils due to a rainfall. In International Journal for Numerical and Analytical Methods in Geomechanics 37 (18), pp. 3278–3292.

Pregl, O. (1999): Handbuch der Geotechnik. Auszug für die Lehrveranstaltung Erd- und Grundbau I.

Rahardjo, H.; Leong, E.C.; Rezaur, R. B. (2002): Studies of rainfall-induced slope failures. In P. P. Rahardjo (Ed.): Slope 2002. Proceedings of the National Seminar. Bandung, Indonesia, 27.04.2002, pp. 15–29.

Schöfer, D. (2012): Untersuchung der Scherparameter eines Feinmittelsandes im gesättigten und teilgesättigten Zustand. Masterarbeit. BOKU, Wien. Institut für Geotechnik.

Schofield, A. N. (1980): Cambridge Geotechnical Centrifuge Operations. In Géotechnique 30 (3), pp. 227–268.

Schrefler, B. A. (1984): The finite element method in soil consolidation (with applications to surface subsidence). Ph.D. Thesis. University College of Swansea.

Staubmann, R. (2008): Zentrifugenmodellversuche an Krainerwänden. Masterarbeit. BOKU, Wien. Institut für Geotechnik.

Take, W. A.; Bolton, M. D.; Wong, P. C. P.; Yeung, F. J. (2004): Evaluation of landslide triggering mechanisms in model fill slopes. In Landslides 1 (3), pp. 173–184.

Tamate, S.; Suemasa, N.; Katada, T. (2012): Simulation of precipitation on centrifuge models of slopes. In International Journal of Physical Modelling in Geotechnics 12 (3), pp. 89–101.

Terzaghi, K. (1936): The shearing resistance of saturated soils and the angle between the planes of shear. In International Conference on Soil Mechanics and Foundation Engineering (Cambridge, MA), pp. 54–56.

The MathWorks, Inc: Matlab.

Tourenfahrer. Available online at http://www.tourenfahrer.de/motorrad-reisen/motorrad-reise-news/felssturz-auf-felbertauernstrasse/, checked on 16/10/2014.

Van Genuchten, M. T. (1980): A Closed-form Equation for Predicting the Hydraulic Conductivity of Unsaturated Soils. In Soil Science Society of Ameria Journal 44 (5), pp. 892–898.

Vanapalli, S. K.; Fredlund, D. G.; Pufahl, D. E.; Clifton, A. W. (1996): Model for the prediction of shear strength with respect to soil suction. In Canadian Geotechnical Journal 33 (3), pp. 379–392.

Wang, G.; Sassa, K. (2003): Pore-pressure generation and movement of rainfall-induced landslides: effects of grain size and fine-particle content. In Engineering Geology 69 (1-2), pp. 109–125.

White, D. J.; Take, W. A. (2002): GeoPIV: Particle Image Velocimetry (PIV) software for use in geotechnical testing. In Cambridge University Engineering Department, Technical Report.

Wisner, B.; Blaikie, P.; Cannon, T.; Davis, I. (Eds.) (2004): At Risk. Natural hazards, people's vulnerability and disasters. 2nd ed.: Routledge.

# Declaration in lieu of oath

**by**

## Grims Michael

This is to confirm my master thesis was independently composed/authored by myself, using solely the referred sources and support.
I additionally assert that this thesis has not been part of another examination process.

Vienna, __________________________ __________________________